Interface analysis of nanoscale thin films

Hina Verma

Sorbonne Université

Ecole doctorale ED388

Laboratoire de Chimie Physique – Matiére et Rayonnement

Interface Analysis of Nanoscale Thin Films

Par Hina Verma

Thèse de doctorat de Chimie Physique et Chimie Analytique

Members of the Jury

Pr. Sylvie Harel	Rapporteuse
Pr. Franck Delmotte	Rapporteur
Dr. Ian Vickridge	Examinateur
Pr. Anouk Galtayries	Examinatrice
Dr. Emmanuel Nolot	Examinateur
Dr. Emmanuelle Jal	Examinatrice invité
Dr. Philippe Jonnard	Directeur de thèse

Table of Contents

Introduction

The X-ray region extends from 0.01 nm to 10 nm (100 eV to 100 keV) in the electromagnetic spectrum. Owing to their penetration abilities, X-rays can be divided into soft (photon energy < 5keV) and hard x-rays (photon energy > 5keV). The advancement in the high brilliance and focused x-ray beams has opened new doors for diverse applications in every field of science. Today X-rays are used for medical imaging, astronomical observations, material analysis and in pharmaceuticals. The interaction of X-rays with the material is governed by the different phenomenon of reflection, absorption and transmission. Unlike the visible light, the x-rays undergo significant intensity loss after being reflected from a material. This calls for the need to design special optical systems that can be engineered to work effectively in the X-ray region. Multilayer mirrors have the great advantage of being adaptable to curved surfaces, enabling their use as reflective optics in microscopes, x-ray spectrometers and telescopes.

Located between the absorption edges of carbon (285 eV) and oxygen (530 eV), the water window range offers good optical contrast for imaging biological samples like organs or even cells with very good resolution of approximately 0.5 nm. It is because within this range, water is transparent to soft X-rays while carbon is absorbing. Within this water window range also falls the N K absorption edge at 395 eV. This particular emission range is quite intriguing as well as challenging at the same time. Interesting because the spectrometers working in this emission range caters to the analysis in diverse fields of science such as the study of DNA molecule, nitrogen based semiconductor alloys such as InN, Ga(In)AsN etc. The functionality in the low energy range (< 500 eV) possesses a challenge of achieving high resolution and high reflectivity. The existing spectral analysers fall short in operating effectively in such low energy ranges, and hence multilayer mirrors are required.

A part of this thesis is dedicated to the design of a multilayer system that can be used as spectral component for operation in the N K emission range i.e. around the N K absorption edge of 395 eV. However, the quality of interfaces is the most important parameter for the performance of multilayer optics. Interdiffusion at interfaces, formation of rough surfaces and

even in some cases presence of buried layers hinder the quality and overall optical performance of any multilayer system. Thus, it is a prerequisite to describe precisely the interlayers and have information about the interactions at the surface of the stack, in-between each layer and at the bottom layer and the substrate. Consequently, in this thesis we have characterized different Mg/Sc systems with the introduction of Cr and ZrC layers as capping and barrier layers.

Second part of the thesis focuses on the study of Fe/Si multilayer using X-ray emission spectroscopy (XES). The valence to core transitions in XES are sensitive to the chemical state of the emitting element. Until now, XES has only been applied in soft x-ray region (photon energy ≤ 2 keV) but no work has been done to investigate its sensitivity in the hard X-ray region. Therefore, in our work we take example of Fe/Si multilayer that has been extensively studied using XES only in the soft X-ray range, and compare the findings in the hard X-ray range.

Thesis outline:

This thesis comprises of four chapters and the contents of each chapter are discussed briefly in the following section.

Chapter 1: Multilayer Optics

This chapter outlines the theory of interaction of X-rays with materials via the phenomenon of X-ray reflection and X-ray fluorescence. The chapter covers the details of the theory of X-ray reflection first at a single interface and then in complex multilayer systems. It is then followed by the explanation of available methods and fabrication of thin films and multilayers. The chapter also contains detailed information on various field of applications of the multilayer mirrors. Lastly, it discusses the aim and motivation of this thesis and its scope in future.

Chapter 2: Experimental Techniques

This chapter explains in-details the different experimental techniques employed for the characterization of thin films and multilayer systems. It covers the experimental set up off the three different beamlines employed, as well as their theoretical background.

Chapter 3: Study of Mg/Sc Systems

This chapter presents the experimental findings of the characterization of different Mg/Sc systems for application as spectral components in X-ray spectrometry. Two types of systems, one with the introduction of ZrC and the other with Cr are discussed. The interface analysis for each of the thin film systems is presented using the characterization methods: X-ray reflectivity, time of flight – secondary ion mass spectroscopy and with combined X-ray reflectivity and X-ray fluorescence. The chapter concludes with the presentation of the possible multilayer mirror system, interesting for X-ray spectrometers.

Chapter 4: Study of Fe/Si multilayer

This chapter focuses on the study of Fe/Si multilayer using XES. It outlines the methodology and potential of XES in the hard X-ray range to study the buried layers and interfaces.

Chapter 1: Multilayer Optics

1.1 Introduction to X-rays

The end of 19th century marked the finding of one of the most quintessential discoveries in science – the '*X-rays*' by the German physicist Wilhelm Röntgen. Despite Röntgen's early identification of his unknown, 'X' rays as longitudinal vibrations of the ether, X-rays proved to be simply light waves, a form of electromagnetic radiation, with very short wavelengths that fall between ultra-violet and gamma rays regions. Figure 1.1 shows the electromagnetic spectrum with the X-ray region ranging from 0.01 nm to 10 nm (100 eV to 100 keV), with wavelengths across the top and energies along the bottom.

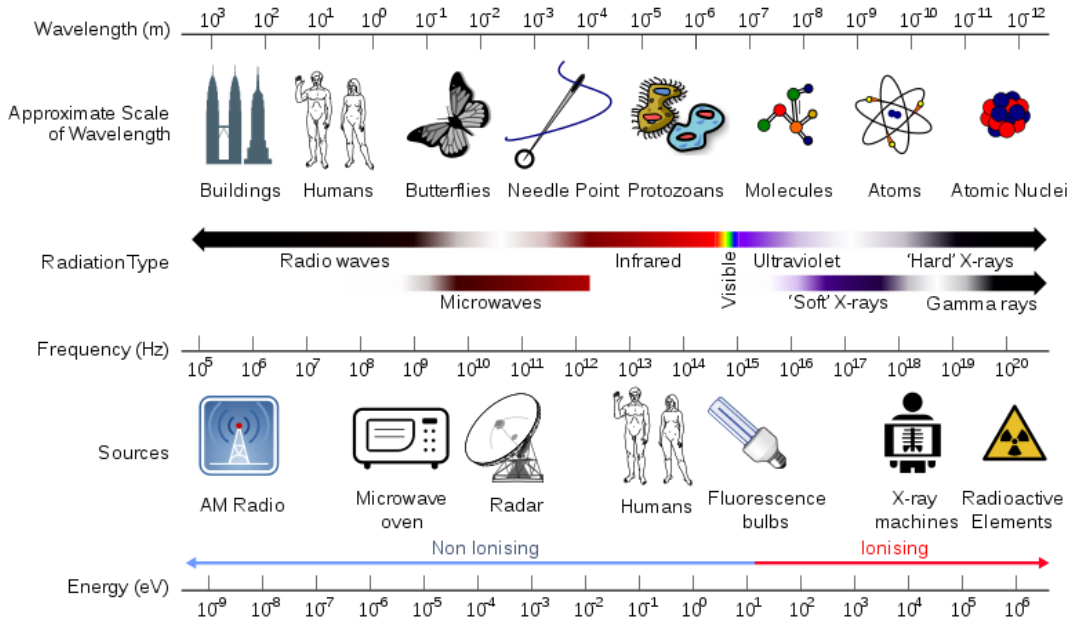

Figure 1.1 - Electromagnetic Spectrum.

With the advancement in technology, it has become possible to achieve high brilliance and focused X-ray beams with variety of applications ranging from medical imagining, astronomical observations, material analysis and in pharmaceuticals etc. Owing to their penetration abilities, X-rays can be divided into soft (photon energy < 5 keV) and hard x-rays (photon energy > 5 keV). The propagation of X-rays, as well as other electromagnetic waves,

in a material can be briefly and classically described by several phenomena. Reflection is the process by which X-rays are returned by the material. This happens either at the boundary between a medium and vacuum or air (surface reflection) or at the interior of the medium (volume reflection). Transmission (or refraction in the case of propagation through different materials) is the passage of X-rays through a medium. Absorption is the way in which the energy of a photon is taken up by matter, typically the electrons of an atom. These phenomena highly depend on the material or medium in which the X-rays travel as well as the energy of the X-rays.

1.2 Theory of refractive index

A material is characterised by its refractive index and in the x-ray region, the complex refractive index (n) is defined as $n = 1 - \delta + i\beta$. The real part of the refractive index (δ) represents the dispersion behaviour of a material with respect to its interaction with the probing photon energy, while the imaginary part (β) indicates its absorptive behaviour and in combination they are commonly known as optical constants. From a semi-classical approximation, the refractive index given by x-ray scattering inside a multi-electron atom is given by:

$$N(\omega) = 1 - \frac{e^2 n_a}{2m\epsilon_0} \sum_s \frac{g_s}{(\omega^2 - \omega_s^2) + i\gamma}$$

where n_a is the atomic density of the material, g_s is the oscillator strength, ω_s is the resonant frequency of the oscillator, ε_0 is the electric permittivity of the medium and γ is the damping factor related to the losses occurring in the oscillator. The above expression can be written in a simplified form in terms of atomic scattering factors as follows:

$$N(\omega) = 1 - \frac{r_e n_a c^2}{2\pi\omega^2}[f_1^0(\omega) - if_2^0(\omega)]$$

where r_e is the classical electron radius given by $r_e = \frac{e^2}{4\pi\varepsilon_0 m_e c^2} = 2.817 \times 10^{-5}$Å, $f_1^0(\omega)$ and $f_2^0(\omega)$ are the real and imaginary parts of atomic scattering factor, $f(\omega) = f_1^0(\omega) - if_2^0(\omega)$. In x-ray region, the energy of photon is large as compared to the binding energy of electrons,

the chemical effects are negligible and the refractive index is thus dependent on the scattering factors of the individual atom. Atomic scattering factor is a measure of scattering power of an isolated atom. It is defined as the ratio of the amplitude of wave scattered by an atom to the amplitude of the wave scattered by the electron. Total scattering amplitude from a group of atoms is given by the vector sum of the scattering amplitude from the individual atoms. In case of longer wavelengths or small scattering angles an atom is considered as a point scatterer that gives all the scattered waves in phase. The optical constants from the refractive index can therefore be given in the following form:

$$n(w) = 1 - \delta + i\beta = 1 - \frac{r_e n_a c^2}{2\pi\omega^2}[f_1(w) - if_2(w)]$$

where,

$$\delta = \frac{r_e n_a c^2}{2\pi\omega^2} f_1(\omega) \quad or \quad \delta = \frac{r_e n_a \lambda^2}{2\pi} f_1(\omega)$$

$$\beta = \frac{r_e n_a c^2}{2\pi\omega^2} f_2(\omega) \quad or \quad \beta = \frac{r_e n_a \lambda^2}{2\pi} f_2(\omega)$$

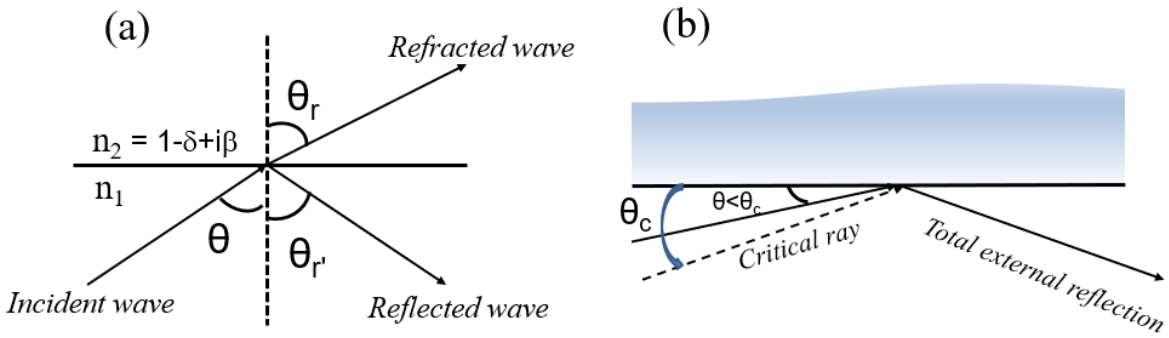

Figure 1.2 - (a) Interface geometry for incident, reflected and refracted waves. (b) Schematic of total external reflection.

The values of delta and beta are close to unity. When an X-ray beam with refractive less than 1, impinges a material surface, X-rays undergo total reflection at grazing angle smaller than the critical angle for total reflection and do not penetrate into the material. As the incident

angle increases beyond the critical angle, incident x-rays penetrate into the material by refraction. The critical angle (θ_c) can be deduced from Snell's law, following the interface geometry from figure 1.2, with θ, θ_r, $\theta_{r'}$ are the angles of incidence, reflection and refraction can be written as:

$$n_1 \cos\theta = n_2 \cos\theta_r = (1 - \delta + i\beta)\cos\theta_r$$

In case of total external reflection, the absorption is negligible, hence the contribution of β can be neglected and the incidence angle can be denoted as θ_c. Therefore, the equation above can be rewritten as:

$$\cos\theta_c = (1 - \delta)$$

Approximating $\cos(\theta_c)$ at small angles,

$$1 - \frac{\theta_c^2}{2} = 1 - \delta$$

$$\theta_c = \sqrt{2\delta}$$

1.3 X-ray reflectivity

X-ray reflectivity, is a non-destructive technique used for structural determination of nanoscale thin films and multilayers. Its principle is based on the specular x-ray reflection i.e. the incident angle should be equal to the reflection angle. Reflectivity measurement can be done in two modes: Angle dependent and Energy dependent. In angle dependent mode, the reflected photons are measured from the surface of a sample as a function of incidence angle at a fixed incident photon energy. In case of energy dependent mode, the measurement is done at a fixed angle and variable photon energy, using synchrotron source. In this technique, the incident beam needs to be monochromatic, collimated and polarization should be well defined.

The measured and fitted reflectivity curves can help determine precisely, the structural parameters along with optical constants for each layer and interlayer. When the measurement is done in energy dependent mode, we cannot only obtain structural information but also element specific information as well when measurement is done near an absorption edge. The

interaction of x-rays with the material in case of x-ray reflectivity is discussed in detail in the sections below. We start by discussing the reflection at a single interface and then proceed to explain the reflection phenomenon in case of a multilayer system, where x-rays undergo reflection and absorption at multiple interfaces.

1.3.1 Reflection at a perfect interface

The phenomenon of reflection and transmission at a perfect interface can be described by Fresnel equations [1]. The interaction of the electromagnetic wave at single interface is shown in figure 1.3. The electric field vectors for incident, reflected and transmitted waves are defined by:

$$\boldsymbol{E}_i = \boldsymbol{E}_i\, e^{-i(\omega_i t - \boldsymbol{k}_i.\boldsymbol{r})}$$

$$\boldsymbol{E}_r = \boldsymbol{E}_r e^{-i(\omega_r t - \boldsymbol{k}_r.\boldsymbol{r})}$$

$$\boldsymbol{E}_t = \boldsymbol{E}_t e^{-i(\omega_t t - \boldsymbol{k}_t.\boldsymbol{r})}$$

Where $\mathbf{k}_i$, $\mathbf{k}_r$, $\mathbf{k}_t$ are the wave vectors for incident, reflected and transmitted beam given by $k = \omega(1 - \delta + i\beta)/c$. The bold letters represent the vectors.

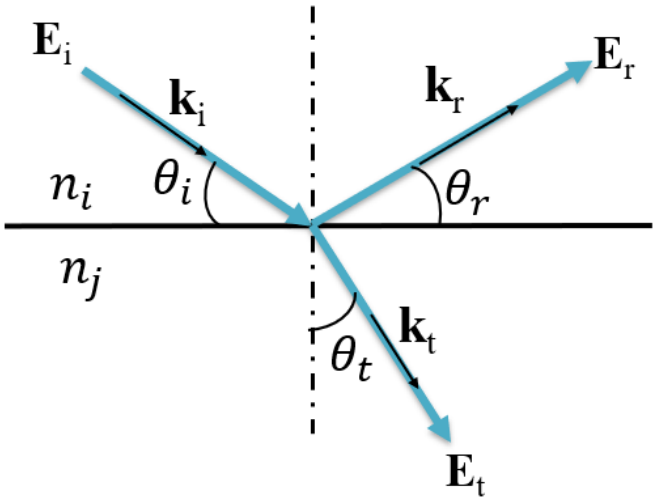

Figure 1.3 - Diagram of an incident plane wave propagating at the interface.

The reflection coefficient (r) and the transmission coefficient (t) are defined by the ratio between the amplitude of the reflected and transmitted electric fields to the amplitude of the incident electric field. The calculation of the coefficients r and t is based on the Fresnel equations as presented below considering different polarizations of the incident light:

For s-polarised incident beam, where the electric field of the incident beam is perpendicular to the incident plane, the reflection and transmission coefficients are:

$$r^s = \frac{|\boldsymbol{E_r}|}{|\boldsymbol{E_i}|} = \frac{n_i \sin\theta_i - n_i \cos\theta_t}{n_i \sin\theta_i + n_j \cos\theta_t}$$

and

$$t^s = \frac{|\boldsymbol{E_t}|}{|\boldsymbol{E_i}|} = \frac{2n_i \sin\theta_i}{n_i \sin\theta_i + n_j \cos\theta_t}$$

For p-polarised incident beam, where the electric field of the incident beam is parallel to the incident plane the reflection and transmission coefficients are:

$$r^p = \frac{|\boldsymbol{E_r}|}{|\boldsymbol{E_i}|} = \frac{n_i \cos\theta_t - n_j \sin\theta_i}{n_j \sin\theta_i + n_i \cos\theta_t}$$

and

$$t^p = \frac{|\boldsymbol{E_t}|}{|\boldsymbol{E_i}|} = \frac{2n_i \sin\theta_i}{n_j \sin\theta_i + n_i \cos\theta_t}$$

Therefore, the reflectance and transmittance of the x-ray beam can be written as:

$$R = |r|^2$$

and

$$T = Re\left\{\frac{n_j \cos\theta_j}{n_i \cos\theta_i}\right\}|t|^2$$

In reality it is impossible to achieve an ideal smooth interface, the fabrication of a thin film, bilayer, trilayer or a multilayer system leads to rough imperfect interfaces. These interfaces are prone to intermixing, diffusion, oxidation and contamination from the

environment. In the section below, we will discuss the optics in a multilayer system – its principle and the phenomenon of x-ray reflection, transmission and absorption.

1.4 X-ray optics in a multilayer system

When an x-ray beam impinges on a material surface, it undergoes major intensity loss as most of it is absorbed within the material. This problem can be solved by designing specialized optical systems such as multilayer mirrors which can be engineered to work in the x-ray range. A multilayer mirror as the name suggests is made up of a combination of two or more materials of high and low atomic number, that are arranged periodically in an alternate manner as shown in figure 1.4. Higher atomic number element is usually the absorbent material for example molybdenum or tungsten, whilst a lower atomic number acts as transparent material or known as the spacer layer, such as silicon, boron or carbon.

The performance of a periodic multilayer mirror is characterized by its reflectance and bandwidth. In this structure, the incident beam is reflected at the surface and at the first interface while the rest penetrates deeper into the stack and which is further partly reflected at the second interface, this process recurs at each interface such that all partly reflected coherent beams interfere with each other. The reflectance depends on the structure of the multilayer as well as the optical properties of the selected elements of the component layers. The design and choice of the multilayer stack is done in such a way that light reflected from each interface adds constructively to yield maximum possible reflectance.

1.4.1 Principle

The X-ray reflection inside a multilayers can be considered analogous to the diffraction of monochromatic radiation by the lattice planes of crystalline structures, defined by the Bragg's law, $n\lambda = 2d \sin\theta$. In the Bragg's equation, figure 1.4, n is the order of diffraction, d is distance between two consecutive atomic planes of the crystal (in case of multilayer this is given by the period of the stack), θ being the glancing angle and λ is the incident wavelength. The working wavelength in a natural crystal is determined by the lattice spacing between the planes, given by d. However, this spacing is very small of the order of a few tenths of nm and

a rather high value is needed to reflect x-rays that are relatively "softer" with longer wavelengths. A multilayer mirror, therefore comes into play to overcome such difficulties. Parameters such as choice of elements, the period of the stack, the number of layers, and the incidence angle can be easily be varied by choice for the design and working of mirrors with high reflectivity.

Figure 1.4 shows the schematic of the reflectivity inside a multilayer mirror. If for example at normal incidence the optical thickness (the product of the refractive index and the geometrical thickness) of all the layers, when not taking into account the absorption, is exactly equal to a quarter of the wavelength of the incoming light ("quarter-wave stack"), all the beams add up constructively and a high reflectivity can be obtained.

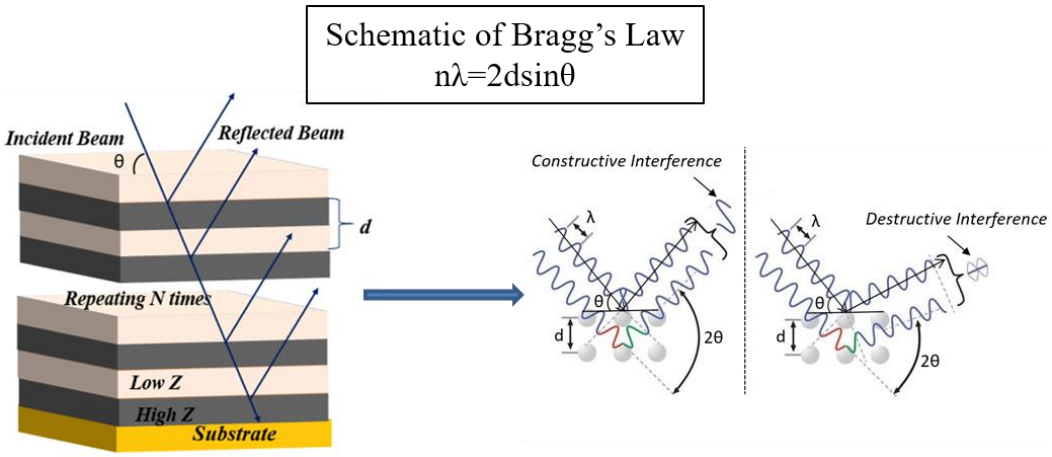

Figure 1.4 - Schematic of a multilayer (left) and of the Bragg's law (right).

The Bragg's law defined above does not take into account the refraction in the consecutive layers and at the interfaces due to dispersion. Therefore, the Bragg's law needs to be modified for the multilayer system and the corrected equation is given as:

$$n\lambda = 2d \sin\theta \sqrt{1 - \frac{2\delta_n}{(\sin\theta)^2}}$$

where δ_n is the decrement of the real part of the complex refractive index. The term δ_n is defined as the weighted average of the real part of the refractive index and is defined by the following equation:

$$\delta_n = \Gamma\delta_H + (1 - \Gamma)\delta_L$$

Where

$$\Gamma = \frac{d_H}{d_H + d_L}$$

Γ is the ratio of the thickness of layer containing heavy element (d_H) to the period of the multilayer structure ($d_H + d_L$) and δ_H and δ_L are the real part of refractive index of the high atomic number and low atomic number element [2].

1.4.2 Design of multilayers

The realisation of an effective multilayer mirror includes three important steps: design, fabrication and characterisation. Reflectivity, transmittivity and phase performance are the three parameters that are targeted for the design of multilayers for the required optical function. Material selection is the most important part of designing a multilayer structure. As we know a multilayer structure is composed of a combination of spacer and absorption layers. The selected pairs for bilayer, trilayer and quadrilayer systems must be such that the elements have strong optical contrast. The spacer layer (which is a lower atomic number element) should have low absorption coefficient at the working wavelength to obtain maximum reflection. Selection of the absorber material should be based on a maximum difference in refractive index, specifically in real part. Generally, heavy metals such as Mo, Ru, Cr, W etc. are chosen as absorber layers.

The multilayer mirrors can be tailored specifically for different application wavelengths by adjusting the period thickness and the thickness ratio Γ. The optical constants of the low Z material should be as small as possible to provide the greatest refractive index contrast with respect to that of high Z material. To obtain strong enough scattering, we can minimize the absorption by reducing the thickness of the high Z layer to have the large optical contrast.

Extremely small gamma values for thin multilayer mirrors are limited by the physical possibility to fabricate continuous sub-nanometer thick layers.

The optical performance of multilayer mirror depends largely on the interface quality defined by morphological roughness and diffusion in between two layers. The fabricated multilayer structure is usually quite different from the ideally simulated structure. A lot of factors contribute to the realisation of a multilayer structure, the primary factor being the method of fabrication of the multilayer. Even when the deposition system is well calibrated to obtain the nominal thickness deposition of each layer, the morphology of the deposited film is affected by the surface mobility of adatoms and the surface free energy of the constituting elements. A study of the interdiffusion of the constituting elements is important because it determines the tendency of elements to form compounds that will contribute to interface formation. Such information can be derived from binary phase diagrams and enthalpies of formation and diffusion coefficients.

1.5 Theory of prediction of interdiffusion – Miedema Model

The mixing enthalpy ΔH can be calculated using the Miedema model [3] to theoretically explain and confirm the existence of the interdiffusion between two layers. The mixing enthalpy for a combination of two transition metals, say x and y can be predicted by using the following expression:

$$\Delta H = \frac{2Pc_x f_x^y V_{xy\ alloy}^{2/3}\left[-\left(\phi_x-\phi_y\right)^2+\frac{Q}{P}\left(\left(n_{ws}^x\right)^{1/3}-\left(n_{ws}^y\right)^{1/3}\right)^2\right]}{\left(\left(n_{ws}^x\right)^{-1/3}+\left(n_{ws}^y\right)^{-1/3}\right)}$$

where

$$f_x^y = C_x^s, for\ solutions$$

$$f_x^y = C_x^s\left(1+8\left(C_x^s C_y^s\right)^2\right), for\ ordered\ alloys$$

$$c_x^s = c_x V_x^{2/3}\left(c_x V_x^{2/3}+c_y V_y^{2/3}\right)$$

$$c_y^s = c_y V_y^{2/3}\left(c_y V_y^{2/3} + c_y V_y^{2/3}\right)$$

Here, P and Q are the constants, such that p =14.1, Q/P = $9.4V^2/(\text{d.u.})^{2/3}$, c_x and c_y are the mole fractions, (c_x+c_y=1), V_x and V_y are the atomic volumes of elements x and y, respectively, ϕ is the electronegativity of components x and y and n_{ws} the electron density at the boundary of the Wigner-Seitz cell as derived for the pure elements in the metallic state. The electron densities are usually given in terms of density units (d.u.), where 1d.u.=$6.75\text{x}10^{22}$ electron/cm^3. $C_x^s and\ C_y^s$ are the surface densities of atoms x and y respectively. f_x^y is a measure to which the atoms of element x are in contact with atoms of element y. The first term representing the difference in electronegativity between the two elements x and y is the measure of the charge transfer between the two elements and shows the tendency for compound formation. The second term gives the discontinuity in electron density at the Wigner-Seitz boundary of atoms x and y. This part shows the tendency of phase separation. Alloy formation between the two elements changes the volume of each of the constituting elements and therefore the new volume is given by [4]:

$$V_{alloy}^{2/3} = V_{pure\ metal}^{2/3}\left[1 + a f_y^x(\phi_y - \phi_x)\right]$$

where the constant a is experimentally determined whose value is 0.10 for Mg, 0.07 for Sc and 0.04 for Fe, Si and Cr. The values of ϕ, n_{ws} and V for different elements studied in this thesis are given in table 1.1. Using the above equations and constants the mixing enthalpy ΔH, is calculated for different systems studied in this thesis. If the value of ΔH is negative for a combination two elements, then they are prone to mixing and compound formation. The mixing enthalpy values associated with each of the element combinations will be discussed for different systems in the following chapters 3 and 4.

Table 1.1 - Constants used in the calculation of mixing enthalpy according to the Miedema [4].

Element	Φ (V)	n_{ws} (d.u.)	V(cm^3/mol)
Sc	3.25	2.05	15.03
Cr	4.65	5.18	7.23
Mg	3.45	1.60	14.00
Fe	4.93	5.55	7.09
Si	4.70	3.38	8.60

1.6 Reflection and transmission

In the case of a multilayer system, the phenomena of reflection and transmission occurs repeatedly at each interface between two consecutive layers. The calculation of the specular reflection inside a multilayer mirror can be done by two methods – kinematical theory and dynamical theory. In the former method, multiple reflections and the depletion of the incident beam can be neglected if the reflectivity at each boundary and the total reflectivity of the structure are small. In this approximation the reflectivity is simply calculated as the vector sum of the reflected amplitudes of the individual boundaries and therefore cannot be used to accurately predict the performance of multilayer mirrors. The dynamical theory on the other hand takes into account all the interactions occurring at each interface and the reflectivity of a multi-layered structure can be calculated either by iterative or matrix methods. These two methods are based on solving Maxwell's equations with the appropriate boundary conditions. The iterative method initially developed by Parratt [5] was latter updated by Underwood et al. [6]. It is an optical approach to the problem based on the use of Fresnel equations. These methods are well suited for the reflectivity analysis because they make it possible to easily introduce and study structural imperfections such as variations thickness, interface layers or roughness. It is important to note that between the iterative method and the matrix method, only the mathematical formalism differs. For this reason, we will describe in detail only the

generalized Parratt theory. The reflectivity data studied in this work has been analysed by using the iterative method in the software developed by D. Windt [7].

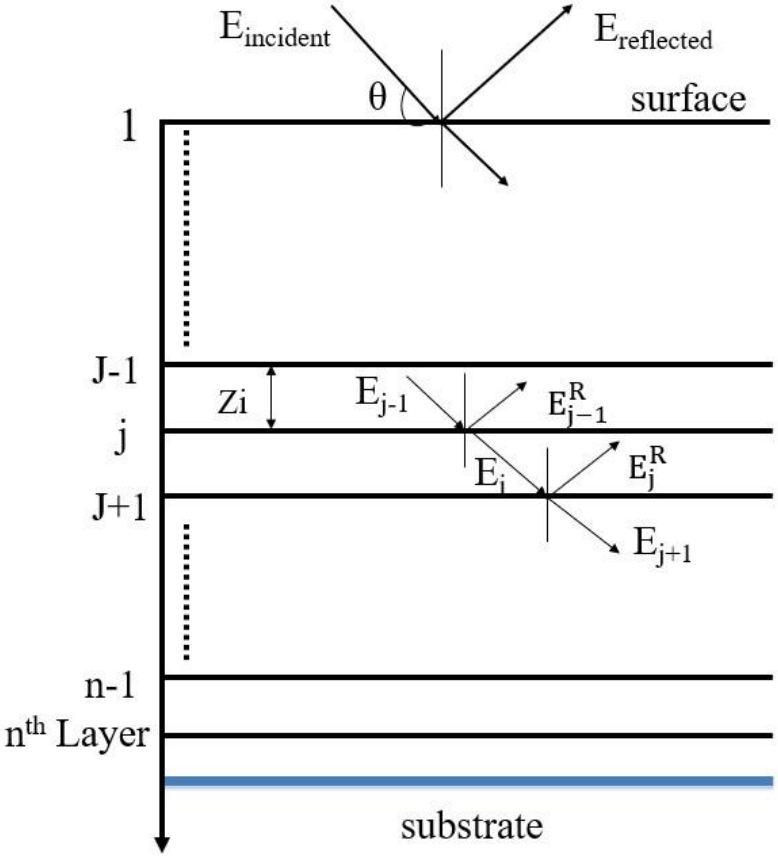

Figure 1.5 - Diagram of a N-layer stack with a photon beam propagating within the multilayer stack.

We consider a photon beam incident with the wavelength λ on a multilayer stack of N layers, shown in figure 1.5, where the j^{th} layer has a thickness z_j and refractive index n_i. Let $|\boldsymbol{E_j}|$ be the amplitude of the electric field of the incident wave at the interface between j^{th} and $(j+1)^{th}$ layer and $|\boldsymbol{E_r}|$ is the amplitude of the reflected wave. The net reflection and transmission coefficients for s and p polarisation are

$$R^s_{j,j+1} = \left|\frac{E^r_j}{E_j}\right| = \frac{g_j - g_{j+1}}{g_j + g_{j+1}}$$

and

$$R_{j,j+1}^{p} = \left|\frac{E_j^r}{E_j}\right| = \frac{\left(g_j \middle/ \boldsymbol{n}_j^2\right) - \left(g_{j+1} \middle/ \boldsymbol{n}_{j+1}^2\right)}{\left(g_j \middle/ \boldsymbol{n}_j^2\right) + \left(g_{j+1} \middle/ \boldsymbol{n}_{j+1}^2\right)}$$

Where, $g_j = \sqrt{\boldsymbol{n}_j^2 - (\cos\theta)^2}$, in which θ is the glancing angle and $\boldsymbol{n}_j$ is the complex refractive index for the j[th] layer. The coefficients of reflection are related to the Fresnel coefficients by:

$$R_{j,j+1} = a_j \, F_{j,j+1}$$

where a_j is the phase term and depends on the thickness of layer j. Using continuous boundary conditions at the interface, the tangential components of electric and magnetic fields can be obtained by the recurring relation:

$$R_{j,j+1} = a_j^4 \frac{R_{j,j+1} + F_{j,j+1}}{R_{j,j+1}F_{j,j+1} + 1}$$

The recursion starts at the substrate with $R_{n,n+1=}0$ and ends at the surface layer with $g_1 = \sin\theta$. The reflectance and the intensity reflected by the whole multilayer structure is given by:

$$I(\theta) = I_0 R, \text{ where } R = \left|R_{j,j+1}\right|^2$$

1.7 X-ray standing wave

The concept of X-ray standing wave was first mentioned by B. W. Batterman in the 1960s. A standard X-ray standing wave is generated by the interference of the incident and reflected x-ray beam under Bragg's condition generating a periodic electric field perpendicular to the multilayer stack, shown in figure 1.6. The formation of the x-ray standing inside the multilayer is similar to that of the mechanical standing waves generated by a vibrating string with nodes and anti-nodes. In case of X-ray standing wave, the nodal plane corresponds to a point of decreased electric field amplitude while the electric field is enhanced at the anti-nodal

plane. The period of this electric field D is related to the wavelength of the X-ray beams and their directions and is given by the formula:

$$D = \frac{\lambda}{2\sin\theta} = \frac{2\pi}{Q}$$

where λ is the wavelength of the two X-ray beams, Q is the difference of their wave vectors (K_H and K_0) and 2θ is the angle between them.

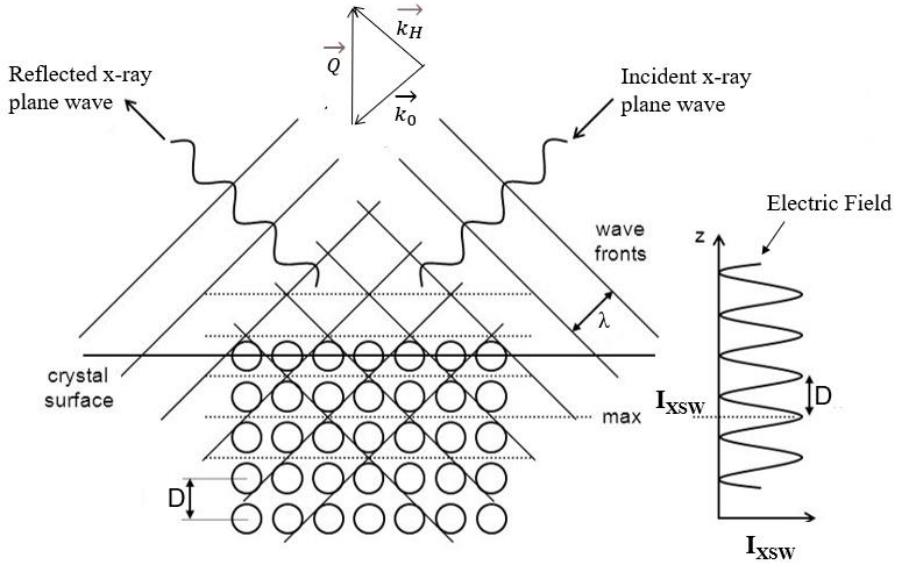

Figure 1.6 - Scheme of the X-ray standing waves resulting from interference of incident and reflected wave with the generation of perpendicular electric field inside the structure [8].

If the wavelength of the incident X-ray is known and the grazing incident angle is fixed at the first order Bragg angle corresponding to the period of the periodic structure, then the period of the electric field will be equal to the period of the material and the anti-nodal planes will be located at each interface of the neighbouring planes [8].

In figure 1.7, is the simulation showing the progression of electric field intensity inside $B_4C[Pd/Y]_{x40}$ multilayer at an incident energy of 10keV. From the figure we can see that as the grazing incidence angle (θ_i) is varied around the Bragg angle (θ_{Bragg}) the anti-nodal planes of

electric field move accordingly inside the different layers. The anti-nodal planes are located in the B_4C capping layer as well as the Y layers, for incidence angle smaller than the Bragg angle.

When the angle is set at the Bragg angle, the anti-nodal planes are present at the interface of each layer and when the angle is increased beyond the Bragg angle, the planes move towards the Pd layers [9]. In this way, the ionization is enhanced in the layers where anti-nodal planes are located, while reduced ionization can be found at the nodal planes. The electric field intensity fades as the incidence angle moves from the Bragg angle due to loss of reflectance. The change in ionization can be experimentally observed by measuring photoemission, X-ray emission or Auger emission as a function of grazing incidence angle.

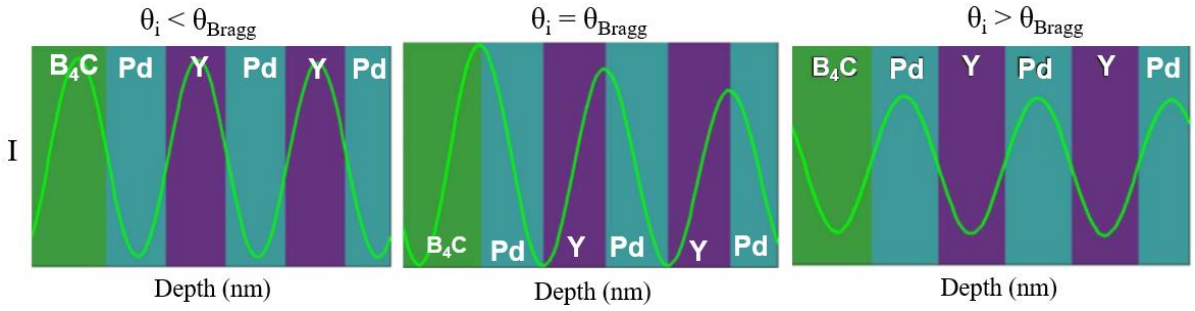

Figure 1.7 - Electric filed intensity represented by green line inside $B_4C[Pd/Y]_{x40}$ multilayer at photon energy of 10 keV as a function of depth [9].

1.7.1 X-ray standing wave enhanced hard x-ray photoelectron spectroscopy

X-ray photoelectron spectroscopy is based on the measurement of kinetic energy of electron ejected from the core level of the atom with an incident photon beam. The conservation of energy in during the process is given by the equation:

$$h\nu = E_K + E_B + \phi$$

where $h\nu$ is the energy of the incident photons, E_K is the kinetic energy of the ejected electron, E_B is the binding energy of the electron and ϕ is the work function which represents the energy required for the electron to escape the Fermi level to the vacuum [8]. The kinetic energy analysis of the emitted electron yields information on binding energies of emitted electron. The binding energy is dependent on the environment of the species and is

characteristic of its chemical state. The information about the chemical state of an element is seen in the "chemical shift", from its nominal position on XPS spectrum. Hard x-ray photoelectron spectroscopy (HAXPES) is an extension of conventional XPS technique. In HAXPES, the probing depth is much higher due to the long inelastic mean free path of the emitted electron because of their high kinetic energy [8]. Hence, it presents an advantage in studying the buried layers and interfaces.

By exploiting the chemical shifts in photoelectron binding energies, the use of XPS combined to XSW allows us to not only obtain element-specific but also chemical state-specific structural information from surfaces. This approach has been used to probe the composition, magnetization and electronic densities of states in buried layers and interfaces of spintronics and other nanostructures. This approach has also been applied to study the multilayer optics for the characterisation of multilayer mirrors. An example is the analysis of different systems of Pd/Y multilayer mirror, studied by Meiyi Wu et. al. [9], with B_4C introduced as the capping and barrier between the Pd and Y layers. B_4C was introduced as capping layer on top of Pg/Y layers, as a barrier layer between the Pd and Y layers and as both capping and barrier layer. The different types of multilayers are shown in figure 1.8 (b), (C) and (d). The XSW obtained by integrating the intensity of each experimentally measured photoemission spectra of Pd $2p_{3/2}$, Y $2p_{3/2}$ and B 1s and is plotted as a function of grazing incidence angle taken around the 1^{st} Bragg angle.

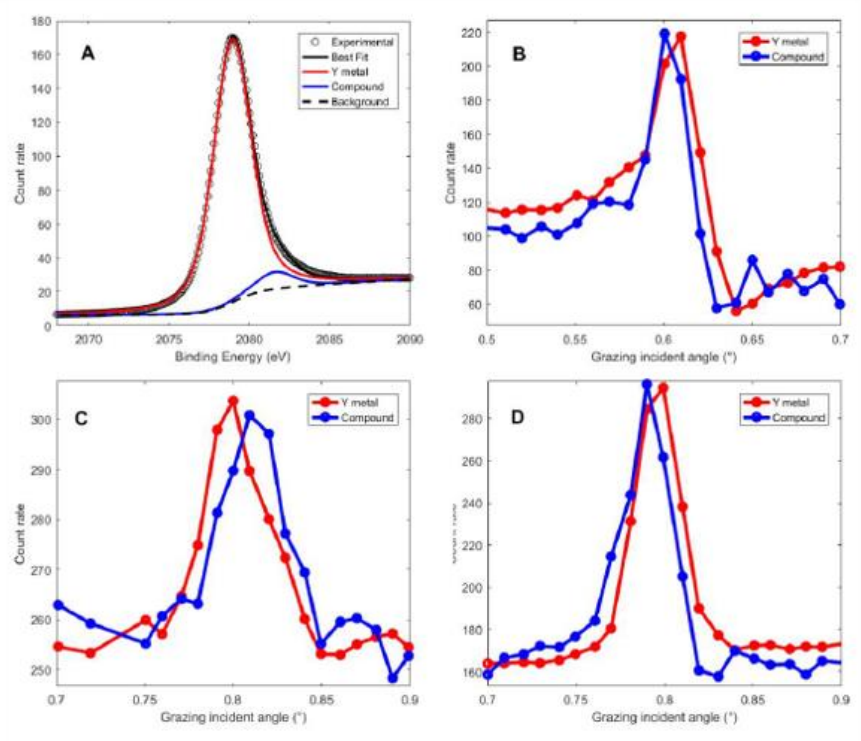

Figure 1.8 - (a) Y 2p3/2 photoemission spectra. (b), (c) and (d) show HAXPES-XSW curves extracted from measured photoemission spectra of Y 2p3/2, for different multilayer systems [13]. The curve in red is of the pure Y-metal layer and the curve in blue corresponds.

Figure 1.8 shows the HAXPES-XSW curves for Y metal and the compound formed due to interdiffusion as extracted from $2p_{3/2}$ photoemission spectra for different multilayer systems. It was found that the interface Y-on-B_4C and B_4C- on-Y results in the formation of a compound which could be either Y-C or Y-B, this can be seen in figure 1.8(a) in the photoemission peak of Y (in red) and the compound (in blue). Figure 1.8(b), shows that the HAXPES-XSW curve of the compound shifts towards the higher angles as compared to Y metal, indicating that such compound is located deeper than Y metal in each period that is on Y-on-B_4C interfaces. In Figure 1.8(c), the curve belonging to the compound shifts towards the lower angles which means it is located at a shallower depth than the Y metal, that is at B_4C-on-Y interfaces. Hence, it was inferred that the interfaces, B_4C-on-Y and Y-on-B_4C are asymmetric and compound formation preferably happens at B_4C-on-Y interfaces. It is because Y-B and Y-C compound are

expected to present similar Y2$p_{3/2}$ shifts. The HAXPES-XSW for Pd 2$p_{3/2}$ curves were also measured and analysed in a similar manner and no compound formation was seen at Pd and B_4C layers. Hence, a detailed description of the depth distribution of each element can be obtained by the HAXPES-XSW measurement.

1.7.2 X-ray standing wave coupled to X-ray fluorescence spectroscopy

The fluorescent x-rays emitted from a material by irradiation of energetic incident beam, can be measured by two types of detection systems: *wavelength dispersive X-ray fluorescence* (WDXRF) and *energy dispersive X-ray fluorescence* (EDXRF). X-ray fluorescence is the emission of characteristic X-rays due to the electronic transition between valence and core levels of an element of interest. In EDXRF the spectral resolution is poor (125 eV at best): this does not allow to observe the chemical shift of the fluorescence lines. WDXRF involves the detection of fluorescent X-rays within a particular energy range given by diffraction from a single crystal or a multilayer mirror. Fluorescence measurement in this mode, gives chemically sensitive depth distribution of an element inside the material owing to the good spectral resolution (of the order of the eV). WDXRF also offers high spectral resolution with access to the analysis of low Z elements as well. WDXRF can be exploited further in combination with the formation of XSW above and below the sample surface. Therefore, measuring WDXRF intensities while varying the glancing angle and hence modulating the electric field inside the stack allows us to probe the structure from top to bottom along with elemental and chemical sensitivity. Hence, the aim is to achieve chemical sensitivity as seen in HAXPES-XSW, by formation if XSW in the WDXRF mode for high resolution.

1.8 Fabrication techniques

The quality of interfaces is the most important parameter for the performance of multilayer optics. Perfect interface would require that the growth of one atomic plane start only when the previous plane is completely filled. The accurate control of the period and the quality of each layer are of major importance for the optical properties. This requires a good control of the fabrication techniques used for depositing the multilayers. The deposition techniques

determine virtually all the properties of the thin films and multilayer systems and can also be used to modify the existing properties. The process of thin film deposition can be classified in two parts: Physical Vapour Deposition (PVD) and Chemical Vapour Deposition (CVD). PVD is described as a process in which a material in its condensed phase goes to a vapour phase and then back to condensed phase in the form of thin film on top of a substrate under vacuum. The most common PVD processes are evaporation and sputtering. In CVD the substrate is exposed to one or more volatile precursors that react or decompose on the substrate surface to form the desired layer. The volatile by-products formed are then removed by gas flow through the reaction chamber [10,11]. CVD is characterised into different sub classes of deposition techniques that differ by the means by which the chemical reactions are initiated, such as plasma enhanced CVD, thermal CVD, laser CVD, atomic layer deposition etc. PVD and CVD are largely employed in the semiconductor industry for the fabrication of solar cells, microelectronics and are used for thin film or multilayer coatings. Commonly, PVD processes are used to deposit thin films and multilayers with thickness in the range of a few nanometres to a thousandth of nanometres by evaporation and sputtering techniques [12]. The following section will discuss briefly these fabrication techniques.

1.8.1 Evaporation

The method is commonly used for the deposition of thin films. It is based on the general process of the change of phase of the material from solid phase to vapor phase and then converting again to solid phase onto a substrate. the deposition process takes place under vacuum or in controlled atmospheric condition. The target material used for the deposition is vaporised by the different means of heating which includes resistance heating, heating by electron gun etc. The evaporation techniques are classified into three types namely – resistive evaporation, electron beam evaporation, laser beam evaporation (pulsed-laser deposition) and molecular beam epitaxy. Amongst all these methods, we will only discuss the electron beam evaporation as it the most widely used method for thin film and multilayer mirror deposition.

1.8.2 Electron beam evaporation

In this technique the target material is bombarded by high energy electron beam from a charged heating filament (of tungsten material) to evaporate and convert it to a gaseous state for deposition onto the target material. The process takes place in a high vacuum chamber, and these atoms or molecules in a vapor phase condense to form a thin film. This technique has various advantages. Most importantly, it can yield higher deposition rates - from 0.1 nm per minute to 100 nm per minute - resulting in higher density film coatings with increased adhesion to the substrate. The e-beam evaporation method also permits the direct transfer of energy with the electron beam to the target material to be evaporated making it ideal for metals with high melting points [13].

1.8.3 Sputtering

Sputtering is a prominent deposition method among the PVD processes. It's a non-thermal vaporization process wherein energetic gas ions (e.g. argon) impinge on the target material, as a result of which the atoms or molecules are ejected from the target through momentum transfer. The sputtered atoms from the target traverse the vacuum chamber and condense on the substrate surface thereby forming a thin film. This process of deposition is known as sputtering. Unlike evaporation, the source is no longer created by thermal but by ion impact on the target. Also, the target to substrate distance is shorter and, hence offers more functionality and performance like improved adhesion and thicker film as compared to electron beam evaporation. The two commonly used sputter deposition techniques namely: ion beam sputtering and magnetron sputtering have been discussed briefly in the following sections.

1.8.4 Ion beam sputtering

It is a physical deposition technique in which an ion source is used to generate an energetic ion beam that sputters a target in proximity to the substrate. The ion source consists of both cathode and anode which are aligned to each other. On applying a high voltage of 2-10 kV, an electrostatic field is created inside the ion source as a result of which the injected argon gas ionizes, creating plasma inside the source region.

The ions are then accelerated from the anode region to the cathode resulting in the formation of an ion beam. The ion beam hits the target material and sputters the target material towards the substrate via the sputtering mechanism as shown in Figure 1.9.

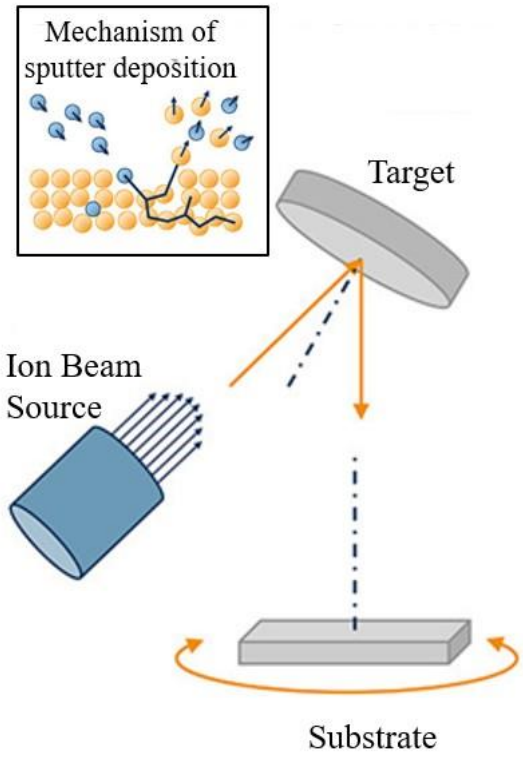

Figure 1.9 - Schematic of the Ion beam sputter deposition process.

One of the most important advantages of this technique is good quality film, which is firmly bonded to the substrate along with high precision on the deposited thickness of the film, preferable density and adhesion to the substrate [14]. A two-ion beam configuration system can be used to have better stoichiometry and density of thin films. The technique also offers the advantage of the utilization of additional flowing gases like oxygen, nitrogen etc. for the growth of oxides and nitrides thin films [15].

1.8.5 Magnetron sputtering

Magnetron sputtering is the most widely used technique for the deposition of thin film and multilayer systems. This technique allows the deposition of metals, alloys, ceramic and

polymer thin films. Magnetron sputtering is divided into two types depending on the excitation source: direct current (DC) and radio frequency (RF) sputtering. DC magnetron sputtering is used to deposit the conductive materials while RF magnetron sputtering can be used for the deposition of conductors, semiconductors and insulating materials. A diagram of DC magnetron sputter process is presented in figure 1.10. The deposition system is placed in a vacuum chamber which is initially evacuated to a base pressure and filled with argon gas. In this process, the target is held at a negative potential and an electrically neutral argon gas is first ionized by the electric field between the cathode (the target) and anode (the substrate). A positively charged plasma is formed and is accelerated by the electric field. When plasma hits the target, atoms are ejected from the target surface as a result of momentum transfer and then condense onto the substrate material. The characteristics of the deposited film depends strongly on the transport of the ions, the transferred momentum, and the deposited energy on the substrate [16,17].

The substrate is rotated so that the thin film can be deposited homogenously and kept directly above of different targets with different exposure times during the course of deposition. Magnetron sputtering techniques offers several advantages over electron beam evaporation [18] as the deposited atoms have higher kinetic energy (about 10 eV, two orders of magnitude higher than electron beam evaporation) so that the deposited films are denser and smoother. With this technique it is possible to deposit laterally gradient thin films or multilayers on substrate with precise control on thickness of individual layers by controlling the sputtering time.

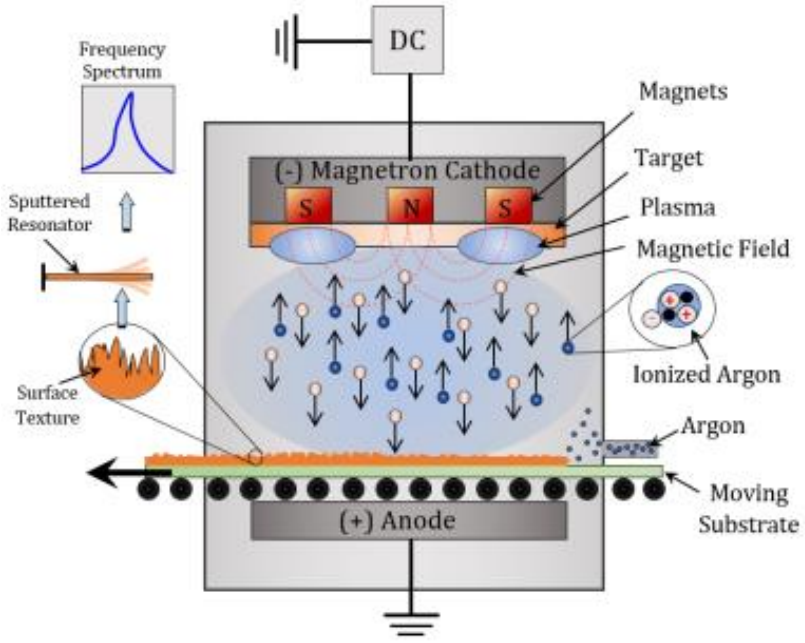

Figure 1.10 - Configuration of a DC-powered magnetron sputtering [19].

In the present thesis work all the samples were prepared using magnetron sputtering and ion beam sputtering setups, the details of which will be discussed further in chapter 2.

1.9 Applications

The application of a multilayer depends on its working energy or wavelength. Multilayer mirrors have the great advantage of being adaptable to curved surfaces, enabling their use as reflective optics in microscopes, x-ray spectrometers and telescopes. In the following we will give some examples of application of multilayer mirror in scientific research and industry.

1.9.1 Astronomy

Normal incidence multilayer mirrors have been used to obtain high-resolution astronomical images. For the past two decades, normal incidence multilayer telescopes have been installed on a number of solar physics satellites and sounding rocket instruments. One example is a Cassegrain type telescope, shown in figure 1.11(a) comprising a large concave primary mirror and a small convex secondary mirror. Periodic multilayer coatings that operate near normal incidence deposited onto super-polished mirror substrates are used to construct

mirrors for application in such type of telescopes [19,20]. Figure 1.11(b) shows the image of the Hinode/EIS instrument, equipped with broad-band Si/Mo EUV multilayers as gratings and mirrors coating for high-resolution solar spectroscopy [21].

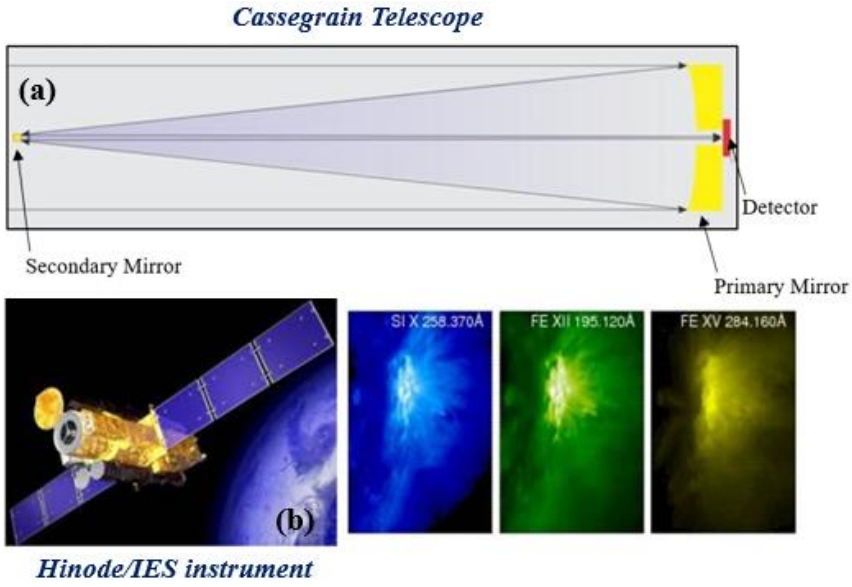

Figure 1.11 - (a) Illustration of a Cassegrain telescope (top); (b)the Hinode/EIS instrument that used multilayer-coated gratings and mirrors to perform high-resolution EUV spectroscopy of the solar atmosphere (bottom) [22].

Multilayer mirrors can be tailored to provide images at strong extreme ultra-violet (EUV) lines in the sun and stars, making them more efficient use of the telescope aperture in comparison to grazing incidence optics. Franck Delmotte et al. [22] reported the development of Al/Mo/SiC and Al/Mo/B_4C multilayers with the reflectance of 56% at 17.4 nm, as good candidates in solar orbiter extreme ultra-violet imaging telescopes. Mo/Si multilayer coatings also developed by the same team, have been employed for solar imaging in SOHO EIT and STEREO EUVI telescopes [23]. When compared to grazing incidence optics, normal incidence multilayer mirrors have reduced scattering, are less prone to geometrical aberrations, are less expensive to manufacture, mount and align. As a result, it is conceivable to approach the diffraction resolution limit for such systems. The small size and low cost of multilayer telescopes, capable of high-resolution observations, allow for the employment of many

telescopes and hence the study of plasma across a wide temperature range, even in a small rocket-borne instrument package [24]

1.9.2 Extreme ultra-violet lithography

Lithography has now become a renowned and most widely used technique in the semiconductor industry to copy patterns for manufacturing processors and memory devices for modern computing systems. Thus, increasing the resolution of the lithography equipment employed in the industry and the associated decrease in the working wavelength of the required light beam has now become the goal of the industry. Hence, multilayer mirror coatings which reflect EUV radiation are a key enabling technology for EUV lithography. Mo/Si multilayers with the reflectivity of 67.5% at 13.4 nm and Mo/Be multilayers with 70.2% reflectivity at 11.3 nm of wavelength, are one of the most popular candidates for application in EUV lithography [24,25].

1.9.3 Microscopy in the water window range

Periodic multilayer mirrors have potential application as optical components in x-ray microscopy, particularly, working in the water window region. The water window range, located between the absorption edge of carbon (285 eV) and oxygen (530 eV), makes it a powerful method for imaging samples due to natural optical contrast between water and carbon. Since the energy is lower than the oxygen absorption edge, hence in this range the water is transparent to the soft X-rays while yet carbon is absorbing. Therefore, radiations having energies in water window range could be used in X-ray microscopy for imaging living specimens like organs or even cells with very good resolution (~0.5 nm). The water window X-ray microscope has been widely developed based on the synchrotron radiation sources [26] and lab-based X-ray sources [27], using either the classic imaging optical system or the new diffraction imaging technique [28]. In all of these, X-ray optics form the most important components to focus the photons to the sample and transport the scattered ones to the detector. These multilayer mirrors work at near-normal incidence in X-ray microscopes. They are either used as the collector or objective lens for the microscope. $[CrN_x/B_4C/Sc]_{x400}$ multilayer with a

peak reflectance of 23% at near normal incidence at 397 eV, has been reported to be used as interference coatings for application in soft x-ray microscope for biological studies using a near-normal incidence Schwarzschild objective [29]. Cr/Ti, and Cr/V are some of the examples of the multilayers that presented reflectivity of 32% in the water window range [30,31]. Figure 1.12 shows an example of a soft X-ray full-field transmission microscope working in the water window range equipped with a $[W/B_4C]_{x200}$ multilayer and an image of a diatom taken with the set up[27].

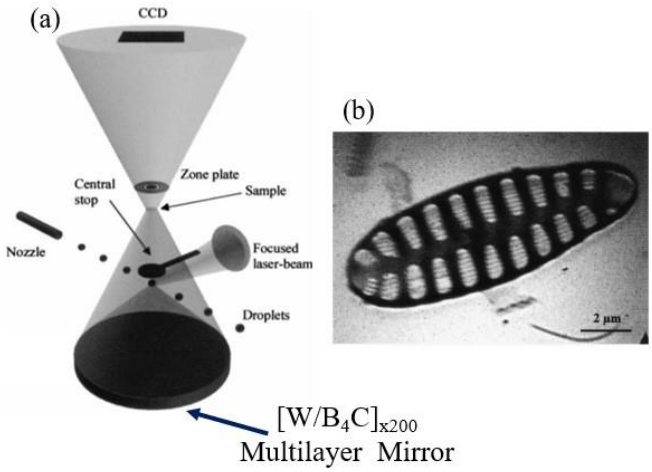

Figure 1.12 - (a) Representation of table-top water-window x-ray microscopy arrangement with $[W/B_4C]_{x200}$ multilayer mirror shown at the bottom; (b) image of diatom [28].

1.9.4 Spectroscopy

Multilayers also find application as optical components in various spectrometers. In order to study a particular wavelength, the dispersion element is positioned at the Bragg's angle to reflect the radiation and spectrum emission of the material is then recorded. The choice of constituting elements, the period and the number of bilayers highly influence the performance of the multilayer mirrors as spectral components. For example Cr/Sc multilayers have been designed to be used as Bragg dispersive devices for the analysis in wavelength dispersive spectrometry of samples containing N or Sc atoms [30]. Be/Si/Al multilayer system is another example of a specially designed multilayer to perform x-ray spectroscopy in the Li K emission range [32]. Figure 1.13, shows the comparison of B Kα emission spectra (dotted line) and the

measured reflectivity curve (dashed line) in the same graph obtained from boron with [B/Si] multilayer (shown in (a)) and [Ni/C] multilayer (shown in (b)). It can be clearly seen from the figure 1.13, that the spectra obtained using [Ni/C] multilayer has higher intensity with a high reflectivity of 25% as compared to the spectra obtained with the other multilayer. [Ni/C] multilayer also presents a higher peak-to-background ratio (7.1 for Ni/C and 6.1 for B/Si) and a higher resolving power $\lambda/\Delta\lambda$ (22.9 for Ni/C and 20.4 for B/Si) [33].

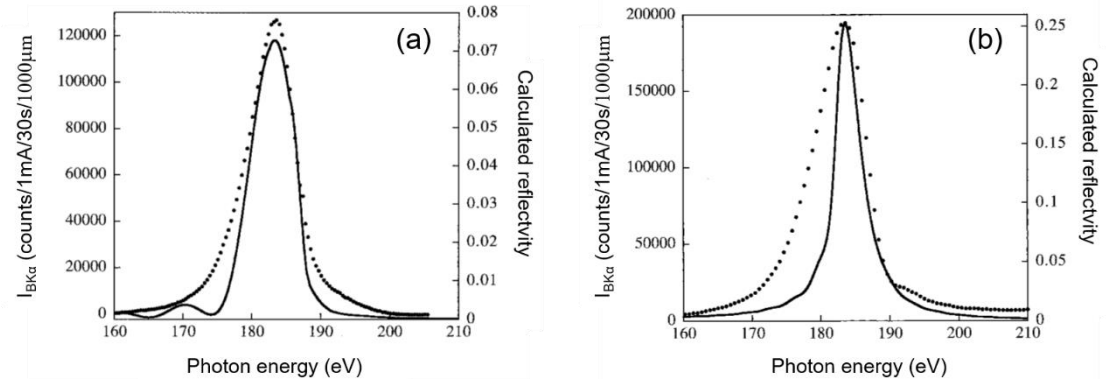

Figure 1.13 - B Kα emissions from boron (dotted line) and measured reflectivity curve (solid line) using (a) [B/Si] and (b) [Ni/C] multilayer mirror [34].

1.10 Scope of this thesis

The nitrogen K emission range is quite interesting for study in different streams of science, from the study of biological samples, to semiconductor devices and many more. Figure 1.14(b) shows an example of measured resonant inelastic X-ray scattering (RIXS) spectra near nitrogen K absorption edge for DNA molecule (in figure 1.14(a)). The measurement is done to investigate the electronic structure of B-DNA (dried double-strand DNA) and (X)·M-DNA (metal ions incorporated inside the helix, with X = Co, Ni). The well-defined, sharp peaks of the nitrogen RIXS spectra indicate localized occupied electronic states in B-DNA. The broadening of these features directly suggests delocalization of the occupied electronic states in the (X)·M-DNA systems [34]. Understanding the conductive pathways in DNA systems is a prerequisite for manipulating biomolecules for applications in domains like nanoelectron physics.

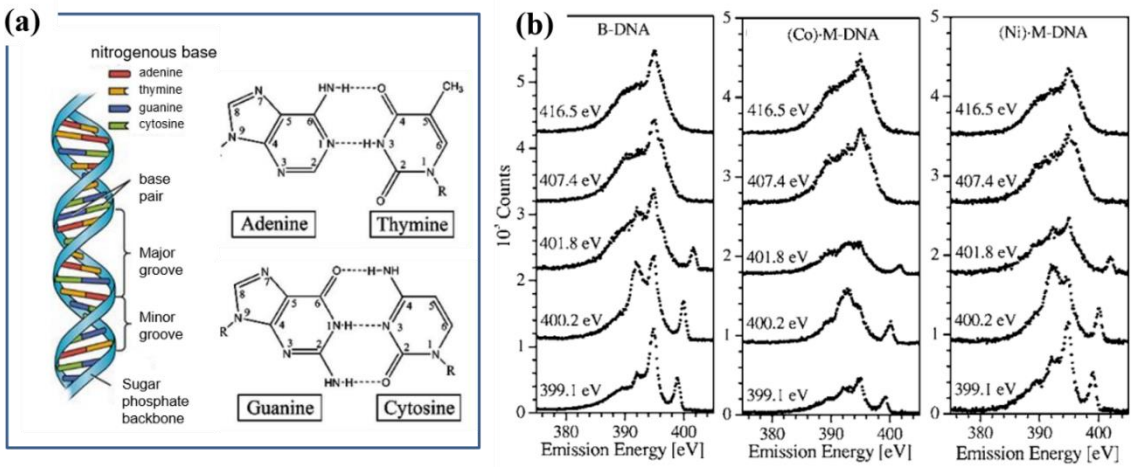

Figure 1.14 - (a) Structure of a DNA molecule with the phosphate ribbons demonstrating the helical shape, with adenine-thymine and guanine-cytosine nitrogenous pairs shown on the right (b) Nitrogen RIXS spectra of B-DNA, (Co).M-DNA and (Ni).M-DNA, with the excitation energy displayed on each spectrum [34].

Nitrogen based semiconductor alloys, have proved to be highly efficient and find exciting applications as optoelectronic devices such as light emitting diodes (LED) and laser diodes (LD) and spin electronic devices. Electronic structure, band gap calculations of various semiconductor alloys such as InN, Ga(In)AsN, $Ga_{1-x}Mn_xN$, $[Ga_{1-x}Zn_x](N_{1-x}O_x)$, SiON/SiC have been studied using X-ray emission spectroscopy with N Kα and O Kα emissions [35,36]. We can now understand how the characterization of materials in the nitrogen K emission range can help determine important information about different materials. However, the available spectrometers equipped with diffraction grating are not very efficient as the reflectance achieved is quite low. Also, since most of the grating spectrometers are set up on synchrotron beamlines, they are harder to access for study. Hence, we must consider the use of spectrometers equipped with a crystal and multilayer mirror.

An important factor for a crystal analyser, to be used as a spectral component is that the λ/2d value should be less than unity. Table 1.2 lists commonly used crystals as dispersive elements and gives information about their lattice spacing and their respective area of applicability. Most crystals work in the hard x-ray region, owing to small d. The x-ray

wavelength dispersive analysis of light elements cannot be achieved using natural crystals because their interplanar spacings are smaller than the wavelength of the characteristic radiations emitted by these elements. However, a few crystals belonging to the family of acid phthalates (listed in table 1.2) having comparatively large d spacing (up to the order of ~26 Å) scatter soft x-rays with energy up to ~ 500eV, making it possible to resolve characteristic x-rays for low Z elements like O, F, Si, Na, Mg, Al, and Si, provided the spectrometer can work at large Bragg angles, i.e., higher than 60°.

On the other hand, multilayer systems can be specifically designed with large periods to diffract x-rays in the soft x-ray range in order to overcome the limitations of the grating and crystal spectrometer. The design of the multilayer is done such that the alternating layers of the multilayer mirror must be a combination of weakly absorbing materials in order to increase the extinction depth of soft x-rays and spectral selectivity and hence decrease the bandwidth.

Cr/Sc Periodic multilayers have been studied for application as Bragg dispersive devices for the analysis in wavelength dispersive spectrometry at the N K x-ray emission (392.4 eV) with peak reflectivity of 16.9% at glancing incidence angle of 45°. The Cr/Sc multilayer mirror was tested in the crystal based spectrometers to the x-ray emissions in the water window of different samples containing N and Sc atoms: BN, CrN, Sc_5Si_3, and ScN [30]. Mg/Sc multilayers with and without Co barrier layer have also been studied for application in the N K range. Out of those systems, Sc/Co/Mg/Co multilayer displayed promising results with an expected reflectivity of 32% in the nitrogen K range. However, it was found that strong interdiffusion takes place at the Mg-on-Sc and Sc-on-Co interfaces, leading to limited reflective properties [37].

The formation of mixed zones on the layer interfaces during deposition strongly affects the layer thickness and chemical composition. Another problem is the influence of the interface roughness upon the reflectivity of multilayer.

Table 1.2 - Table of crystal monochromators used as spectral components in X-ray spectrometry.

Crystals	**Reflecting planes orientation**	**2d (in Å)**	**Applications**
Lithium fluoride (LiF)	200	4.027	From K to heavy elements
	220	2.848	Heavy elements
	420	1.801	Heavy elements
Quartz (SiO_2)	$10\bar{1}1$	6.684	As Ge (111)
	$10\bar{1}0$	8.514	As PET
Indium Antimonide (InSb)	111	7.480	Quantitative analysis of silicon
Silicon (Si)	111	6.271	Extinction of even order spectral lines
	220	3.840	
Germanium (Ge)	111	6.532	
	220	4.000	
Pentaerythritol PET ($C(CH_2OH)_4$)	002	8.740	-

Ammonium Dihydrogen Phosphate ADP, ($NH_4H_2PO_4$)		101	10.648	Mg
Beryl ($3BeO, Al_2O_3\ 6SiO_2$)		1010	15.950	Na and following elements
Acid Phthalates	Thallium TIAP ($CO_2HC_6H_4CO_2TI$)	001	25.900	F to Al
	Rubidium RbAP ($CO_2HC_6H_4CO_2Rb$)	001	26.120	Na, Al up to F in emission probes
	Potassium KAP ($CO_2HC_6H_4CO_2K$)	001	26.640	
	Cesium CsAP ($CO_2HC_6H_4CO_2Cs$)	001	26.650	

Studies show that sometimes in early stages of film formation, the thin layers form isolated islands and such non-continuous layers giving rise to a significant interlayer roughness and a distortion of the interference pattern in the multilayer structure. Therefore, a successful practical realization of high reflection from the multilayer requires careful investigation of film formation processes and interlayer structures to compose an optimal design of the mirror. Thus, it is a prerequisite to describe precisely the interlayers and have complete information about the interactions at the surface of the stack, in-between each layer and at the bottom layer and the substrate.

First part of this thesis is dedicated to the characterization of of Mg/Sc systems with the introduction of Cr and ZrC layers as capping and barrier layer. The capping layer prevents the

oxidation of the structure, while the barrier layer when at interfaces of Mg-on-Sc and Sc-on-Mg should prevent the intermixing of the two layers. The study is based on the analysis of thin film, bilayer, trilayer, quadrilayer and multilayer systems for the Mg/Sc systems with Cr and ZrC. The idea behind the individual analysis of different layer systems is to characterize and gather information from each interface. The result is then introduced into the design and fabrication of the multilayer structure.

Second part of the thesis focuses on the study of Fe/Si multilayer using X-ray emission spectroscopy (XES). The emission spectra allow us to study the interactions between elements in the buried layers from the analysis of their valence states. The emission band obtained as a result of the valence to core transition, has a distinct shape and width, reflecting the chemical state of the emitting element. Hence, XES was shown to provide sensitive information about the physical chemical environment of the emitting elements in multilayer. Until now XES has been applied in soft x-ray region (photon energy ≤ 2 keV) to study the buried layers and interfaces. In this thesis we extended the existing methodology to the hard x-ray range and used it to evaluate the sensitivity of the technique to study buried interfaces. The chapter also explores the possibility of formation of X-ray standing wave (XSW) inside the multilayer stack, in order to investigate the depth dependent chemical sensitivity of the combined XSW-XRF.

Chapter 2: Experimental Techniques

2.1 Synchrotron radiation

Synchrotron light sources are one of the most powerful tools for investigating the properties of matter in many different fields like molecular and atomic physics, biology, medical applications, nanotechnology, catalysis and cultural heritage. Electrons traveling at the speed of light, when changing their direction under the effect of magnetic fields (perpendicular to the direction of their motion), emit light, with peculiar characteristics, known as synchrotron radiation. A pictorial representation of the synchrotron facility is shown in figure 2.1. At first, electrons generated from an electron gun are accelerated to the speed of light by a linear accelerator (LINAC) and reach a kinetic energy of the magnitude of 100 MeV. The electrons are then transferred into the booster ring, a circular accelerator, where the energy of electrons increases from 100 MeV to several GeV. They then enter the outer circular storage ring and circulate periodically at a constant energy. Modern synchrotrons work in a so-called "top-up" mode, where the electrons are injected into the storage ring in small quantities but frequently to keep the current constant in the storage ring. The trajectory of the electrons inside the storage ring is directed and maintained by an array of bending magnets and insertion devices (wigglers and undulators). The magnets are placed alternatively in a series of arched sections separated by straight sections. Thus, when electrons pass through the ring they are deflected by the magnetic field created by the magnets resulting in the emission of electromagnetic radiation at each turn. A radio frequency cavity supplies extra energy to the electrons as they tend to lose their energy by emitting the radiations. The electromagnetic radiation produced by the synchrotron is emitted in a narrow cone in the forward direction, at a tangent to the electron's orbit and due to this, the different beamline stations are placed tangentially with respect to the ring. The synchrotron radiation is optimized at each beamline depending upon the functionality and purpose of the beamline setup. The different beamlines and their experimental setups used for the characterization of samples in this thesis are discussed in detail in the following sections [38].

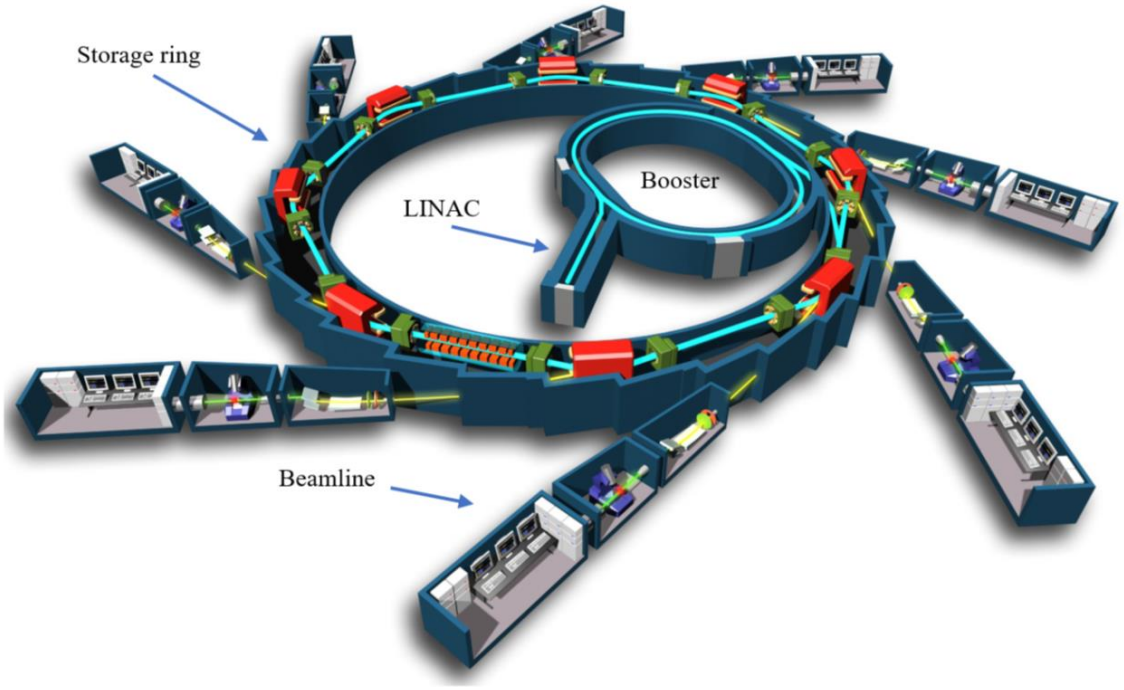

Figure 2.1 - Main parts of a synchrotron facility [39].

2.2 X-ray reflectivity in the hard X-ray range (8048 eV)

X-ray reflectometry (XRR) is a non-destructive and non-contact technique to study thin film and multilayer samples. The reflectivity measurement can be done by using a table top X-ray diffractometer configured to perform X-ray diffraction and reflectometry in grazing incidence. A schematic of a goniometer is shown in figure 2.2 with a Cu Kα radiation source with energy 8048 eV, a monochromator, slit (S1) that collimates the incident beam upon the sample surface, the sample holder and slits (S2, S3) to remove the aberrations before the reflected beam reaches the detector. When a monochromatic incident beam hits the sample surface at a grazing angle θ, the reflected intensity is then recorded by the photon detector at varying grazing incidence angles. Specular condition must be maintained during the experiment, that is the angle of incident radiation of the sample surface must be equal to the reflection angle. The measurement is done in θ-2θ mode, in which the position of the source is kept fixed while rotating simultaneously the sample at an angle θ and the detector at an angle of 2θ.

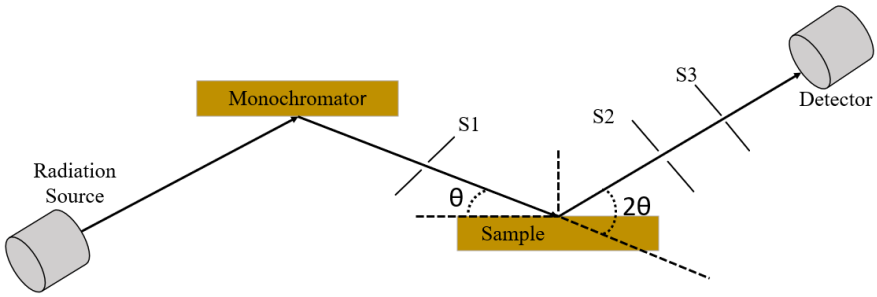

Figure 2.2 - Schematic of the X-ray reflectometer arrangement for hard X-ray grazing incidence X-ray reflectivity.

The reflectivity measurements done using a table top diffractometer were done at two places: one using a *Rigaku diffractometer* at INSP, Sorbonne Université and another using Bruker D-8 reflectometer in RRCAT, India. The details of the samples studied using two systems will be explained in the following chapters 3 and 4.

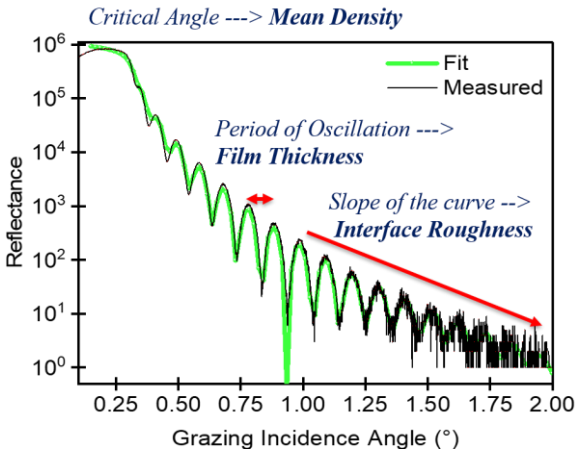

Figure 2.3 - Information provided by the reflectivity curve.

The measured reflectivity curve can provide information on the thickness, density, roughness of each layer and interlayer in a thin film and multilayer system. Shown in figure 2.3 is the measured and fitted reflectivity curve for a Cr thin film on a Si substrate, in which the oscillations observed are a result of the constructive interference of the reflected X-rays. These oscillations are known as the Kiessig fringes. The oscillations are representative of the film thickness, and the thicker the film, the shorter the period of oscillations. The critical angle for

total reflection provides information on the total density of the structure, with the slope of the curve being the representative of the roughness. The fitting of the reflectivity curves measured in this thesis is done by using IMD, a software that utilizes a nonlinear, least-squares curve fitting based on the χ^2 optimization to determine the structural and optical parameters for a thin film or a multilayer system [7].

2.3 X-ray reflectivity in the soft X-ray range (100-1500 eV)

The soft X-ray reflectivity (SXR) beamline at INDUS synchrotron caters to surfaces, near-surface and interface analysis of thin films and multilayers to study their structural and optical behaviour. It covers two energy ranges: (1) BL-04 operating in the range of 10-300 eV on Indus-1; (2) BL-03 operating in 10-1500eV on Indus-2 synchrotron radiation source. In this thesis, we have used Indus-2 synchrotron source (10-1500 eV) for study of our samples. Indus-2 is a 2.5 GeV electron storage ring installed on a bending magnet is equipped with a variable line spacing plane grating monochromator (VLS-PGM) with Hettrick type optics.

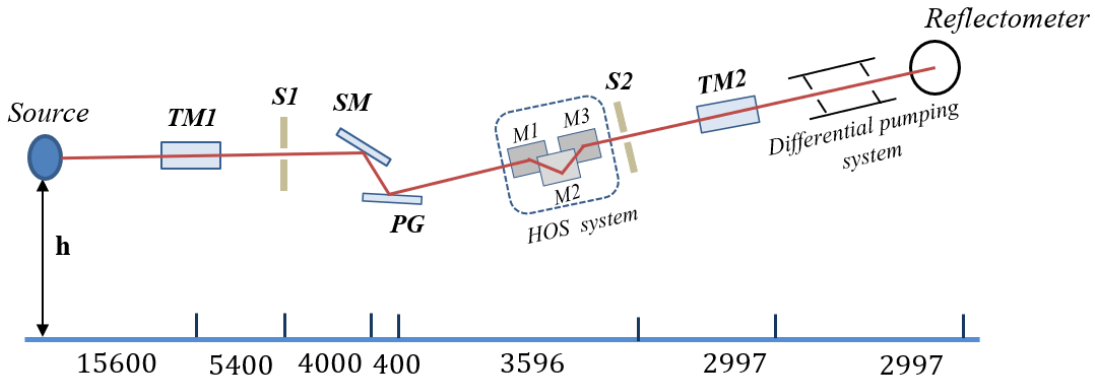

Figure 2.4 - Optical layout of the soft X-ray reflectivity beamline at Indus2 source. The abbreviations given in the figure are: TM1, TM2-Toroidal mirrors; SM-Spherical mirror; PG-plane gratings and M1, M2, M3-plane mirrors comprising the higher order suppressor system [39].

Shown in figure 2.4, is the optical layout of the reflectivity beamline mainly comprising of a pre-focusing toroidal mirror (TM1), a spherical mirror (SM), three interchangeable gratings

and finally a post-focusing toroidal mirror (TM2). TM1, which is horizontally deflecting, accepts 2 mrad (H) and 3 mrad (V) of the emitted bending magnet radiation and focuses light vertically on to the entrance slit S1, and horizontally on to the exit slit S2. The vertically deflecting spherical mirror then forms a convergent beam on the plane grating. The plane grating diffracts the white light and focuses the desired wavelength onto the slit S2. A set of three interchangeable gratings of line densities 1200, 400 and 150 lines/mm are used to efficiently cover the whole energy region of 100-1500eV. The whole beamline operates in ultra-high vacuum, $5x10^{-9}$ mbar and provides moderate spectral resolution of, $E/\Delta E \approx 1000\text{-}6000$ and high photon flux of $\sim 10^{9}$ - 10^{11} ph/sec. The beamline covers the K edges of light elements like C, N, and O and the L and M edges of transition elements [39].

The experimental section with the reflectometer chamber consists of a two-axes goniometer and a linear translation stage. The linear translation stage allows the sample movement in x-y-z direction for alignment process and to perform scans in θ-2θ configuration; The goniometer is set in vertical reflection geometry so that s-polarization geometry of the synchrotron light is chosen. The experimental section of the high vacuum reflectometer chamber is separated from the ultra-high vacuum section of the beamline via a differential pumping system. The reflected beam is detected using a silicon photodiode detector (International Radiation Detector Inc, USA) which have 100% internal quantum efficiency. The detector signal is measured in terms of electric current using a Keithley electrometer (6514) [40].

In the soft X-ray region, the refractive index is given in the complex form, $n=1-\delta+i\beta$, where δ and β are the dispersion and absorption coefficients respectively. In most cases, for X-rays the real part of the refractive index is slightly less than one and its decrement to unity δ is positive. But in the soft X-ray range, the value of δ for some elements is negative around their absorption edge. For example, the δ value of Sc is negative around its L3-absorption edge (400 eV) [41]. This sign reversal can be understood by the response of the bound and free electrons contribution to the scattered field. The bound electron contributes in-phase with the scattered field whereas the free electrons contribute out of phase with respect to the scattered

field. When the energy of the incident beam is tuned to the absorption edge of the element under study, the electrons are not able to move out of the local environment of the atom and as result contribute to the scattered field with in-phase polarization. However, when the energy of the incident beam is sufficiently higher to bring the electrons out of the local environment of atom, it then contributes as out of phase polarization. Hence, when the in-phase component surpasses the out of phase one, the real part of the refractive index undergoes sign reversal [42,43].

The scattered intensity measured of the reflected X-ray is due to the variation in in electron density near the interfaces. In conventional XRR, the optical contrast is not sufficient for low atomic number elements to identify the small compositional gradients at the interfaces. However, when the incident beam energy is tuned to the energy of absorption edge of the element to be investigated, the X-ray reflectivity shows resonant behaviour. Near the absorption edge, the scattered intensity undergoes strong modulation due to significant change in refractive index as a result of change in chemical environment of the element. This change in the refractive index also results in the variation of atomic scattering factors. Hence, with resonant reflectivity one can achieve sensitivity to a specific element with high optical contrast by tuning the energy of the X-rays to the absorption edge of the element being investigated.

2.4 X-ray emission spectroscopy

X-ray emission spectroscopy (XES) is an important tool for investigation of materials and is employed in almost every thinkable field of technology ranging from materials science, to environmental research, architecture, art, forensics and astronomy. XES serves as direct fingerprints for elemental analysis, as it provides both quantitative and qualitative information of constituting elements inside a material. X-ray fluorescence, (XES in the case where excitation is performed by X-rays) is a so-called photon-in, photon-out spectroscopy in which an incident photon of energy ($h\nu$), ejects an electron from the inner shell of the atom thereby creating a hole. Following this, the atom goes into an ionized state, intrinsically unstable and decays instantaneously via the transition of an electron from a higher energy shell to fill the vacancy in the core shell along with the radiative emission of an X-ray. The other is possibility is the non-radiative emission, with ejection of an electron (Auger electron). The emitted X-rays

are the characteristic X-rays with energy equivalent to the difference in energy between the core and high energy electronic shells involved in the transition. Figure 2.5 shows the scheme of electronic transitions The electronic transitions between empty and filled energy states that satisfy the following quantum selection rules are the most intense.

$$\Delta l = \pm 1;\ \Delta j = 0,1\ (j = \pm 1/2);\ \Delta n \neq 0$$

where l and j are the orbital quantum number and total angular momentum quantum number respectively.

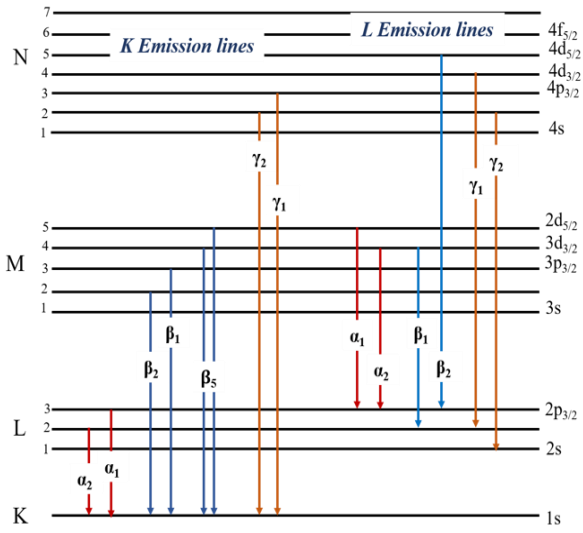

Figure 2.5 - Scheme of K and L emission lines.

X-ray emission spectra reflect partial occupied density of electronic states. The position of peak and its chemical shift, the shape of spectrum as well as any satellites are important characteristics for analysing chemical states of elements present at buried interfaces within a sample. An X-ray spectrometer commonly equipped with diffraction grating, crystal analyser or multilayer mirror is employed to record and analyse the emitted fluorescent X-rays. The diffraction properties of the analyser crystal and the spectrometer geometry govern the selection and recording of the photon energies. After the irradiation of X-rays onto the sample, all types of X-rays: incident, scattered and fluorescent X-rays are emitted essentially into all directions.

Therefore, the required instrumental set up must possess a large angular acceptance with good energy resolution [44]. The analyser X-ray optics can be categorized into two types:

1. *Scanning monochromator* type cylindrically or spherically curved crystal based on Rowland geometry, shown in figure 2.6(a). The spectrum is recorded by varying the incident beam energy across the spectral range of interest. This is done by changing simultaneously the analyser angle and detector position.
2. *Polychromator* type cylindrically curved crystal based on Von Hamos geometry, shown in figure 2.6(b) that disperse the emitted X-rays with different energies onto a position sensitive detector.

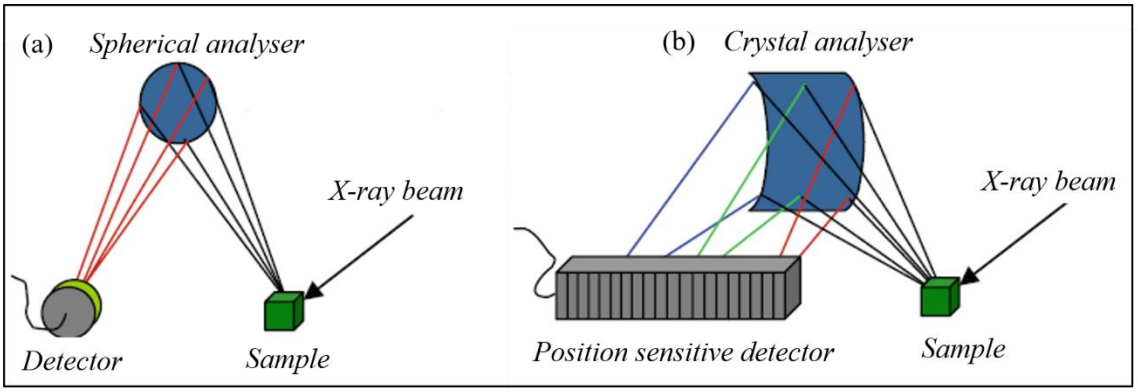

Figure 2.6 - Schematic representation of XES spectrometers based on different crystal analyser setups, (a) Rowland based geometry with monochromator crystal (b)setup based on Von Hamos geometry with polychromator crystal analyser [44].

In this thesis we studied Fe/Si multilayer using XRF on GALAXIES beamline with an instrument based on Rowland Circle geometry at synchrotron SOLIEL.

2.5 GALAXIES Beamline

The GALAXIES beamline at the SOLEIL synchrotron is dedicated to photoelectron spectroscopy (HAXPES) and inelastic X-ray scattering (IXS) under both in non-resonant (NR-IXS) and resonant (RIXS) conditions in the hard X-ray range (2.3–12 keV). These two techniques provide detailed information about the electronic properties of materials, specific to the chemical element and selected orbitals with bulk sensitivity. The resonant and non-resonant

IXS processes can utilized different techniques such as X-ray emission spectroscopy (XES), high-energy-resolved fluorescence detection (HERFD) and X-ray Raman spectroscopy (XRS). Hence the study for each of these require different experimental conditions and configuration in terms of resolution, geometry and apparatus. In this thesis we have used the resonant inelastic X-ray scattering setup for the of the GALAXIES [45]. RIXS end station installed on the GALAXIES beamline, allows to perform XES experiments in the hard X-ray range.

Figure 2.7 shows the schematic of RIXS spectrometer, depicting the arrangement of the detector assembly with the position of single and multi-crystal analysers and the sample stage. The spectrometer is mounted on five-axis motorised base with stepper motors that allows the user to align the spectrometer with respect to the incident beam position. Placed at the base are the anti-skid and anti-vibrational pads that ensure excellent vibration dampening. A compact horizontal rotation stage and a small manual goniometer is attached to the sample stage for sample alignment.

The setup is based on a six axis Newport diffractometer with two rotating arms: a long vertical arm and a short horizontal arm for energy or momentum analysis of scattered photons. The horizontal arm is equipped with four spherically bent crystal analysers having radii of curvature of 0.5 or 1 m. The crystal analysers collect all the scattered as well as fluorescence X-rays emitted by sample on its irradiation by the incident photon beam and focused them onto the detector. The scan of the emitted energy is realised by changing the height of the analysers while adjusting the analyser-sample and detector-sample distances thereby maintaining a Rowland circle geometry. A helium filled bag is placed between the sample, the analysers and the detector to reduce air absorption [46].

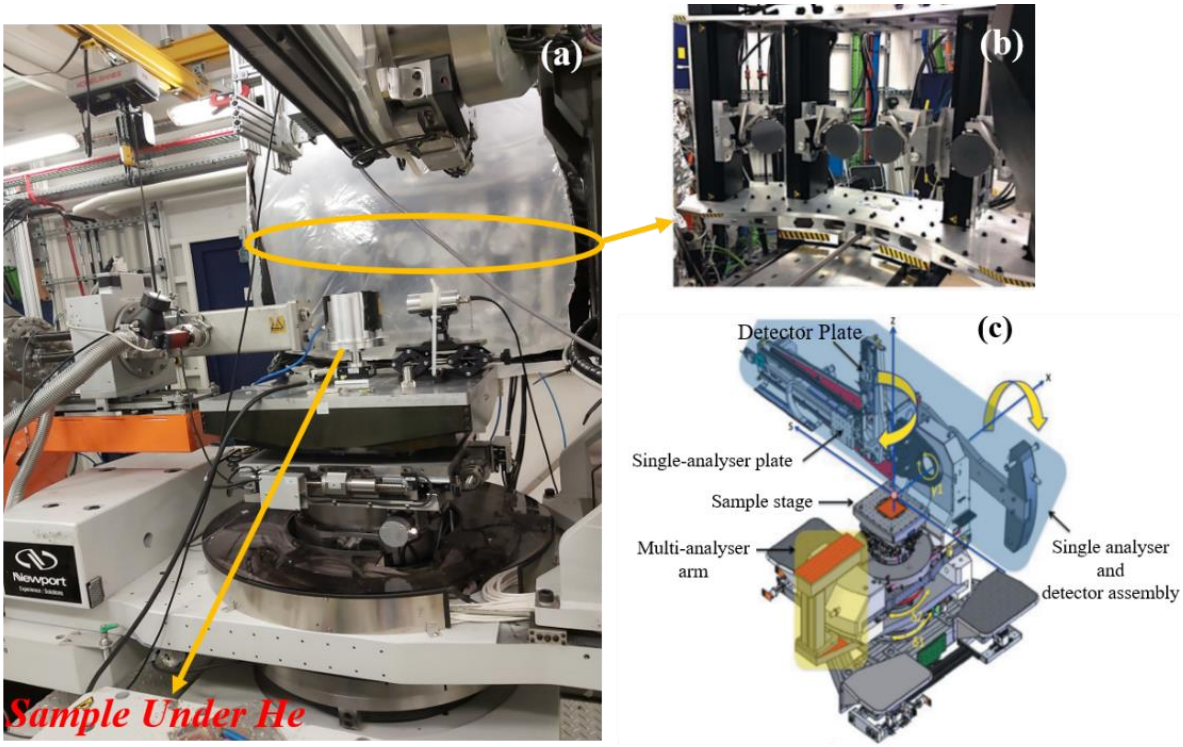

Figure 2.7 - (a) Complete RIXS set up at GALAXIES beamline (b)multi-analyser crystal set arranged in 4x1 configuration (c) RIXS spectrometer marked with different components such as analysers, detector plate and sample stage [45].

2.6 Combined X-ray reflectivity and X-ray fluorescence technique

Grazing incidence X-ray fluorescence (GIXRF) is based on the measurement of fluorescent X-rays emitted by the elements in a material and their detection and analysis as a function of glancing angle of the incident radiation. The emitted fluorescent signal is element specific and the angle dependent curve gives depth dependent information about the elemental composition, concentration and thickness. X-ray fluorescence signal.

X-ray reflectivity (XRR) on the other hand is also a non-destructive interface-sensitive technique used to determine thickness, in-depth electronic density and roughness of thin films and multilayers. Similarly, here the intensity of specularly reflected X-rays is measured as function of varying grazing incidence angle [47]. Hence, that both XRR and GIXRF are based on a similar measurement of recording the intensity (reflected or fluorescent beam) as a function

of grazing incidence angle. These techniques follow the same principle of data analysis as XRR is based on the Parratt's formulism [5] that uses recursive method for the calculation of reflected part of the beam, as explained in chapter 1 and as De Boer in 1991 [48], formulated a method for the calculation of fluorescence emitted from sample based on Parratt's recursive method. Therefore, the two techniques can be very well combined to have better characterization of sample in terms of thickness, roughness, mass density and in-depth elemental profile and to reduce the uncertainties presented by each technique individually. The combination of the two involves simultaneous measurement of the intensity of the specular reflectivity and emitted fluorescence and their consequent data analysis using combined fitting software. The combined XRR and GIXRF analysis on our samples was done at METROLOGIE beamline at synchrotron SOLEIL, using a specialised instrument CASTOR.

2.7 METROLOGIE Beamline

The beamline is composed of two branches: a **soft X-ray branch (30 eV – 1800 eV)** and a **hard X-ray branch (100 eV – 40 keV)** and is equipped with CASTOR instrument dedicated to the metrological characterization of thin films and multilayers. The instrument **CASTOR** (*Chambre d'Analyse Spectrométrique en Transmission ou en Réflexion*) enables the combined analysis of X-ray reflectivity and X-ray fluorescence using a seven-axis goniometer with p-polarization [49]. A schematic representation of the instrument is shown in figure 2.8. The samples are placed vertically on two perpendicular translation stages (namely Tz and Ts), which are further mounted on a rotation stage (Rx). This three-axis platform is attached to a horizontal translation stage (Tx), which is further placed above the upper rotation stage (Rθ). The detection arm is on a second rotation stage (Rθ2) placed at the bottom of the stages and is equipped with four photodiodes. The photodiodes are used to record the X-ray reflectivity signal in a θ-2θ configuration, while the energy dispersive detector facilitates the fluorescence related measurements. The fourth translation (Tz2) allows the detector to be selected. R and R2 are the most critical axes for the experiments and are encoded for better accuracy [50].

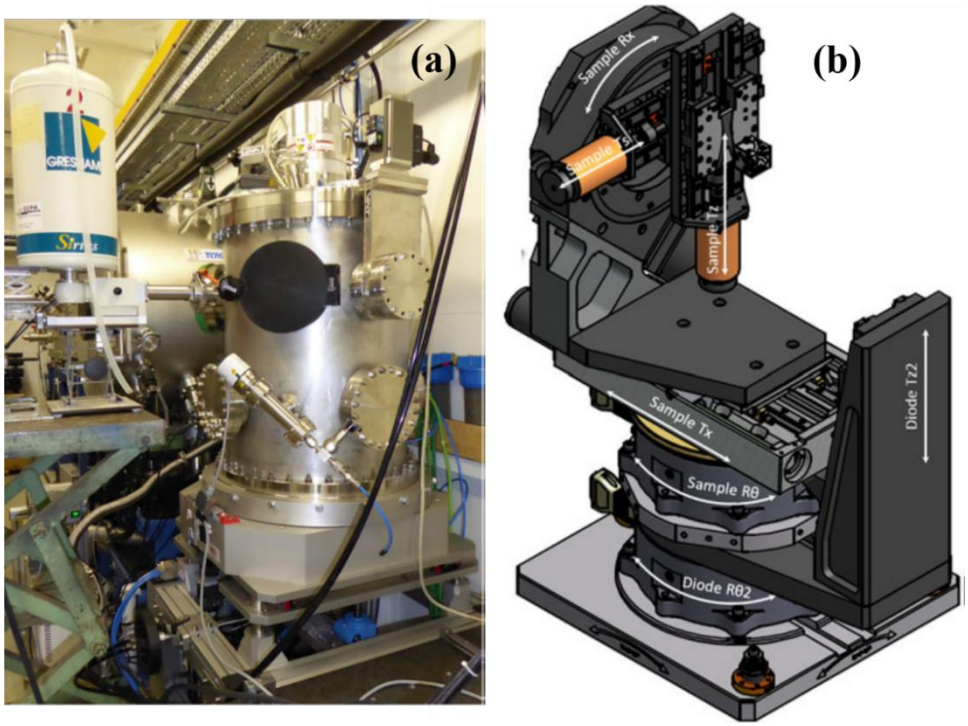

Figure 2.8 - (a) External view of the CASTOR setup installed at Metrologie beamline (b) Schematic representation of seven-axis goniometer.

Prior to any measurement the CASTOR setup is aligned by placing a pinhole, of diameter 200 μm, in line with the path of the beam. This is realised by scanning the translation stage, T_X, perpendicular to the beam for $\theta = 0°$ to center the position of the beam within the pinhole. The scan is repeated for $\theta = 180°$ and the average of the two T_X scanned positions gives the correct position and the whole chamber is moved accordingly. The second step is the alignment of the sample. The sample holder contains four slots for the placement of different samples. A reference sample, which in our case was a Ni (9 nm) thin film was placed on one slot and other samples were kept on the remaining three slots. For alignment, the reference sample is positioned in front of the detector using T_Z. Then Rθ1 is adjusted and the translation stage TX1 is varied to find the maximum of the detected signal. The alignment is done by repeatedly scanning the translation stage Tx1 and adjusting Rθ1, until no changes are found in the expected values with respect to the precision of the translation or rotation steps. In the end,

the sample is set at the position of maximum intensity corresponding to the values of Tx1 and Rθ1.

The combined XRR and XRF measured signal is recorded and analysed by a software linked to the CASTOR setup. The footprint of the incident beam on the sample surface is defined by the slit. Since the samples are placed vertically, a vertical slit with a larger height is used to limit the horizontal divergence of the beam and to increase the flux. Several slits of 100 nm width and vertical aperture of 1, 3 or 5 nm can be used.

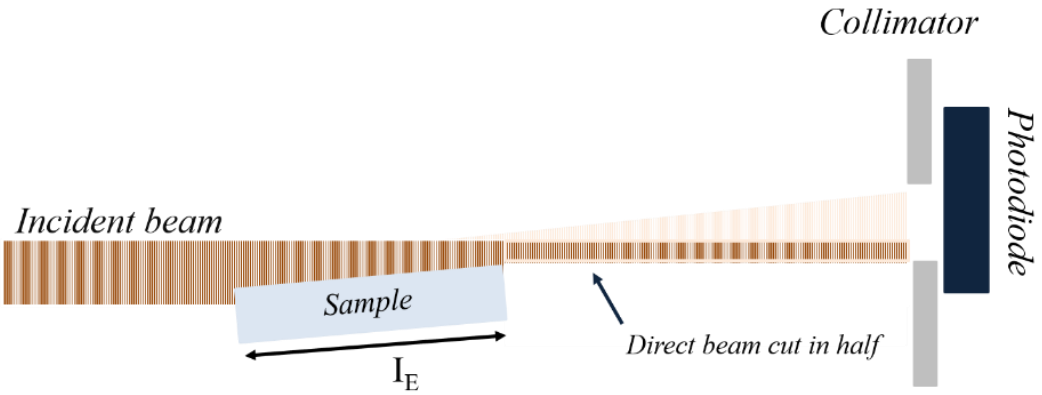

Figure 2.9 - Geometry for the XRR at shallow angles [50].

In case of X-ray fluorescence, geometrical factors play an important role in analysis of the fluorescence curves. Shown in figure 2.10 is a schematic of incident beam impinging on a surface and representation of a collimator of thickness (e) and diameter (c) placed in front of the SDD and at a distance d1 from the sample. The solid angle depends on the distance of the collimator from both the sample and the detector (d2), the collimator dimensions and incoming beam characteristics (its shape and dimensions). Firstly, the solid angle is calculated as function of radial distance from the sample, as every irradiated point on the sample does not contribute equally to the emitted signal.

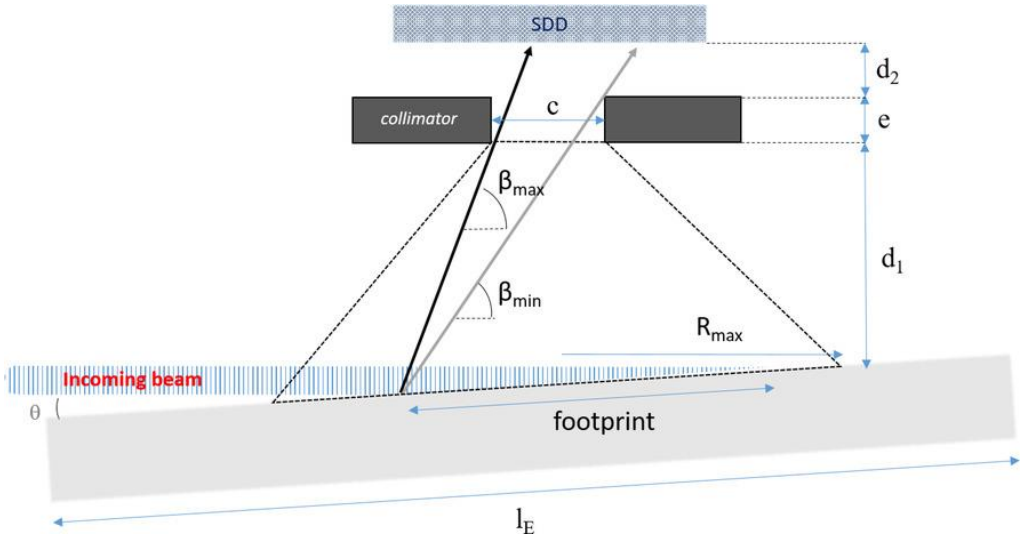

Figure 2.10 - A schematic representation of the field of view of the SDD detector [50].

$$\Omega_r(r) = \iint^{S(r)} \frac{\sin(\beta)}{((d_1{+}e + d_2)^2 + (r + x)^2 + y^2)} dxdy$$

The angle β is given by:

$$\beta = arctan\left(\frac{d_1 + e + d_2}{\sqrt{(r + x)^2 + y^2}}\right)$$

The integral limits are expressed as a surface S(r) given as, $S(r) = A_{SDD} \times A_{c1} \times A_{c2}$, where A_{SDD} is the active area of SDD detector, and Ac1 and Ac2 are the projected areas on the detector from the front and back side of the pinhole respectively. the solid angle for each incident angle is given by

$$\Omega(\theta) = \frac{1}{A_s} \iint \Omega_r(r)\, dxdy$$

where A_S is the footprint, which is the area shared by the incident beam on the sample surface, the sample length and the field of view of the SDD delimited by the maximal radius R_{max} [49].

2.8 Secondary ion mass spectroscopy

The previous sections discuss the material analysis method using non-destructive X-ray reflectivity and X-ray fluorescence techniques with surface and depth characterization. SIMS on the other hand is a destructive depth profiling technique that is used to analyse the isotopic, elemental, chemical and molecular state of the constituting elements inside the sample. In this technique, an energetic primary ion beam (of Bi^+, Cs^+, Ar^+, O_2^+, or C_{60}) is used to sputter the sample surface. As incident ion collides with the sample surface, its energy is transferred to the target atoms and is further transmitted successively from one atom to another resulting in a collision cascade. The aftermath of the collision results in the implantation of the impinging target atom, ejection of neutral atoms, ionisation of atom giving rise to the emission of electrons, X-rays, ions, and molecular ions. Hence, the whole process damages and modifies the target material. The ejected ions are sorted and analysed as a function of mass/charge ratio using a mass spectrometer [51]. SIMS instruments differ by the type of mass analyser used: magnetic, quadrupole or time-of-flight. In this thesis we have used time-of-flight based SIMS to study our samples. Schematic of TOF-SIMS apparatus is shown in figure 2.11. In time-of-flight secondary ion mass spectroscopy (ToF-SIMS), the secondary ions are accelerated to a given potential. After this they enter a free flight chamber under ultra-high vacuum in which no external is applied on them and are made to fly up to the time-of-flight detector. The ions are then separated based on the time it takes for them to reach the detector, which is directly dependent on the mass of ion by:

$$t_{ToF} = L * \sqrt{\frac{m}{2q(E_0 + U)}}$$

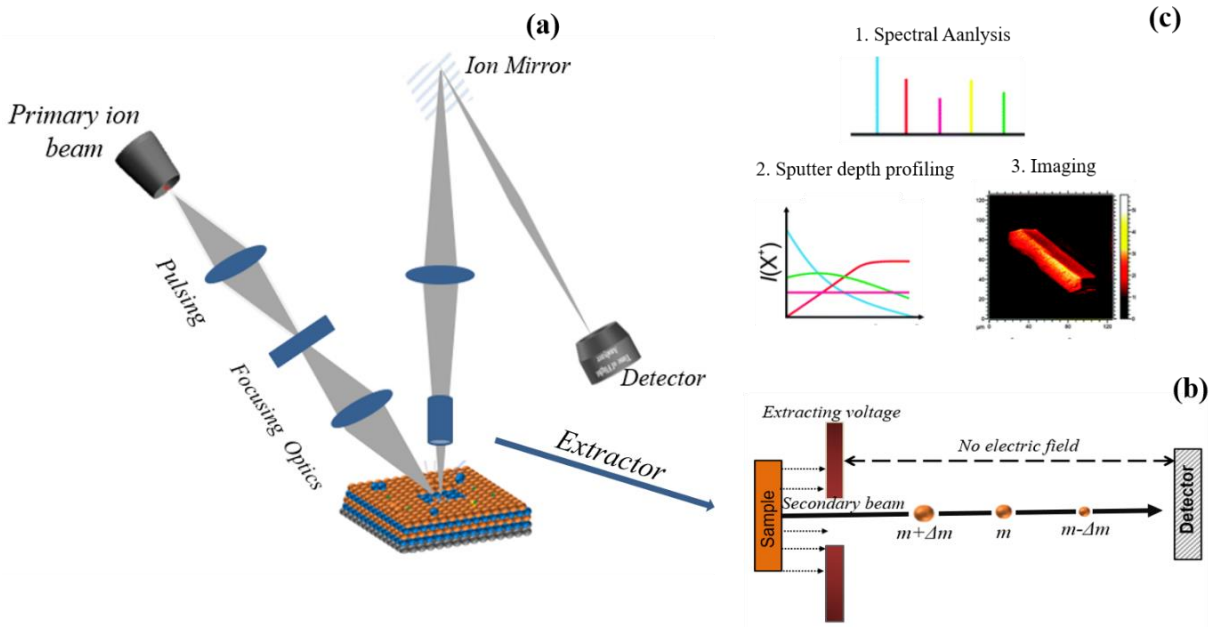

Figure 2.11 - (a) Schematic of a TOF-SIMS apparatus showing the sputter and analysis of ions using a time-of-flight analyser in (b). (c) Types of analysis possible using TOF-SIMS.

where t_{ToF} is the time taken by the ions to reach the detector, L is the length of the chamber, U the applied potential, E_0 is the energy of the ion and m being the mass of the ion. The lighter the ions i.e., with a low mass/charge ratio, the sooner they arrive as compared to the heavy ions [52]. In ToF-SIMS, the primary ion beam can be rastered over a small area of interest to determine the lateral distribution of elements and molecules on the sample surface known as the mass image. We performed ToF-SIMS measurements on Mg/Sc and Sc/Mg bilayers, that are discussed in detailed in chapter 3. The analysis was done using Bi^+ ion gun operating at 30 keV and ~2.5-3.0 pA. The depth profiling was made with a O_2^+ ion gun operating at 500 eV, ~100 nA over an analysis of 100 µm× 100 µm.

Chapter 3: Study of Mg/Sc systems

3.1 Introduction

The functionality and shortcomings of different spectral components for operation in the N K emission range have been discussed in details in chapter 1. Figure 3.1 shows the simulation of a perfect (without roughness or diffusion) periodic Sc/Mg multilayer having 25 bilayers, with a period of 6 nm. It presents a 51% reflectance at the N K absorption edge of 395 eV. However, a case of perfect interfaces does not exist. Indeed interdiffusion at interfaces, formation of rough surfaces and even in some cases presence of buried layers hinder the quality and overall optical performance of any multilayer system. Thus, it is a prerequisite to describe precisely the interlayers and have information about the interactions at the surface of the stack, in-between each layer and at the bottom layer and the substrate.

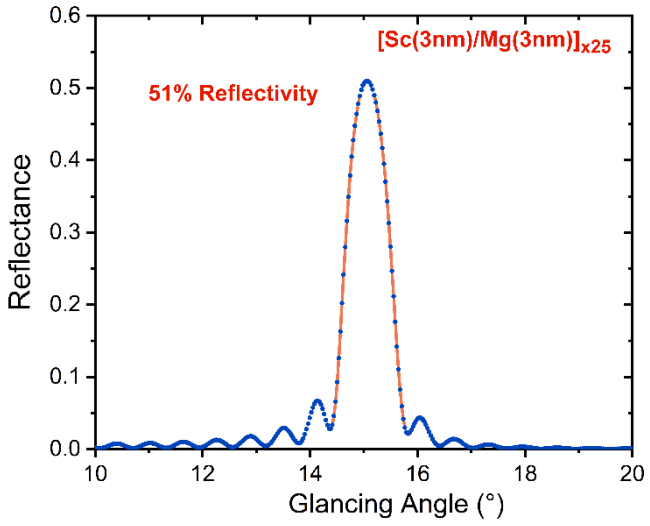

Figure 3.1 - Reflectance calculated for [Sc(3nm)/Mg(3nm)]x25 multilayer at the incident photon of energy of N K edge (395 eV).

This chapter highlights the study of interfaces of Mg/Sc systems. Various combinations of bilayer, trilayer, and quadrilayer systems of Mg/Sc with ZrC and Cr as a capping and barrier layer, were fabricated and characterized. The capping layer prevents the stack from oxidation

while the presence of a barrier layer between the two layers hinders the mixing between them. The choice of ZrC and Cr as diffusion barriers was made owing to their positive mixing enthalpy with Mg and Sc. A positive mixing enthalpy suggests that the combination of Mg/ZrC, Sc/ZrC, Mg/Cr and Sc/Cr layers will not undergo mixing. Table 3.1 below lists the different sets of ZrC and Cr based Mg/Sc systems studied, with the designated abbreviations used for discussion in this chapter.

Table 3.1 - Structural design of Mg/Sc systems with ZrC and Cr thin films.

S.No.	Structure	Abbreviations
	Bilayer (with ZrC)	
1	[Mg(20nm)/Sc(20nm)]/Si substrate	***Mg/Sc***
2	[Sc(20nm)/Mg(20nm)]/ZrC(1.5nm)/Si substrate	***Sc/Mg***
	Quadrilayer (with ZrC)	
3	[Sc(19nm)/ZrC(2nm)/Mg(11nm)/ZrC(2nm)]/Si substrate	***Sc/ZrC/Mg/ZrC***
4	[ZrC(2nm)/Sc(20nm)/ ZrC(2nm)Mg(10nm)]/Si substrate	***ZrC/Sc/ZrC/Mg***
5	[ZrC(2nm)/Mg(10nm)/ZrC(2nm)/Sc(20nm)]/Si substrate	***ZrC/Mg/ZrC/Sc***
	Bilayer (with Cr)	
6	[Cr(20nm)/Mg(20nm)]/Si substrate	***Cr/Mg***
7	[Cr(20nm)/Sc (20nm)]/Si substrate	***Cr/Sc***
8	Cr(2nm) [Mg(20nm)/Sc(20nm)]/Si substrate	***Cr/(Mg/Sc)***
	Trilayer (with Cr)	
9	Cr(4nm) [Mg(16nm)/Sc(21nm)]/Si substrate	***Cr/Mg/Sc***

The samples were characterized using a combination of techniques of X-ray reflectivity, time of flight secondary ion mass spectroscopy and combined X-ray reflectivity and grazing incidence X-ray fluorescence (XRR-GIXRF). The discussion of ZrC based Mg/Sc systems is presented first, that are characterized using X-ray reflectivity technique in both hard and soft X-ray regions. ToF-SIMS analysis of the samples gives the distribution of layers of inside the stack and provides information of the possible compounds formed as a result of intermixing between the layers. In the end, combined XRR-GIXRF study of the Cr based samples discusses the ability of the technique to provide element sensitive structural information of the stack.

3.2 Study of ZrC based samples

3.2.1 Sample Preparation

The samples were fabricated using Ion beam sputtering technique. Commercially available sputtering targets of Mg, Sc and ZrC with 99.5% purity were used. Deposition chamber was evacuated to 10^{-7} mbar before sputtering. The targets were sputtered by 1 keV Ar ions using Kauffman ion source with 3 sccm flow. Working pressure was maintained in ~10^{-3}mbar range during the deposition. The sputtering targets were pre-sputtered for ~10 min to remove surface contamination. Samples were then deposited at a typical deposition rate of 0.5-0.7 nm/min for all Mg, Sc and ZrC films.

3.2.2 Characterization

Grazing incidence hard X-ray reflectivity (GIXRR), a non-destructive tool, is used to probe the different bilayer, and quadrilayer structures to deduce structural parameters: thickness, roughness and density of layers and interlayers. Grazing incidence reflectivity measurements using hard X-rays were performed using a table top Bruker D-8 reflectometer equipped with a θ-2θ goniometer and a Cu Kα source (8048 eV). The reflectivity in the soft X-ray region was carried out at the soft X-ray reflectivity beamline at Indus-2 synchrotron source. The beamline operates in the energy region of 100-1500 eV with moderate resolving power ($E/\Delta E \approx$ 1000-6000) and high photon flux of 10^{9}-10^{11} photons/s [39]. The beamline operates under ultra-high vacuum (< 3x10^{-9}mbar). The reflectometer is kept in a high vacuum

experimental chamber equipped with a two-axis goniometer and a linear translation stage for sample movement. The reflected beam is detected using a Si photodiode connected to a Keithley electrometer.

SXR measurements were done by tuning the energy of the incident beam around the Sc L-absorption edge, and varying the incident photon energies from 370 to 420 eV around the absorption edge. The measured data was then fitted using IMD, a program for modelling optical properties of thin films and multilayers, based on Parratt recursive formalism to obtain the structural and optical parameters of the stack: thickness, roughness, density and real and imaginary parts of the optical index of the layers and interlayers [5,7]. It utilizes nonlinear least squares curve fitting technique based on χ^2 minimization method to fit the reflectivity curves.

To further highlight the morphology of interfaces for different systems, time-of-flight secondary ion mass spectroscopy (ToF-SIMS) measurements were performed. The analysis was done using Bi^+ ion gun operating at 30 keV and ~2.5-3.0 pA. The depth profiling was made with a O_2^+ ion guns operating at 500 eV, ~100 nA over an analysis of 100 μm× 100 μm and positive ions were recorded. Cs^+ ion gun was also used to record the negative ions for the samples. ToF-SIMS profiles are recorded by measuring the intensity of each incident ion of a given mass as a function of the sputtering time. It must be noted that the time scale is not relative thickness of each layer and that the sputtering yields of two elements is not related to the difference of concentration of these elements.

Since, fitting of the reflectivity data can result in various possible fitted structures when we take into account different thickness, composition and density of constituting layers and interlayers. We then first use, ToF-SIMS analysis to determine a priori information on the possible structure, by measuring the distribution of elements as a function of sputter time inside the stacks. Then, the possible structure obtained from the ToF-SIMS analysis is used to fit the measured GIXRR curves for all the samples.

3.2.3 Results and discussion

1. **[Mg(20nm)/Sc(20nm)] bilayer – Mg/Sc**

Figure 3.2 shows the ToF-SIMS profiles of Mg^+, Sc^+, Si^+ ions as well as C^+ ions obtained on the Mg/Sc bilayer. For sake of clarity, the regions corresponding to Mg and Sc layers and Si substrate are delimited by vertical lines. The progression of Mg and Sc profiles suggests that Mg is diffusing towards the Sc layer, resulting in an interlayer formation. The small increase, between the Sc layer and the substrate could be indicative of an interlayer. Even if there exists no direct relation between the sputtering time and the depth, it takes about four more time to sputter the Sc layer than the Mg one. Knowing that the ratio of the sputtering yields of Mg to Sc by oxygen ion of 1 keV is about 0.5 (it should be the same order of magnitude for 0.5 keV ions), we expect the Sc layer to be at least twice thicker than the layer containing Mg atoms. Carbon is only present at the surface owing to atmospheric contamination.

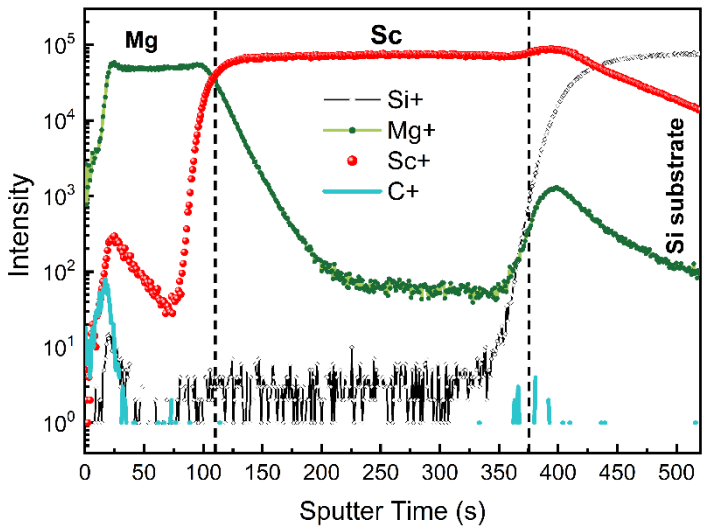

Figure 3.2 - ToF-SIMS profile for Mg/Sc bilayer obtained with O_2^+ion gun.

Now that we have an idea of possible structure of the Mg/Sc bilayer, this information is implemented to fit the measured GIXRR curve. Figure 3.3(a) shows measured as well as fitted GIXRR data of the Mg/Sc bilayer. The best fit was obtained using a four-layer model consisting of a top layer due to surface oxidation (MgO), an MgSc layer, the nominal Sc layer and an interlayer at the scandium and silicon substrate interface. Table 3.2 collects the structural parameters of the stack deduced from the fit. From these parameters, the δ-profile is plotted in Figure 3.3(b). The thickness of the layers containing Mg atoms (4.5 nm) is much lower than the

aimed thickness (20 nm), whereas the Sc thickness (17 nm) is a little lower than the aimed one (20 nm). This could come from a problem in the calibration of the Mg and Sc deposition rates or of a low sticking coefficient of magnesium atoms on scandium.

The formation of the interface layer on Mg-on-Sc interface can be understood by the value of the mixing enthalpy of Mg and Sc. It is found that the maximum values of enthalpy calculated from semi-empirical Miedena model [53] for Mg-Sc is -5 kJ/mol. This negative value means that the interface Mg-on-Sc is prone to interdiffusion and a mixed region is likely to be formed as a result of diffusion of Mg atoms into the Sc layer during the deposition. The Sc layer is mostly uniform with a density close to that of the bulk. An increase in the δ-profile is seen at the Sc-on-Si interface. The calculated delta value of the interlayer (16.76×10^{-6}), Table 3.2, suggests that the interlayer formed at the Sc-on-Si interface could either be an oxide of scandium, Sc_xO_y (10.50×10^{-6}) or a scandium silicide (ScSi 10.50×10^{-6}; Sc_3Si_5 10.69×10^{-6}). But since the fitted δ value of the interlayer is higher than those of Sc_xO_y, ScSi and Sc_3Si_5, we suggest that the interlayer is rather a mix of ScSi interlayer with the presence of O atoms resulting into a higher density [54,55]. The source of oxygen is the native oxide layer naturally formed of top of the silicon substrate.

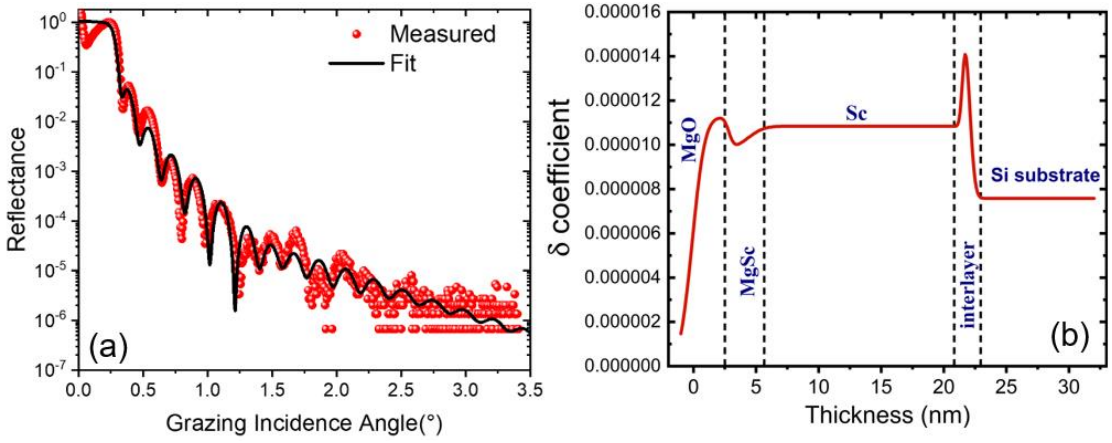

Figure 3.3 - For the Mg/Sc bilayer: (a) experimental and fitted GIXRR curves; (b) in-depth δ-profile deduced from the structure used to fit the GIXRR curve.

Table 3.2 - Structural and optical parameters of the Mg/Sc bilayer, where z and σ are the thickness and roughness of each layer respectively; δ and β are the dispersion and absorption coefficients. The thicknesses and roughness's are given ±0.1 nm.

Layer	**z (nm)**	**σ (nm)**	**δ (×10^{-6})**	**β (×10^{-7})**
MgO	2.93	0.80	11.24	1.23
MgSc	1.54	0.32	9.79	3.95
Sc	17.15	1.00	10.84	6.76
Interlayer	0.51	0.20	16.76	5.95
Si substrate	-	0.35	7.58	1.73

2. [Sc(20nm)/Mg(20nm)]/ZrC(1.5nm) bilayer – Sc/Mg

Figure 3.4, shows the ToF-SIMS profile of Mg^+, Sc^+, Zr^+, Si^+ ions as well as C^+ ions of Sc/Mg bilayer where the different layers are separated delimited by vertical dotted lines. As in Tthe existence of an interlayer at the Sc-on-Mg interface. Owing to the very small thickness of the ZrC layer, it is difficult to know if the shoulder observed on the Mg profile around 360s should mark could evidence the presence of an interlayer between Mg and ZrC layers or is due a transient sputtering regime. Carbon is only present at the surface owing to atmospheric contamination and is not enough intense to be observed from the ZrC layer.

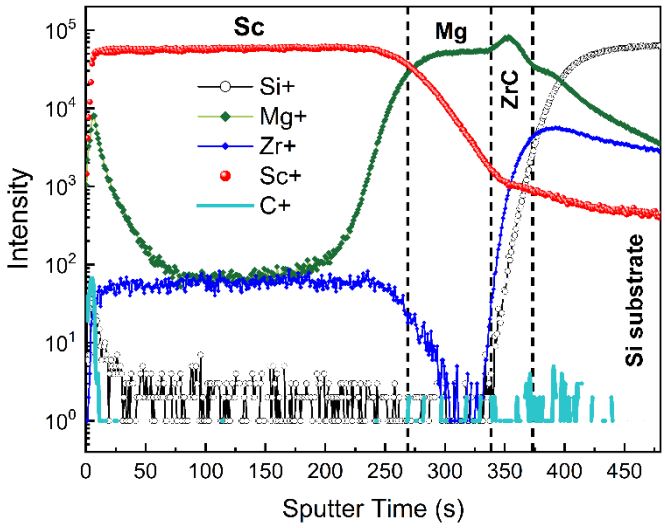

Figure 3.4 - ToF-SIMS profile of Sc/Mg bilayer obtained with O_2^+ion gun.

Similarly, here, the ToF-SIMS analysis result is applied to find a structure suitable to fit the Sc/Mg GIXRR curve. The fitted and measured curves are shown in Figure 3.5(a). The fitted structure is a six-layer model, that is to say in addition to the nominal layers of Sc, Mg and ZrC, a top layer due to surface oxidation (Sc_2O_3), an interfacial layer (MgSc) at the Sc-on-Mg interface and a native oxide layer (SiO_2) on the silicon substrate have to be introduced. Thickness and roughness of different layers along with their δ and β values for each layer as extracted from the GIXRR analysis are given in Table 3.3. The fitted optical constants for each of the nominal layers are close to their bulk densities. The delta δ-profile deduced from the chosen structure of the parameters of Table 3.3 is shown in Figure 3.5(b).

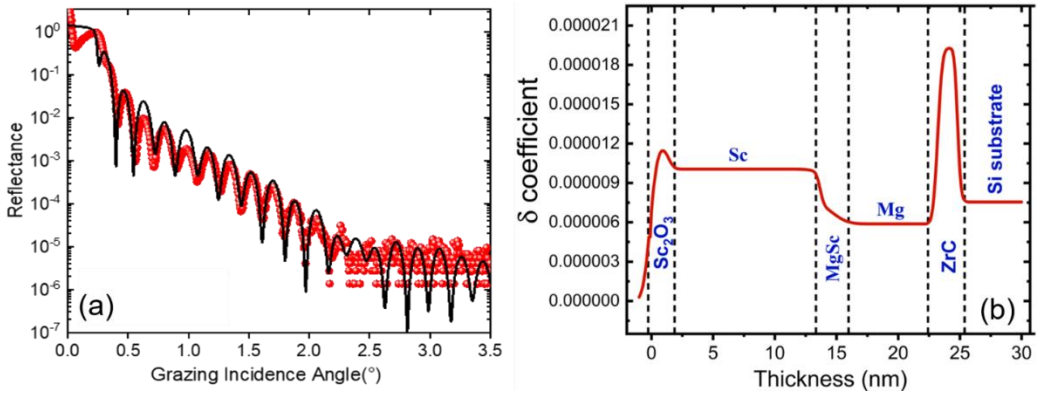

Figure 3.5 - For the Sc/Mg bilayer: (a)experimental and fitted GIXRR curves; (b) in-depth δ-profile deduced from the structure used to fit the GIXRR curve.

Table 3.3 - Structural and optical parameters of the Sc/Mg bilayer, where z is thickness of each layer, σ being the roughness of each layer δ and β are the dispersion and absorption coefficients. The thicknesses and roughness's are given ±0.1 nm.

Layer	**z (nm)**	**σ (nm)**	**δ ($\times 10^{-6}$)**	**β ($\times 10^{-7}$)**	**δ ($\times 10^{-6}$) (Bulk)**	**β ($\times 10^{-7}$) (Bulk)**
Sc_2O_3	1.47	0.46	11.81	5.85	11.99	5.95
Sc	12.3	0.36	10.05	7.52	9.10	6.85
MgSc	0.94	0.25	7.67	4.09	7.67	4.09
Mg	8.59	1.00	5.88	0.87	5.58	0.83
ZrC	1.6	0.30	19.29	9.64	19.16	9.57
SiO_2	0.24	0.20	8.71	1.13	7.13	0.92
Si subs.	-	0.25	7.58	1.73	7.58	1.73

As for the previous sample, the thickness of layers containing Mg atoms as well as the layers containing Sc atoms are smaller than the aimed designed ones. On the contrary the ZrC layer thickness is close to the aimed one. The large thickness of the Sc layer prevents the underneath Mg layer from oxidation. The thickness of the MgSc interlayer is limited to 0.9 nm in the Sc/Mg bilayer while it is 1.5 nm in the Mg/Sc bilayer. This shows that Mg-on-Sc and Sc-on-Mg interfaces are asymmetric. A shoulder of native oxide of SiO_2 is expected to be observed at the bottom of ZrC profile, but since the fitted thickness of SiO_2 is very small (0.24nm) it is difficult to see SiO_2 on the δ-profile.

In the X-ray region, complex refractive index for matter is given by $n = 1 - \delta + i\beta$, where δ (dispersion coefficient) and β (absorption coefficient) are the optical constants. The SXR curves measured around the Sc $L_{2,3}$-absorption edge (400 eV), with energies ranging from 370 to 420 eV, are fitted and the values of optical constants δ and β are determined. The calculated values of δ and β for Sc are then plotted as a function of incident energy across the absorption edge. Using the fit values of film thickness, real part of refractive index (δ), and roughness, a depth dependent δ-profile is calculated and plotted as a function of the depth. In case of hard X-ray analyses, the δ-profiles are more analogous to mass density profiles. However, in case of soft X-rays the presence of different edges affects δ value significantly which then does not vary directly with mass density.

Near the absorption edge, refractive index is sensitive to the chemical environment, so any change in local environment of the atom will be reciprocated by the change in its optical parameters [56–58]. Thus, SXR technique can give elemental sensitive information, by tuning the energy of X-rays to the absorption edges of Sc [59,60]. The SXR fitted and measured curves for Sc/Mg bilayer, as function of incident angle at different photon energies around the Sc L absorption edge ranging from 370 to 420eV are shown in Figure 3.6.

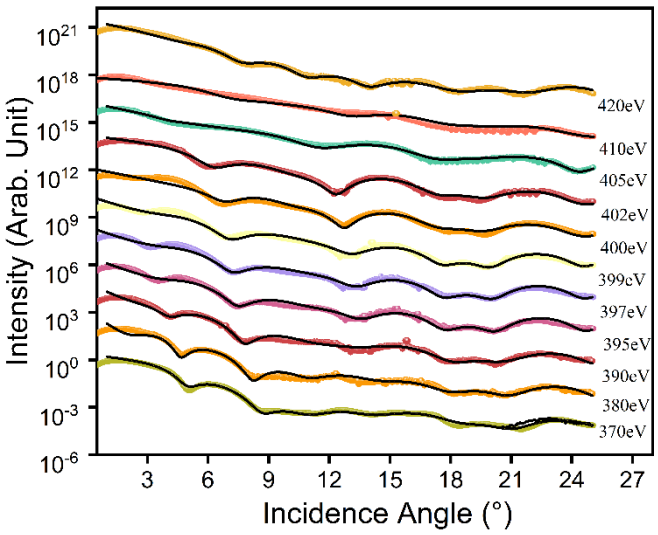

Figure 3.6 - Measured (color lines) and fitted (black solid lines) angle-dependent SXR curves at energies across the Sc L2,3 absorption edge.

The structural parameters, thickness and roughness of the various layers and interlayers, determined from the GIXRR analysis are now used to build a structure suitable to fit the SXR curves. This fitting procedure only applies to the δ and β values (the thickness and roughness values deduced from GIXRR analysis are now considered fixed). The calculated δ and β values of the Sc layer are plotted in Figure 3.7 (a) and (b) in comparison to the tabulated values as and CXRO values obtained from online database [61]. Close to the Sc edge (400 eV) the anomalous behaviour is evidenced by the negative values of the δ parameter. The β parameter is low before the edge and then increases sharply owing the empty Sc d states. A scale difference for both δ and β curves is observed in comparison with CXRO database at Sc-$L_{2,3}$ edge. At lower energies below the absorption edge, the δ values of Sc are similar to those of CXRO.

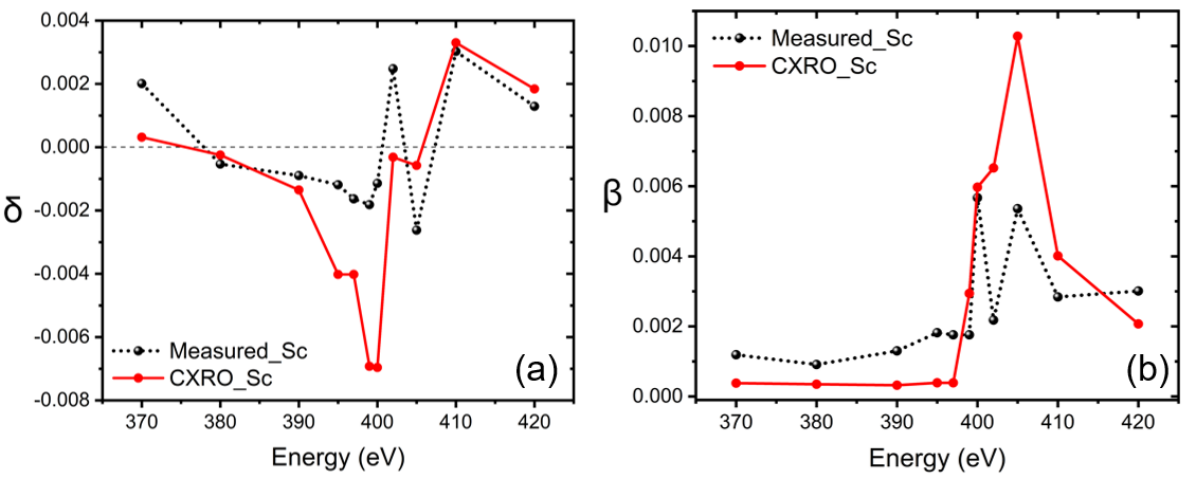

Figure 3.7 - Dispersion (δ) (a) and absorption (β) (b) coefficients of Sc layer for photon energies in the vicinity of the Sc L2,3 edge extracted from the fit of SXR curves and compared to CXRO tabulated values.

In conclusion we can say that an intermixing between the Mg and Sc layers takes place with an asymmetric behaviour between both Sc-on-Mg and Mg-on-Sc interfaces. This confirms the need to insert barrier layers at the interfaces of Mg/Sc stacks. Hence, four different types of systems were fabricated and characterised with the insertion of ZrC as barrier and capping layer at Mg/Sc interfaces.

3. [Sc(20nm)/ZrC(2nm)/Mg(20nm)/ZrC(2nm)]– Sc/ZrC/Mg/ZrC

Given in figure 3.8 is the measured ToF-SIMS spectra for ***Sc/ZrC/Mg/ZrC*** quadrilayer, with Sc^+, Mg^+, C^+, Zr^+ and Si^+ ion profiles. The different regions depicting different layers are marked by dotted vertical lines on the ToF-SIMS profile. The region from 0 to 25 s is the contamination layer followed by uniform Sc layer, followed by ZrC thin layer. The Mg layer situated between the two ZrC barrier layers shows a strange behaviour, such that both at ZrC-on-Mg and Mg-on-ZrC interfaces, we can see that the green Mg profile progresses towards the two ZrC layers trying to be on top of them. This can result in the intermixing at the ZrC-on-Mg and Mg-on-ZrC interfaces. Hence, we can assume that the a priori structure could be: [Surface-layer/Sc/ZrC/Inter-layer1/Mg/Inter-layer2/ZrC/SiO_2]/Sisubstrate or [Surface layer/Sc/ZrC/Inter-layer1/Mg/Inter-layer2/ZrC/Inter-layer 3]/Sisubstrate.

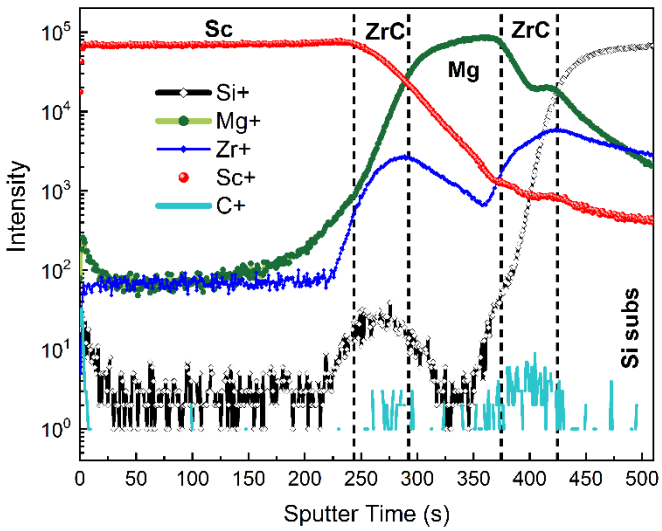

Figure 3.8 - ToF-SIMS profile of Sc/ZrC/Mg/ZrC quadrilayer obtained with O_2^+ ion gun.

Two different reflectivity fitting models were considered to fit the GIXRR curve of the quadrilayer system. At first, we considered a five-layer model. The fitted curve is shown in figure 3.9 and the structural parameters deduced are given table 3.4. In this model, a part of the Sc layer is oxidised with 11.73 nm of uniform Sc layer. The fitted density of two ZrC layers is less than the bulk density of 6.89 g/cm^3. It was also found that the Mg layer is completely oxidised with fitted thickness far less than the expected thickness of 20 nm. The thickness of Sc layer is also reduced to half as compared to the expected thickness of 20 nm. As seen in the SIMS profiles in figure 3.8, long tails of Sc and Mg are seen in the first ZrC layer and a tail of Mg profile progressing into the second ZrC layer. This kind of progression points towards a possible interdiffusion at Sc-on-ZrC, ZrC-on-Mg and Mg-on-ZrC interfaces. This could therefore explain reduced density of the two ZrC layers in the fitted GIXRR model in table 3.4.

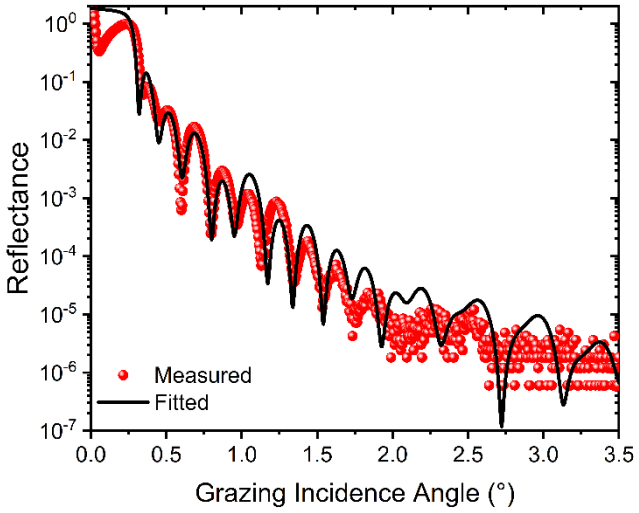

Figure 3.9 - Measured Sc/ZrC/Mg/ZrC quadrilayer GIXRR curve fitted using a five-layer model.

Table 3.4 - Structural and optical parameters of the Sc/ZrC/Mg/ZrC quadrilayer, where z is thickness of each layer, σ being the roughness of each layer δ and β are the dispersion and absorption coefficients. The thicknesses and roughness's are given ±0.1 nm.

Layer	**Z (nm)**	**σ (nm)**	**δ (x 10^{-6})**	**β (x 10^{-7})**
Sc_2O_3	0.92	0.77	13.14	6.15
Sc	11.73	0.34	9.09	6.83
ZrC	1.80	0.17	12.26	6.12
MgO	6.63	0.57	11.80	1.25
ZrC	2.22	0.32	16.89	8.41
Si Susbtrate	-	0.20	-	-

Hence, we considered another model to fit the reflectivity curve by taking into account the interfacial layers at the three interfaces of: Sc-on-ZrC, ZrC-on-Mg and Mg-on-ZrC. Figure 3.10 shows GIXRR fitted curve using a new nine-layer model, whose structural

parameters are listed in table 3.5. In this model both Sc and Mg layers are considered to be completely oxidised with a presence of surface contamination layer on top of the Sc layer. Formation of interlayers at Sc-on-ZrC and ZrC-on-Mg with thickness 2.16 nm each is deduced. During the deposition of ZrC thin film, pure Zr target is used while C is infused into the deposition chamber to facilitate the deposition of ZrC thin film. The infusion of carbon into the chamber could result in the diffusion of C atoms into the subsequent Sc and Mg layers resulting in the formation of a Sc_xC_y and Mg_xC_y interlayer where x and y denote the stochiometric composition in which the two compounds might exist.

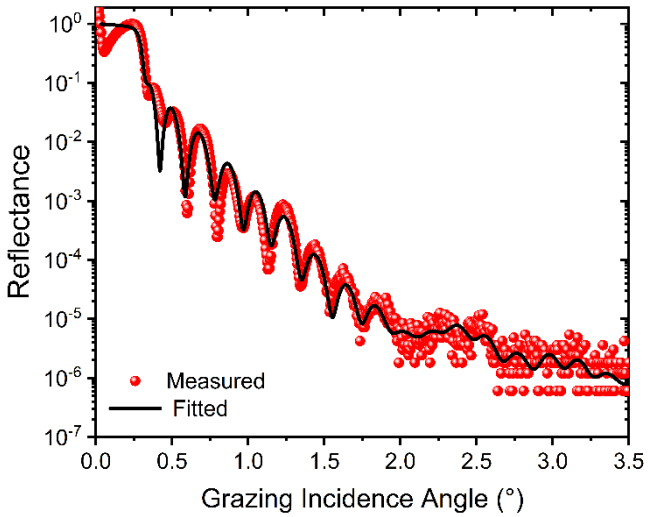

Figure 3.10 - GIXRR fitted curve with the new quadrilayer model.

Table 3.5 - Structural and optical parameters of the Sc/ZrC/Mg/ZrC quadrilayer, where z is thickness of each layer, σ being the roughness of each layer δ and β are the dispersion and absorption coefficients.

Layer	**Z (nm)**	**σ (nm)**	**δ ($\times 10^{-6}$)**	**β ($\times 10^{-7}$)**
Surface layer	1.01	0.723	8.91	1.7
Sc_2O_3	11.08	0.539	14.35	6.7

Sc_xC_y	2.16	0.823	13.20	6.7
ZrC	3.00	1.075	17.7	8.3
$Mg_xO_yC_z$	2.16	0.96	13	8.3
MgO	2.87	1.16	11.3	6.7
ZrC	2.14	*0.24*	*20.7*	*8.3*
SiO_xC_y	1.75	0.76	7.79	0.94
SiO_2	3.75	0.59	8.40	0.94
Si Substrate	-	0.20	7.55	1.7

Different studies on Sc-C system shows the formation of different possible scandium carbides namely: ScC (3.54 g/cm^3), Sc_2C (3.27 g/cm^3), Sc_4C_3 (3.83 g/cm^3) [62,63]. The formation of scandium carbide can also be attributed to the negative mixing enthalpy between the Sc and C as shown by the blue curve in figure 3.11 [53]. A negative mixing enthalpy indicates that Sc and C can mix easily to form different compounds. The Sc_xC_y interlayer formed at Sc-on-ZrC layer as a result of the diffusion of carbon atoms. It is however difficult to precisely stipulate the exact stochiometric composition of the compound formed. We can only say that since the fitted density of the Sc_xC_y interlayer is closer to that of the Sc_4C_3, this could indicate that our interlayer is of the same compound.

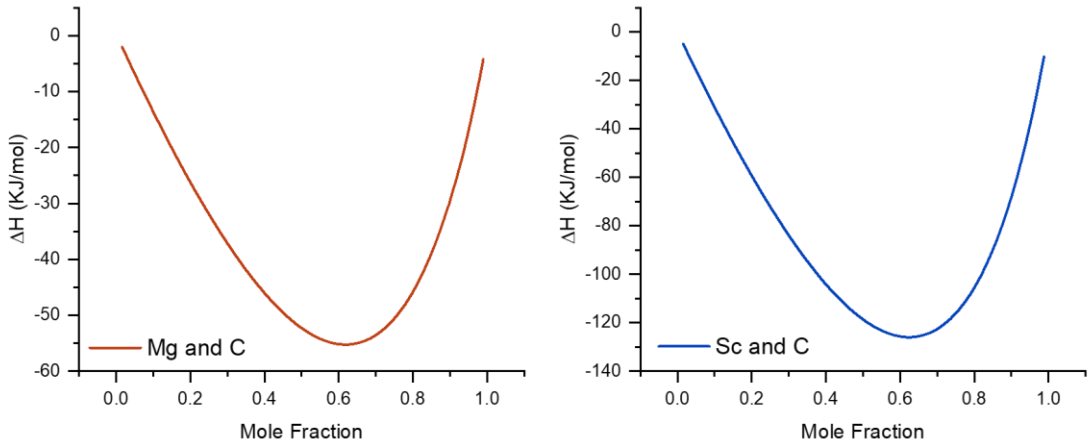

Figure 3.11 - Schematic of enthalpy of mixing between Mg and C (in Red) and between Sc and C (in blue) [54].

Figure 3.11 also shows the trend of the enthalpy of mixing between Mg and C. Similarly, here the negative mixing enthalpy leads to the intermixing of the two layers resulting in the formation of magnesium carbide (Mg_xC_y). Mg_2C_3 and MgC_2 are two compounds that have been found to be most likely formed at the intermixing of the two elements [64]. The C-on-Mg and Mg-on-C interfaces have been studied extensively in the $[C/Mg/C]_{x5}$ multilayer [65]. In case of the multilayer system, it was found that Mg layer is completely oxidised. This is explained by the intermixing at C-on-Mg and Mg-on-C interfaces. The study shows that MgC interlayer formed is porous and has considerable defects, that could allow oxygen or water vapour to penetrate into the interlayer. This explains the formation of mixed interlayer of $Mg_xO_yC_z$ interlayer at the ZrC-on-MgO interface. The formation of SiO_xC_y at ZrC-on-SiO2 interface could be explained in the similar manner, owing to the presence of native oxide on the Si substrate.

4. [ZrC(2nm)/Sc(20nm)/ZrC(2nm)/Mg(20nm)] qudrilayer – ZrC/Sc/ZrC/Mg

As seen in case of Sc/ZrC/Mg/ZrC quadrilayer, the top scandium layer was oxidised. We now study a new quadrilayer where ZrC is introduced as both capping and barrier layer in at the Sc-on-Mg interface. The capping layer is meant to prevent the stack from oxidation. The measured ToF-SIMS profile for ZrC/Sc/ZrC/Mg quadrilayer system is shown in figure 3.12.

Both Cs+ and O_2^+ ion guns were used to record the negative and positive ions respectively. The progression of profiles of different ions is not very well defined as in case of the previous samples. In case of SIMS profile measured with O_2^+ ion gun, the region from 0 to 25 s is the contamination layer. The ZrC profile can be seen both near the surface as well near the Si substrate in relation to its position in the quadrilayer stack, with the uniform Sc profile in the region from 25 to 125 s. The Mg profile (in blue) despite of its position below the two ZrC thin films in the stack, tries to progress on top of ZrC profile (in green). A similar behaviour is seen with the Cs^+ ion gun measured SIMS profile. The MgO^- profile moves at the top of that of the ZrC profile, present between 100 and 130 s near the substrate. The progression of Mg+ and MgO- in such a manner can indicate the diffusion of the Mg atoms into the above layers resulting in the formation of an interlayer at the ZrC-on-Mg interface. The ZrC-on-Sc and Sc-on-ZrC interfaces seem rather stable. Some intermixing at Mg-on-Si substrate could also be expected owing to the long Mg tails progressing into the Si substrate. The quadrilayer structure could be: [surface-layer layer/ZrC/Sc/ZrC/Interlayer/Mg/Interlayer]/Si substrate.

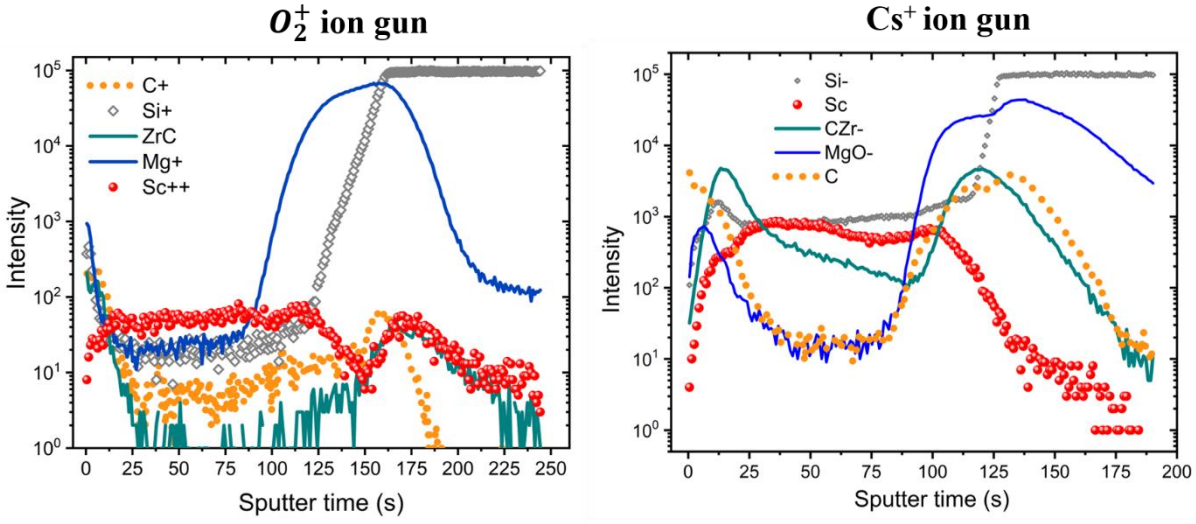

Figure 3.12 - ToF-SIMS profile for ZrC/Sc/ZrC/Mg quadrilayer obtained with O_2^+and Cs+ ion guns.

Figure 3.13 shows the experimental and fitted GIXRR curve for the ZrC/Sc/ZrC/Mg quadrilayer. The best fit was obtained with a seven-layer model, with the deduced structural

parameters listed in table 3.6. The fitted model matches well with the expected structure from the SIMS analysis. At the top we have a surface layer formed due to contamination/oxidation. It is then followed by the ZrC layer whose fitted density is less than the bulk density of 6.73g/cm3. This could be due to some of the carbon atoms being oxidised forming a surface layer. The Sc layer however is uniform with density close to that of the bulk. The barrier ZrC layer at Sc-on-Mg, is presented with density fitted density much less than the bulk. This could be due to some intermixing between the ZrC and Mg layers. Unlike the Sc layer, the Mg layer is not very uniform. A part of the Mg layer undergoes some oxidation, and some part mixes with the Si substrate with the formation of Mg_2Si interlayer. The proof of this interlayer formation could also be traced back to the ToF-SIMS profile of long tail of Mg^+ ion progressing into the substrate and to the presence of a subtle shoulder at the Mg/Si interface in the Cs^+ ion gun measured spectra. It should be noted that a defined layer structure is needed to fit the reflectivity curve and it is not possible to guess the anomalous progression of Mg layer on top of the ZrC layer, as found in SIMS.

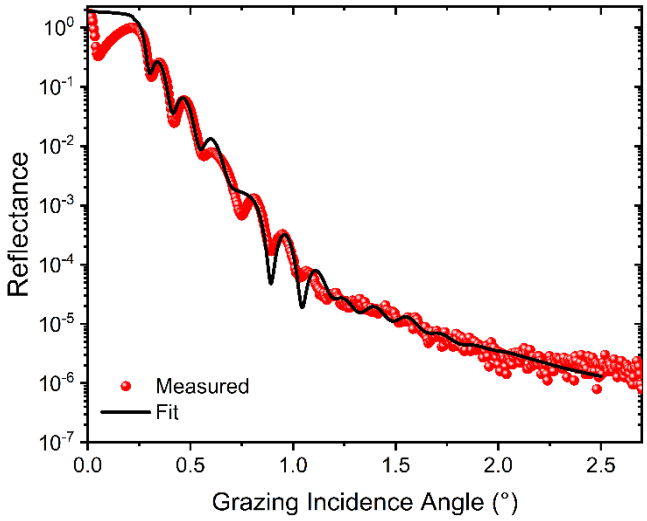

Figure 3.13 - Experimental and fitted GIXRR curves for ZrC/Sc/ZrC/Mg quadrilayer at 8048 eV.

Table 3.6 - Structural and optical parameters of the ZrC/Sc/ZrC/Mg quadrilayer, where z is thickness of each layer, σ being the roughness of each layer δ and β are the dispersion and absorption coefficients. The thicknesses and roughness's are given ±0.1 nm.

Layer	**Z(nm)**	**σ (nm)**	**δ ($\times 10^{-6}$)**	**β ($\times 10^{-7}$)**
Surface Layer	1.18	1.19	7.32	3.54
ZrC	2.72	1.52	17.3	8.39
Sc	20.44	1.33	9.09	6.83
ZrC	2.71	0.79	8.81	4.40
Mg	6.40	0.13	5.17	0.77
MgO_xC_y	0.58	1.24	13.7	1.46
Mg_2Si	0.30	1.18	4.28	0.76
Si substrate	-	0.88	-	-

5. [ZrC(2nm)/Sc(20nm)/ZrC(2nm)/Mg(20nm)] quadrilayer - ZrC/Mg/ZrC/Sc

In this case, we study the Mg-on-Sc interface with ZrC thin film. Figure 3.14 shows the ToF-SIMS spectra recorded with O_2^+ and Cs+ ion guns sputtering ZrC/Mg/ZrC/Sc quadrilayer. Similarly, here the top layer is contaminated. In the two ToF-SIMS spectra, the Mg^+ and MgO^- ion profiles try to be on the top of first ZrC layer. As we saw in previous systems, such a migration could to intermixing between the two layers. The Sc layer is uniform with no sign of diffusion with the above ZrC layer. An interlayer at the Sc-on-Si substrate could be expected as the two are prone to intermixing. This interlayer formation has been discussed in detail in case of Mg/Sc bilayer above.

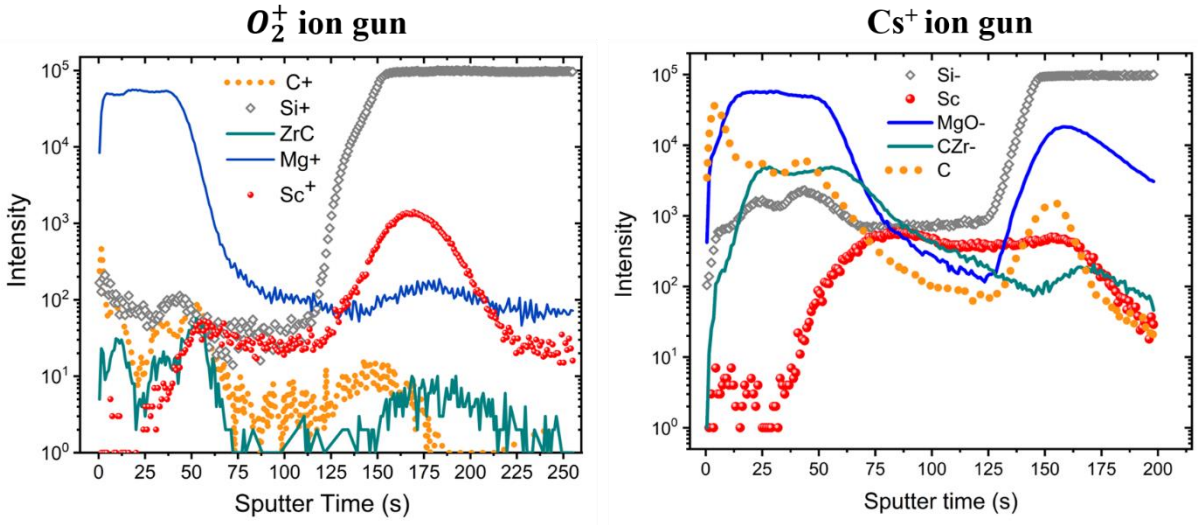

Figure 3.14 - ToF-SIMS profile for ZrC/Mg/ZrC/Sc quadrilayer obtained with O_2^+and Cs+ ion guns.

Figure 3.15 shows the experimental and fitted XRR curves using the six-layer model given in table 3.7. The Mg and Sc layers are found to be uniform with the fitted density slightly higher than the bulk. The fitted thickness of Sc layer is much less than the expected thickness of 20 nm. A ScSi interlayer is formed at the Sc-on-Si substrate interface. The second layer of ZrC thin film at Mg-on-Sc interface also has a reduced density of 5.31 g/cm3. It can also be seen that there is a discrepancy in the fitting at lower angles from 0.1° to 0.5°. We learnt from the ToF-SIMS spectra that Mg tries to migrate on top of the ZrC layer and from the fitted GIXRR curve that the fitted density of the top layer is close to Mg and far away from that of the ZrC. This could indicate the possibility that during deposition Mg diffuses towards the top of the stack and thus the deposition is not purely ZrC but a mix of Zr, Mg and C or even O.

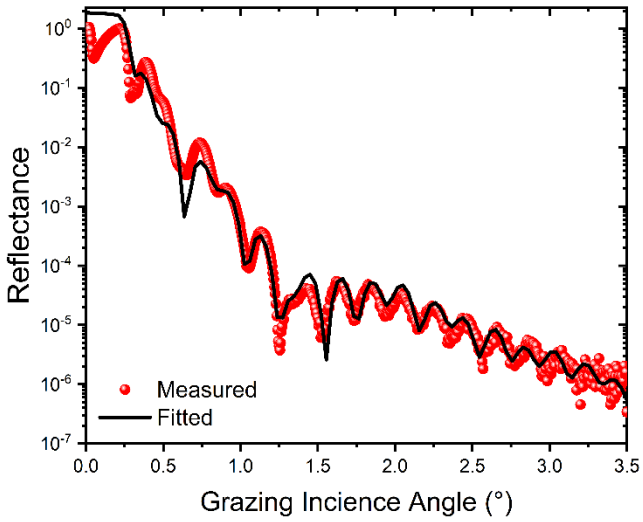

Figure 3.15 - Experimental and fitted GIXRR curves for ZrC/Mg/ZrC/Sc quadrilayer at 8048 eV.

Table 3.7 - Structural and optical parameters of the ZrC/Mg/ZrC/Sc quadrilayer, where z is thickness of each layer, σ being the roughness of each layer δ and β are the dispersion and absorption coefficients. The thicknesses and roughness's are given ±0.1 nm.

Layer	**Z (nm)**	**σ (nm)**	**δ ($x10^{-6}$)**	**β ($x10^{-7}$)**
ZrC	1.70	0.15	6.65	3.32
MgO	1.56	0.21	10.19	1.08
Mg	8.13	0.39	5.90	0.87
ZrC	2.70	0.77	14.72	7.35
Sc	8.39	0.44	9.35	7.03
ScSi	0.37	0.37	9.80	5.31
Si substrate	-	0.32	-	-

3.2.4 Conclusions drawn from ZrC based Mg/Sc systems

The interface analysis of Mg-on-Sc and Sc-on-Mg interfaces, was done in a scheme of different combinations of samples with and without the presence ZrC thin film. The samples were characterised mainly by X-ray reflectivity (using hard and soft X-rays) and ToF-SIMS. ToF-SIMS was useful as a first step in the analysis to limit the number of possible structures used in the process of fitting reflectivity curves and to give an idea of the *a priori* structure of the stack. All the samples had a contamination layer at the top leading to the oxidation of the top surface layer. In case of Sc/Mg and Mg/Sc bilayers, an intermixing between the Mg and Sc layers takes place with an asymmetric behaviour at the Sc-on-Mg and Mg-on-Sc interfaces respectively. ZrC thin film was then introduced both as the capping as well as the barrier layer in the new quadrilayer systems: Sc/ZrC/Mg/ZrC (quadrilayer1), ZrC/Sc/ZrC/Mg (quadrilayer 2) and ZrC/Mg/ZrC/Sc (quadrilayer3). In quadrilayer 1, an interlayer at all the interfaces was found whereas in other two quadrilayers 2 and 3, the Sc-on-ZrC and ZrC-on-Sc interfaces were found to be rather stable with no intermixing between them. Mg and ZrC layers, however resulted in an interlayer formation in all cases.

Soft X-ray reflectivity measurement shown in figure 3.16, was done on the then fabricated $[Sc(3nm)/Mg(3nm)]_{x25}$ multilayer. The reflectivity curves were recorded as a function of incident photon energy around the Sc L-absorption edge at different glancing angles ranging from 12.2° to 13.4°. The multilayer showed 27% reflectivity when measured at an incidence angle of 12.6° at 405 eV. Hence this multilayer system can be a good candidate for X-ray spectroscopy in the N K emission range.

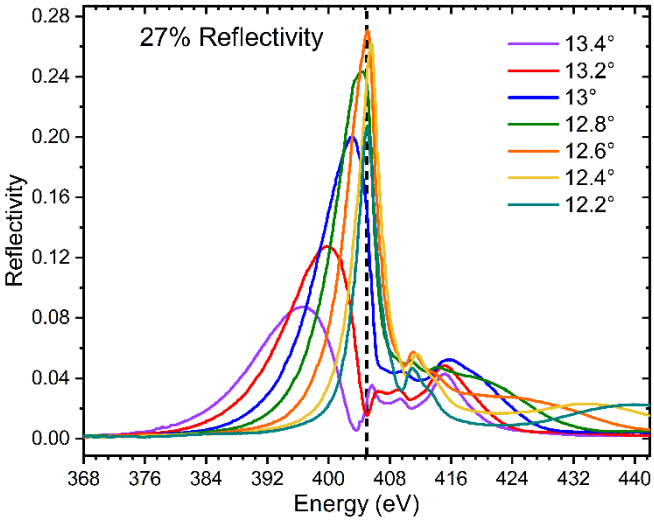

Figure 3.16 - Soft X-ray reflectivity measurement done for [Sc/Mg]x25 multilayer.

As seen from the Sc/Mg bilayer, intermixing at the Sc-on-Mg interface is expected. Also, with the passage of time, the interface tends to degrade further. Hence there is a need for the barrier layer that can prevent intermixing. As seen from the samples characterized above, the introduction of the ZrC thin film did not fully play the role of barrier layer in the Mg-Sc systems. Therefore, a new set of samples with the inclusion of Cr thin film were fabricated and studied.

3.3 Study of Cr based Mg/Sc systems

3.3.1 Sample Preparation

Magnetron sputtering was used for the deposition at room temperature of samples on a Si (100) substrate using high purity Cr, Mg and Sc targets. The argon pressure inside the chamber was maintained at 0.43 mbar during deposition. The base pressure was $2x10^{-7}$ mbar. The deposition rates used for Cr, Mg, Sc were 0.15 nm/s, 0.06 nm/s, and 0.07 nm/s respectively with 150 W power set at each of the sputtering targets.

3.3.2 Characterization

We performed X-ray reflectivity (XRR) in combination with GIXRF at metrology beamline using CASTOR (*Chambre d'Analyse Spectrométrique en Transmission ou en*

Réflexion) instrument [49] at SOLEIL. The measurement was done on the hard X-ray branch (100 eV to 40 keV). The reflectivity is obtained by measuring the current at the photodiode at varying grazing incidence angles and the fluorescence spectra is recorded at the energy dispersive silicon drift (SDD) detector located at right angle with respect to the incident beam. The measurements were taken at an incident photon energy of 6.25 keV. The choice of this measurement energy was made to be sufficiently above the K-edges of elements of interest present in the system, *i.e.* 5.987 keV for Cr, 4.486 keV for Sc and 1.309 keV for Mg. The reflectivity data was recorded from 0° to 3° with an angular step of 0.004°. The energy dispersive X-ray fluorescence spectra were measured on the same range but at varying angular steps.

For every grazing incidence angle, the measured energy dispersive spectrum was calibrated along with background subtraction and then fitted with Colegram software [66] using batch processing. The area under the peak of each element was then deduced for each incidence angle thereby resulting in an angle dependent fluorescence curve. This curve calculated for each element of a particular sample is then fitted simultaneously with the measured reflectivity to simulate the structure of the stack using ELIXIR software. In this way we obtained the information of thickness, density and roughness of each layer and possible interlayers from the combined XRR-GIXRF fit. This approach was applied for the analysis of all the samples. Further details of the results obtained from the measured and fitted XRR and GIXRF data have been discussed in detail separately for each sample in the section below.

An example of the fitted fluorescence spectra summed over different angles of acquisition for Cr/Mg/Sc trilayer is shown in figure 3.17. The measured emission lines of Si $K_{\alpha 1,2}$, Mg $K_{\alpha 1,2}$, Sc ($K_{\alpha 1,2}$, $K_{\beta 1}$) and Cr ($K_{\alpha 1,2}$, $K_{\beta 1}$) have been analysed. As seen from the spectra, the Mg $K_{\alpha 1,2}$ peak has the lowest intensity and is present in the left tail of the Si $K_{\alpha 1,2}$ emission peak. For the measurement done at low angles, it was observed the Mg peak was almost absorbed in the tail of the Si K peak and it was difficult to extract the Mg peak area. We encountered this problem with all our samples containing Mg i.e. in case of Cr/Mg bilayer Mg/Sc bilayer and Cr/Mg/Sc trilayer (as shown here). Hence, only the angle dependent

fluorescence extracted curves for Cr (for this sample) and Sc (for other samples with Sc thin film) have been discussed

In the fluorescence spectra we also observe a peak of high intensity around 2400 eV. This peak is termed as an escape peak and is the result of the interaction of X-ray photon with the Si atoms present in the SDD detector. This results in the ejection of the electron from the Si K shell, and hence an emission of characteristic Kα X-rays in the detector. These characteristic X-rays then appear as a separate peak in the fluorescence spectrum with reduced energy from the energy of parent X-rays where it arises. In this spectra, the energy of the peak is given by, $E_{escape\ peak} = E_{(Sc\ K\alpha 1,2)} - E_{(Cr\ K\alpha 1,2).} = E_{(Cr\ K\alpha 1,2)} = 1.74$ keV.

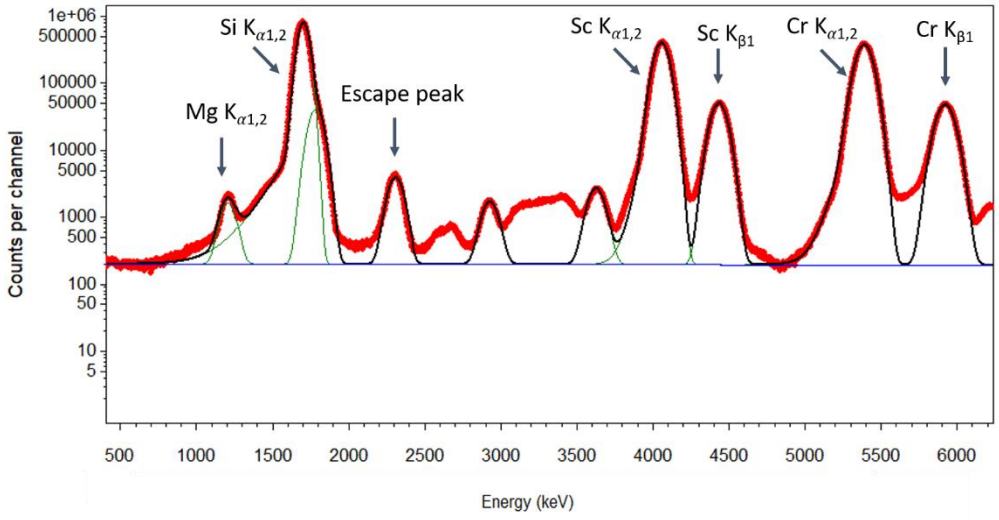

Figure 3.17 - The experimental spectrum is shown in red; fits are shown in black. Mg Kα1,2, Si Kα1,2, Sc Kα1,2 and Cr Kα1,2 lines are fitted with gaussian (with left tail) and the rest are fitted with gaussian (sigma) function. The background is represented by the by the blue line and is subtracted before the peaks of interest are fitted.

3.3.3 Results and Discussion

1. [Cr(20nm)/Mg(20nm)] bilayer – Cr/Mg

Figure 3.18 shows the measured and fitted combined XRR-XRF curves, and the derived structural parameters are listed in table 3.8. The fitted structure is a four-layer system, where

the top Cr is layer is found to be completely oxidised (with CrO_3 and Cr_2O_3), followed by Mg layer and a native oxide layer on top of Si substrate. Extensive studies on Cr thin films found that the film is very readily oxidised and is prone to surface contamination easily. Different experimental investigations shows the formation of Cr_2O_3, CrO, CrO_3, CrO_2, Cr_3C_2 compounds on Cr thin film [67–70]. The fitting of the XRF part takes into account the mass fraction of all the elements and compounds in each layer. Therefore, different combination of Cr-oxides and Cr-carbide were considered and the best fit in this case was obtained with Cr_2O3 and CrO_3 oxides of Cr. We found the presence of Cr_2O_3 in all the sample and CrO_3 in most cases (except for trilayer, discussed below). Next, the thickness of the Mg layer is much less than the aimed thickness of 20 nm with density close to the bulk. The Cr-on-Mg interface is presented with a high roughness of 1.17 nm but no interlayer formation has been observed.

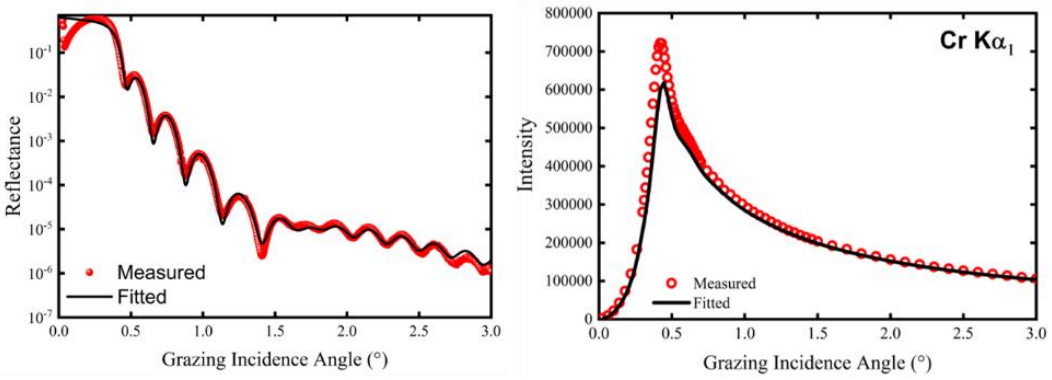

Figure 3.18 - Combined XRR-GIXRF fit of the Cr/Mg bilayer.

Table 3.8 - Calculated structure from the XRR-GIXRF combined fitting for Cr/Mg bilayer. The thicknesses and roughness's are given ±0.1 nm.

Layer	**Z (nm)**	**σ (nm)**	**ρ (g/cm^3)**
CrO_3	1.92	0.87	2.641
Cr_2O_3	20.65	0.14	4.842
Mg	4.43	1.17	1.738
SiO_2	0.16	1.06	2.7

Si substrate	-	0.25	-

2. [Cr(20nm)/Sc(20nm)] bilayer – Cr/Sc

The combined fitting analysis of Cr/Sc shown in figure 3.19, yields the structure given in table 3.9. The best fit was obtained with a four-layer structure where the top Cr layer is completely oxidised. The oxidation of the Cr film shows the presence of CrO_3 and Cr_2O_3 oxides. Sc layer however is found to be uniform with no oxidation, with the density slightly less than the bulk density of 2.89 g/cm^3. The deposited Sc thickness was also found to be much lower than the expected thickness of 20 nm. The Cr-on-Sc interface was found to be rather stable with small roughness and no intermixing.

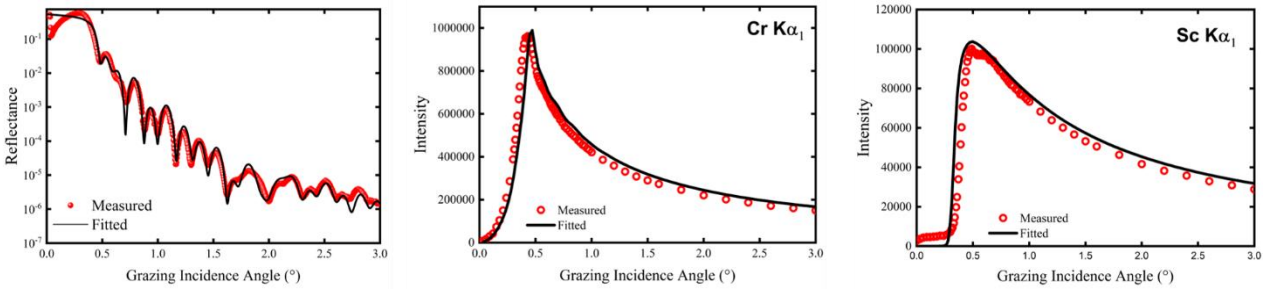

Figure 3.19 - Combined XRR-GIXRF fit of Cr/Sc bilayer.

Table 3.9 - Calculated structure from the XRR-GIXRF combined fitting for Cr/Sc bilayer. The thicknesses and roughness's are given ±0.1 nm.

Layer	**Z (nm)**	**σ (nm)**	**ρ (g/cm^3)**
CrO_3	0.99	0.74	1.78
Cr_2O_3	30.23	0.93	3.23
Sc	12	0.15	2.76
SiO_2	2.31	0.51	2.59

Si substrate	-	0.52	2.33

3. Cr(2nm)/[Mg(20nm)/Sc(20nm)] bilayer – Mg/Sc

As seen in the previous case of Mg/Sc bilayer (discussed above), a part of the top Mg layer was oxidised. To prevent the Mg/Sc bilayer from oxidation, a capping layer of Cr has been added. Table 3.10 shows the fitted structure of the combined XRR-XRF of Mg/Sc bilayer, figure 3.20. As expected, the top Cr layer is oxidised. Since the thickness of the Cr film is small ~ 4nm, the oxide layer further oxidises a part of the Mg layer also. Significant intermixing at the Mg-on-Sc interface results in MgSc interlayer formation. The fitted density of the Sc layer was found to be slightly lower than the bulk. Formation of Sc_2O_3 was also seen at the interface between Sc and Si substrate.

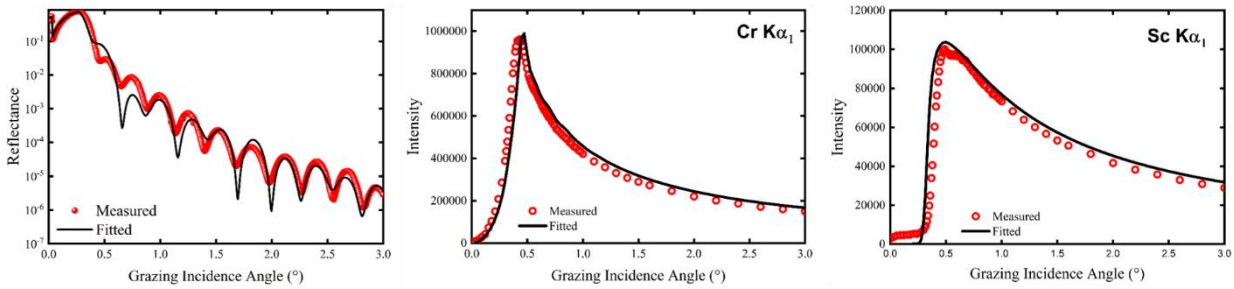

Figure 3.20 - Combined XRR-GIXRF fit of the Mg/Sc bilayer with Cr capping layer.

Table 3.10 - Calculated structure from the XRR-GIXRF combined fitting for Cr/(Mg/Sc) bilayer. The thicknesses and roughness's are given ±0.1 nm.

Layer	**Z (nm)**	**σ (nm)**	**ρ (g/cm^3)**
CrO_3	2.51	0.44	2.6
Cr_2O_3	1.18	0.43	4.3
MgO	4.27	0.11	3.73

MgSc	2.63	0.69	2.53
Sc	7.6	0.15	2.59
Sc_2O_3 interlayer	2.24	0.4	4.32
Si substrate	-	0.2	-

4. [Cr(4nm)/Mg(16nm)/Sc(21nm)] Trilayer – Cr/Mg/Sc

Figure 3.21 shows the combined XRR-XRF fit of the Cr/Mg/Sc trilayer and the corresponding structural parameters are given in table 3.11. In this case also the Cr layer seems to be oxidised with the presence of CrO and Cr2O3 oxides. It should be noted that for the top CrO layer the fitted density is much higher than the bulk density of 2.7 g/cm^3. This means that the top layer is not composed of pure oxide but has some contamination that leads to the increase in density. It is then followed by the Mg layer that is decomposed in three parts: MgO, Mg and MgSc layers. The Mg layer in between the MgO and MgSc layers has a density ~32% higher than the bulk density of 1.738 g/cm^3. This increase in density can be explained by the fact that this layer might have some diffused oxygen or scandium atoms from the surrounding layers present in it. A uniform layer of Sc with density close to the bulk is found. However, this layer intermixes with the Si substrate and the native oxide present on the substrate to have three layers of ScSi, Sc_2O_3 and SiO_2.

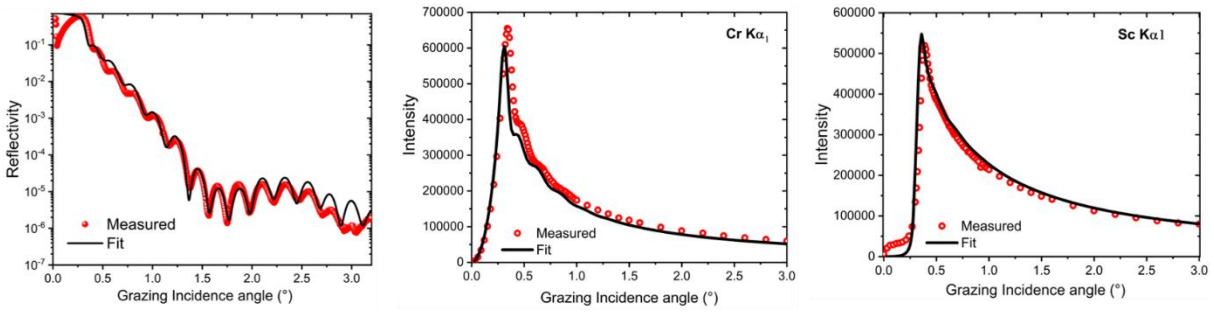

Figure 3.21 - Combined XRR-GIXRF fit of the Mg/Sc bilayer with Cr capping layer.

Table 3.11 - Calculated structure from the XRR-GIXRF combined fitting for Cr/(Mg/Sc) bilayer. The thicknesses and roughness's are given ±0.1 nm.

Layer	**Z (nm)**	**σ (nm)**	**ρ (g/cm^3)**
CrO	1.80	0.42	3.72
Cr_2O_3	1.66	0.38	5.97
MgO	2.25	0.38	3.99
Mg	5.51	0.70	2.3
MgSc	3.93	0.42	2.65
Sc	8.99	0.28	2.89
ScSi	1.30	0.35	3.48
Sc_2O_3	0.52	0.45	3.67
SiO_2	1.53	0.16	2.83
Si substrate	-	0.23	-

3.3.4 Conclusions drawn from Cr based Mg/Sc systems

The analysis of the Cr based Mg/Sc systems show that the interfaces Cr-on-Mg and Cr-on-Sc are quite stable and do not show any intermixing. The top Cr layer is completely oxidised. Two multilayers of:

1. Cr(2nm) $[Cr(1nm)/Mg(3.5nm)/Sc(1.5nm)]_{x50}$ – $[Cr/Mg/Sc]_{x50}$

2. Cr(2nm) $[Mg(3.5nm)/Cr(1nm)/Sc(1.5nm)]_{x50}$ – $[Mg/Cr/Sc]_{x50}$

were fabricated and characterised using the combined XRR-XRF measurement. The XRR curve recorded for both the multilayers is shown in figure 3.22. The reflectivity curve for $[Cr/Mg/Sc]_{x50}$ shows the presence of three Bragg peaks, with a rapid decrease in the slope of

the reflectivity curve. Contrary to the stable interfaces found in Cr/Mg and Cr/Sc bilayer, the reflectivity of the $[Mg/Cr/Sc]_{x50}$ multilayer is very poor, with no Bragg peaks. This could be explained by a low thickness of the Cr thin film which might not have been achieved and the Mg and Sc layers intermixed as result thereby destroying the structure of the stack. Owing to a complex structure found in Mg/Sc bilayer and Cr/Mg/Sc trilayer, it was difficult to deduce a combined XRR-XRF fitted structure the $[Cr/Mg/Sc]_{x50}$ multilayer.

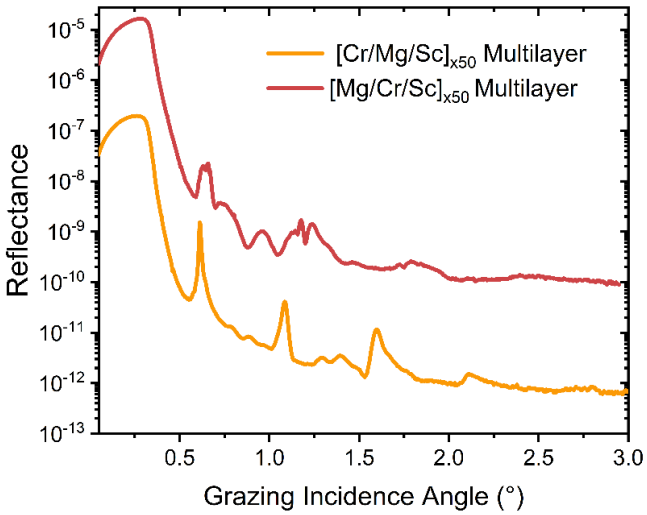

Figure 3.22 - GIXRR curve for $[Cr/Mg/Sc]_{x50}$ and $[Mg/Cr/Sc]_{x50}$ multilayers measured at photon energy of 6.25keV.

3.4 Conclusion

No inter diffusion at Cr-on-Mg and Cr-on-Sc interfaces could be used as a plus point to design a multilayer system. A simulation of Sc/Cr/Mg multilayer shown in figure 3.23, shows a reflectance of 48% around N K edge, 395 eV. A capping layer of B_4C is used to prevent the top layer of the multilayer stack from oxidation. A thicker 2nm layer of Cr between Sc and Mg interfaces could prevent the intermixing the layers. However, in comparison to the simulation of Sc/Mg multilayer in figure 3.1, the reflectance of the new simulated structure, given in figure 3.23 decreases by 3%. The new structure is expected to be comparatively stable, as the analysis of the Sc/Mg bilayer proves intermixing at the interfaces, which will in turn lead to further decrease in reflectance.

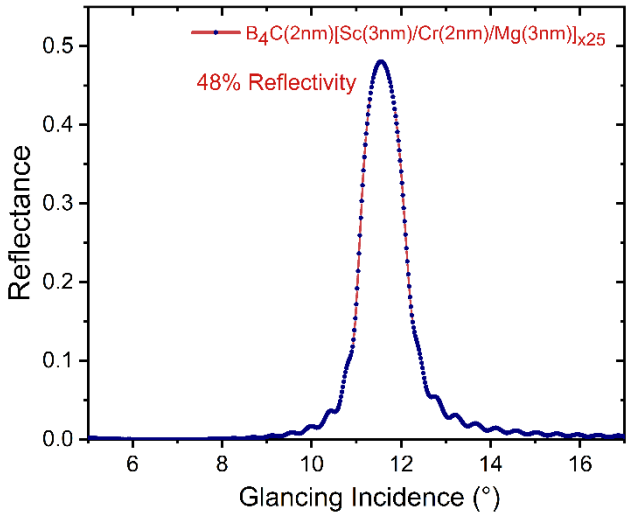

Figure 3.23 - Reflectance calculated for B4C(2nm) [Sc(3nm)/Cr(2nm)/Mg(3nm)]x50 multilayer at the incident photon of energy of N K edge (395 eV).

Chapter 4: Study of Fe/Si multilayer

4.1 Introduction

X-ray emission spectroscopy (XES) has proven to be a suited tool for analysing buried layers and interfaces [71,72]. The emission spectra allow us to study the interactions between elements in the buried layers from the analysis of their valence states. The emission band obtained as a result of the valence to core transition, has a distinct shape and width, reflecting the chemical state of the emitting element. Hence, XES was shown to provide sensitive information about the physical chemical environment of the emitting elements in multilayers [73–76]. Until now XES has been applied in soft X-ray region (photon energy $\leq$ 2 keV) to study the buried layers and interfaces.

The Fe/Si multilayer system has been of particular interest owing to its applications in microelectronics and magnetism [77]. The soft X-ray fluorescence measurements on the Fe/Si multilayer performed previously suggest that a strong interdiffusion between Fe and Si layers gives rise to a silicide layer at the interface [78]. Fe_3Si, FeSi and $FeSi_2$ silicides have been reported to be formed at the interfaces depending upon the thickness and deposition conditions of the constituting Fe and Si layers. The iron rich, Fe_3Si phase usually forms when the thickness of the Si layer is much lower than the thickness of Fe layer, followed by the FeSi and $FeSi_2$ phases with the increase in Si layer thickness with respect to that of Fe [78,79]. The Si $L_{2,3}$ emission spectra for Fe/Si multilayer, studied by Imazono et al. [78] , Carlisle et al. [80] and Watanabae et al. [81] reveal that intermixing takes place. The measured Si L emission spectra for the Fe/Si multilayer is possibly a mix of spectra of pure Si and other silicides. Similar results were obtained on the Mo/Si system, wherein the interfaces are composed of $MoSi_2$, Mo_5Si_3 [76,82]. The measured spectrum was decomposed with the reference spectra of the silicide compounds. From this decomposition, the interfacial thicknesses was deduced [81] as well as the chemical environment of the emitting element.

We want to extend this methodology to the hard X-ray range and evaluate the sensitivity of the technique in the same manner. We also performed X-ray reflectivity (XRR) measurements to obtain preliminary structure of the multilayer stack, the thickness, density of the layers and possible interdiffusion between the layers.

4.2 Sample Preparation

We prepared two Fe/Si multilayer samples. The first was made of 40 bilayers with alternating Fe and Si layers of 2.5 nm thickness each, and the second was made of 13 bilayers with alternating Fe and Si layer of thickness 3.6 nm and 4.5 nm respectively. We also prepared a reference sample of 20 nm thin film of Fe deposited on a Si substrate. Magnetron sputtering was used for the deposition at room temperature of samples on a Si (100) substrate using high purity Fe and Si targets. The argon pressure inside the chamber was maintained at 1.9×10^{-3} mbar during deposition. The base pressure was 1.7×10^{-7} mbar. The periodic Fe/Si multilayer sample made of 40 bilayers was prepared at the deposition rate of 0.32 nm/s and 0.21 nm/s respectively with 150 W power set at each of the Fe and Si sputtering targets. The 20 nm thin film of Fe was fabricated with the similar conditions. This Fe thin film sample is used as the Fe reference.

In the Fe/Si multilayer sample with 13 bilayers, the Fe and Si thicknesses were chosen so that the overall stoichiometry is $FeSi_2$. This multilayer was prepared at a deposition rate of 7.5 nm/s and 6.0 nm/s with power of 150 W and 50 W maintained at the Fe and Si targets respectively. Various silicides, FeSi, $FeSi_2$ and Fe_3Si have been reported to be formed by the intermixing of Fe and Si layers at the Fe-on-Si and Si-on-Fe interfaces [80,83]. The Fe_3Si and FeSi silicides are found to be thermodynamically stable at annealing temperatures between 400-500°C [84]. However, at higher annealing temperatures (>600°C) $FeSi_2$ forms at the expense of other silicides. It was observed that annealing temperatures between 600-700°C for 1-2 hours are sufficient to change 100 nm thick metal film deposited on a silicon substrate into a disilicide film [85–88]. From these observations, we deduce that when the $[Fe(3.6nm)/Si(4.5nm)]_{x13}$ multilayer sample is annealed at 675°C for 2 hours under vacuum, rigorous interdiffusion and intermixing occur at interfaces throughout the multilayer stack. The stoichiometry of the Fe and

Si layers along with the annealing conditions drives the formation of $FeSi_2$ in the bulk. The presence of this $FeSi_2$ was confirmed with the X-ray diffraction (XRD, see below) and the sample was used as the $FeSi_2$ reference.

4.3 Characterization

4.3.1 X-ray Diffraction

An X-ray diffraction experiment was carried out to confirm the presence of $FeSi_2$ evidenced through the analysis of XES measurements. Monochromatic Cu $K\alpha_1$ (8048 eV) radiation on a Rigaku five-circle diffractometer was used to obtain the $\theta/2\theta$ diffraction patterns of the Fe/Si multilayer and $FeSi_2$ reference in a θ-θ geometry in an angular scan ranging from 20 to 80° in 2θ.

The XRD patterns of the $FeSi_2$ and Fe/Si multilayer are shown in Figure 4.1. A narrow X-ray diffraction peak at 45.66° is found for the $FeSi_2$ reference. The other two peaks belong to Si substrate [89,90]. The position of diffraction peak for $FeSi_2$ is comparable to the diffraction peaks for $FeSi_2$ thin film on Si substrate at 45.81° [89]. It must be noted that the comparison is only done with the diffraction peaks for $FeSi_2$ thin films rather than the bulk values, since the lattice parameters in thin films could be different from the bulk ones.

Also, considering the annealing conditions and the stoichiometry of our $[Fe(3.6nm)/Si(4.5nm)]_{x13}$ sample we can rule out the presence of Fe and other iron silicides and can infer that the diffraction peak at 45.66° is due to $FeSi_2$ compound only. However, for the Fe/Si multilayer, $[Fe(2.5nm)/Si(2.5nm)]_{x40}$, a broad peak (having a width of 1.93°) is observed at 44.66°. Given this width and closeness to both diffraction peaks of Fe and $FeSi_2$, from this pattern we cannot obtain relevant information regarding the presence or not of silicide within the multilayer.

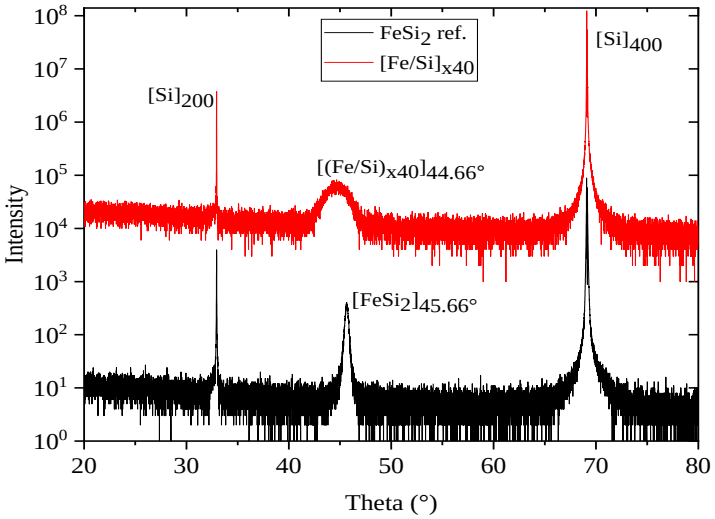

Figure 4.1 - X-ray diffraction patterns of the FeSi2 reference (black line) and Fe/Si multilayer (red line).

4.3.2 X-ray Reflectivity

XRR measurements were carried out by using a Rigaku five-circle diffractometer equipped with a monochromatized Cu $K\alpha_1$ radiation source (8048 eV). The reflectivity curve was obtained by varying the grazing incidence angle and simultaneously detecting the reflected beam in θ-2θ geometry.

XRR is used to characterize the layers of a multilayer stack, i.e. the thickness, roughness, density and composition of the different layers and interlayers of the multilayer, provided a model of the stack giving the different layers, is defined. These parameters are calculated by fitting the experimentally obtained XRR curve of the Fe/Si multilayer using the IMD code [7]. At first, we consider a two-layer model, Fe/Si to describe the stack. Since, the fit does not work well with this model we then take into account a $FeSi_2$ interfacial layer at Fe-on-Si and Si-on-Fe interfaces, i.e. we consider a four-layer model of [$Fe/FeSi_2/Si/FeSi_2$] on the Si substrate. The structural parameters obtained from fitting the four-layer model of the Fe/Si stack, shown in Figure 4.2, are given in Table 4.1. The fitted density of the interlayers is close to the one of the disilicide, 4.96 g/cm^3.

Table 4.1 - Structural parameters of the layers used in the model to describe the Fe/Si stack in order to fit the reflectivity measurement. Layers are presented from the surface down to the substrate.

Layer	Z (nm)	σ (nm)	ρ (g/cm^{-3})
Fe	1.78	0.67	7.86
$FeSi_2$	1.10	0.35	5.09
Si	1.30	0.44	2.32
$FeSi_2$	0.90	0.52	4.79
Si substrate	-	0.23	-

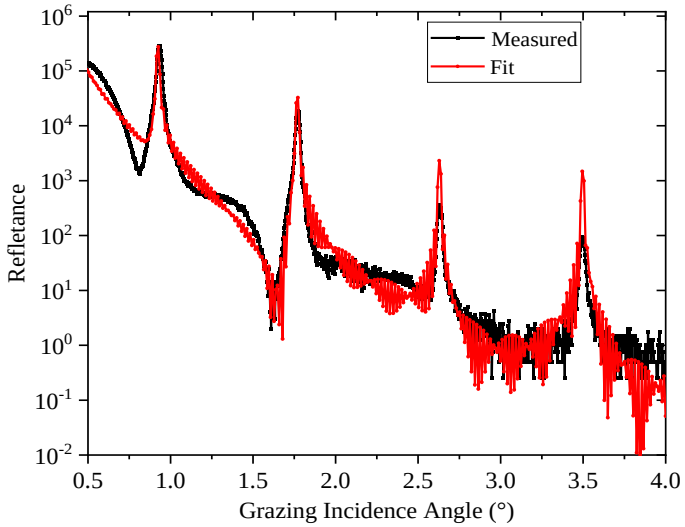

Figure 4.2 - X-ray reflectivity fit of the Fe/Si multilayer at 8048eV.

From Table 4.1, we can observe that the thickness of $FeSi_2$ layer formed at the Fe-on-Si interface is slightly higher than the thickness of $FeSi_2$ formed at the Si-on-Fe interface. Even

if this difference in thickness values is within the uncertainty, it could be attributed to the difference between the surface free energies of Fe (2.9 J/m^2) and Si (1.2 J/m^2) [91]. As the surface free energy of Si is lower than the one of Fe then during the deposition of Fe on Si, Si atoms try to move to the surface guided by the chemical driving force giving rise to intermixing between the layers. Whereas, during the deposition of Si on Fe, no such chemical driving force exists, therefore the intermixing at Si-on-Fe interface would take place as a result of random thermal motions only [92].

4.3.3 X-ray Emission Spectroscopy

X-Ray fluorescence analysis of the Fe $K\beta_{2,5}$ emission line in the Fe/Si multilayer, Fe and $FeSi_2$ reference samples were done at GALAXIES beamline [46] installed at synchrotron SOLEIL. The experimental set up was arranged in a Rowland geometry, where four Ge (620) analyser crystals collect the scattered and characteristic X-rays from the sample and focus them onto a silicon drift detector. The total spectrometer resolution was estimated at 1.5 eV (full width half maximum) from the elastic line. During the experiment it was observed that sample surface (placed in ambient air) underwent a chemical reaction due to the formation of ozone upon irradiation by the incident beam. Hence, to prevent this reaction, the sample was placed in helium atmosphere. This also increases the transmission of the incident and emitted radiations. The incident photon energy was 7500 eV. The data for each of these samples was baseline subtracted and then normalised to their maximum to plot the emission curves. The Fe $K\beta_{1,3}$ emission spectra were also measured (see supplementary information) but since the spectra of the Fe and $FeSi_2$ references were similar, not much information could be obtained about the chemical state of Fe.

4.4 Results and Discussion

To determine physical-chemical state of the Fe atoms in the multilayer, we compare the $FeK\alpha_{2,5}$ emission spectrum of the multilayer with the ones of Fe and $FeSi_2$ references, Figure 4.3. The emission band results from the electronic transition from occupied 3d to 1s levels. It is a valence to core transition and is sensitive to the chemical state of emitting Fe

atoms. The Fe $K\beta_{2,5}$ emission spectra of the multilayer and the references have their own distinct shape along with a relative shift in the position of the maximum. We can also see from the Figure 4.3 that the Fe $K\beta_{2,5}$ emission spectrum of the Fe/Si multilayer is located between those of Fe and $FeSi_2$ and then can be considered as a mix of the emission spectra of the two references, indicating the presence of an iron silicide at the interfaces in the multilayer stack.

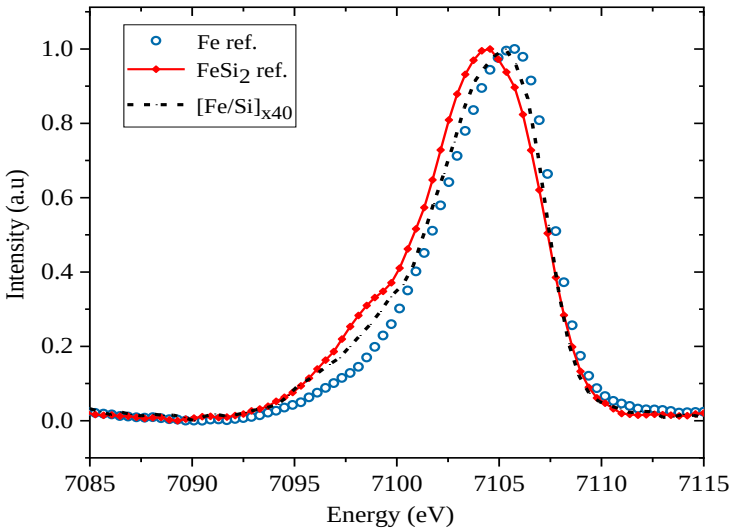

Figure 4.3 - Normalised Fe $K\beta_{2,5}$ emission spectra of the Fe/Si multilayer, Fe reference and $FeSi_2$ reference.

The spectrum of Fe/Si multilayer is fitted with a weighted sum of Fe and $FeSi_2$ spectra. Using the weighted coefficients of Fe and $FeSi_2$, we determine the thickness of the interfacial $FeSi_2$ layer in the multilayer stack with a model proposed by Miyata et al. [76]. In this model, we consider that the total Fe $K\beta_{2,5}$ intensity emitted from the multilayer is due to the contribution of the intensity emitted by iron atoms, present in the Fe layers and the $FeSi_2$ interfacial layers. The coefficients of the weighted fit are proportional to the emitted intensity of the respective layers, which is itself considered proportional to the thickness of each layer [76]. We also assume that the composition and thickness of the Fe-on-Si and Si-on-Fe interfaces are identical and that the densities of the reference compounds are equal to those of bulk compounds [76]. As only one XES measurement is performed it is not possible to use a more sophisticated model

of the stack, where the thicknesses of the Fe-on-Si and Si-on-Fe interfaces are different and thus we assume a same thickness at both these interfaces.

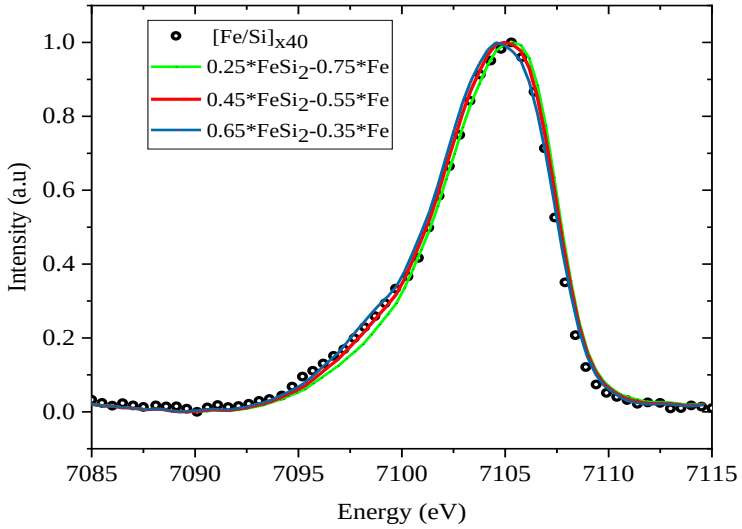

Figure 4.4 - Fits (lines) of the Fe Kβ$_{2,5}$ emission band of the Fe/Si multilayer (dots) by a weighted sum of the spectra of the reference compound. The best fit is obtained with 45%FeSi$_2$ + 55%Fe (thick line).

The weighted fit of the Fe/Si multilayer spectrum is presented in figure 4.4. The best fit is obtained with 0.55 Fe + 0.45 FeSi$_2$, with an uncertainty of about 0.2 on the coefficients. With 55% of FeSi$_2$ in the weighted sum, the thickness of the interfacial FeSi$_2$ is estimated to be 1.4 ± 0.2 nm at all interfaces, giving a total interlayer thickness of 2.8 nm. This value is larger (40%) than the thickness deduced from the XRR analysis, 2.0 nm.

However, other silicides could also be formed at the interface, but here we stress only the application of the technique used in soft X-rays to be extended with hard X-rays. Moreover, when other silicides, FeSi and Fe$_3$Si, are considered in the calculation of thickness whilst taking into account the bulk density for each, we find that the interfacial thickness increases to 1.5 nm and 1.6 nm, respectively, thus increasing the discrepancy between values deduced XRR and XES. Also, the growth kinetics, fabrication conditions as well as thickness deposited play a crucial role in determining the type of silicides formed at the interface. Hence, from XRR fit

and XES calculations we can conclude following our model that $FeSi_2$ is formed at all the interfaces with a thickness estimated to be 1.4 nm.

4.5 Conclusion

We studied Fe/Si multilayer by analysing the hard X-ray Fe $K\beta_{2,5}$ emission band. The characterization of the physical-chemical state of the iron atoms within the Fe/Si multilayer as obtained by XES shows the formation of iron silicide ($FeSi_2$) of 1.4 nm thickness at the interfaces. Until now, X-ray emission has been used to study the multilayer systems in the soft X-ray range and here we presented that the same methodology could be transferred in the hard X-ray range to get information about the multilayer, qualitatively and quantitatively. This methodology could also be applied to study other multilayers provided the emission spectra for the multilayer and the associated references i.e. the possible compounds formed at the interface are of distinct shape. Furthermore, this technique gives better chemically sensitive information of an element, in comparison to other methods such as XRR which is not sensitive enough to identify the small compositional gradients at the interfaces.

More precise information on the buried layers and interfaces of the multilayer stack could be facilitated by using X-ray standing wave technique [8] combined with XES at high spectral resolution. The combination of these techniques will be sensitive to the depth distribution and chemical state of the emitting element thereby providing depth-dependent information of the multilayer in the sub-nanometer resolution.

Chapter 5: Conclusion

The first part of this thesis was dedicated to the interface analysis of Mg/Sc systems with the introduction of ZrC and Cr thin films. The analysis was done by using X-ray reflectivity in both hard and soft X-ray ranges and time of flight – secondary ion mass spectroscopy. X-ray reflectivity helped determine detailed structure of the stack: thickness, roughness and density of different layers and interlayers. ToF-SIMS helped determine a priori information on possible structures, by measuring the distribution of elements as a function of sputter time inside the stacks. Structural investigations using soft X-ray reflectivity around Sc L absorption edge gave information on the variation of dispersion (δ) and absorption (β) coefficients i.e. the real and imaginary part of the complex refractive index; $n = 1 - \delta + i\beta$. Variation of these optical constants of Sc around the absorption edge hinted towards the change in chemical environment of Sc in the Sc/Mg bilayer stack.

The interface analysis of Mg-on-Sc and Sc-on-Mg interfaces in case of Sc/Mg and Mg/Sc bilayers showed an asymmetric behaviour. It was found that an interlayer of MgSc was formed at the two interfaces with thickness 1.54 nm and 0.94 nm respectively. In order to prevent the layers from mixing, a thin film of ZrC was introduced as a barrier layer. The film was also used as the capping layer in order to prevent the stack from oxidation. Hence, the analysis of different sets of quadrilayer systems was made to study different interfaces between ZrC, Sc and Mg layers. The interface between Sc and ZrC layers was found to be rather stable with no intermixing between them. Mg and ZrC layers, however resulted in an interlayer formation.

Cr based Mg/Sc samples were analysed using X-ray reflectivity (XRR) in combination with grazing incidence X-ray fluorescence (GIXRF). While, X-ray reflectivity (XRR) helped determine structural parameters, GIXRF, on the other hand provided depth dependent elemental composition, concentration and thickness of the studied bilayer and trilayer stacks. The measurements were taken at an incident photon energy of 6.25 keV. Top Cr is layer was found to be completely oxidised with the presence of the presence of two types of oxides Cr_2O_3 and

CrO_3. The interfaces Cr-on-Mg and Cr-on-Sc are quite stable and did not undergo intermixing. This could be taken as a point to design a multilayer system of Sc/Cr/Mg trilayer with a good capping layer.

The quality of the multilayer formed depends largely on the deposition technique and careful and precise control of the deposition parameters. The fabrication of a multilayer involves first a test of the deposited thin film of the elements needed in the multilayer. X-ray reflectometry measurements using a table top Cu Kα source of energy 8048 eV are used to test the deposited thin films. Reflectivity provides information about the thickness, density and roughness of the layers and interlayers of thin films and multilayers. Thin film analysis gives an idea on deposited thicknesses which in turn are then taken into account for the calibration of the sputtering systems for further deposition. Calibration thus allows us to set the sputtering rates, power and vacuum conditions, in order to have better precision on the deposition. It is only with repeated tests and calibration; one can achieve a good multilayer with sharp interfaces and with less roughness at the interfaces as well as on the top surface of the multilayer stack. Therefore, with repeated tests and calibration; one can achieve a good multilayer with sharp interfaces and with less roughness at the interfaces as well as on the top surface of the multilayer stack.

The second part of the thesis focuses on the study of interfaces in Fe/Si multilayer with X-ray emission spectroscopy (XES). We characterized and compared the Fe Kβ emission band in $[Fe/Si]_{x40}$ multilayer and that of the Fe and $FeSi_2$ references. The analysis of the physical-chemical state of the iron atoms within the Fe/Si multilayer as obtained by XES shows the formation of iron silicide ($FeSi_2$) of 1.4 nm thickness at the interfaces. Therefore, it can be inferred than XES in the hard X-ray range can provide chemically sensitive information about the multilayer, both qualitatively and quantitatively. This methodology could also be applied to study other multilayers provided the emission spectra for the multilayer and the associated references i.e. the possible compounds formed at the interface are of distinct shape.

References

[1] A.I. Lvovsky, Fresnel Equations, in: Encyclopedia of Optical and Photonic Engineering, Second Edition, 2nd ed., CRC Press, 2015.

[2] A.E. Rosenbluth, P. Lee, Bragg condition in absorbing x-ray multilayers, Appl. Phys. Lett. 40 (1982) 466–468. https://doi.org/10.1063/1.93150.

[3] A.R. Miedema, P.F. de Châtel, F.R. de Boer, Cohesion in alloys — fundamentals of a semi-empirical model, Physica B+C. 100 (1980) 1–28. https://doi.org/10.1016/0378-4363(80)90054-6.

[4] Miedema Calculator: A thermodynamic platform for predicting formation enthalpies of alloys within framework of Miedema’s Theory | Elsevier Enhanced Reader, (n.d.). https://doi.org/10.1016/j.cpc.2016.08.013.

[5] L.G. Parratt, Surface Studies of Solids by Total Reflection of X-Rays, Phys. Rev. 95 (1954) 359–369. https://doi.org/10.1103/PhysRev.95.359.

[6] J.H. Underwood, T.W. Barbee, Layered synthetic microstructures as Bragg diffractors for X rays and extreme ultraviolet: theory and predicted performance, Appl. Opt., AO. 20 (1981) 3027–3034. https://doi.org/10.1364/AO.20.003027.

[7] D.L. Windt, IMD—Software for modeling the optical properties of multilayer films, *Comput. Phys.* 12 (1998) 360. https://doi.org/10.1063/1.168689.

[8] J. Zegenhagen, A. Kazimirov, *The X-ray Standing Wave Technique: Principles and Applications*, World Scientific Publishing Company, Singapore, 2013. https://www.worldscientific.com/doi/epdf/10.1142/6666.

[9] M.-Y. Wu, V. Ilakovac, J.-M. André, K.L. Guen, A. Giglia, J.-P. Rueff, Q.-S. Huang, Z.-S. Wang, P. Jonnard, Study of Pd/Y based multilayers using high energy photoemission spectroscopy combined with x-ray standing waves, in: EUV and X-Ray Optics: Synergy between Laboratory and Space V, SPIE, 2017: pp. 67–73. https://doi.org/10.1117/12.2265630.

[10] K. Holmberg, A. Mathews, Coatings tribology: a concept, critical aspects and future directions, Thin Solid Films. 253 (1994) 173–178. https://doi.org/10.1016/0040-6090(94)90315-8.

[11] A.V. Rane, K. Kanny, V.K. Abitha, S. Thomas, Chapter 5 - Methods for Synthesis of Nanoparticles and Fabrication of Nanocomposites, in: S. Mohan Bhagyaraj, O.S. Oluwafemi, N. Kalarikkal, S. Thomas (Eds.), Synthesis of Inorganic Nanomaterials, Woodhead Publishing, 2018: pp. 121–139. https://doi.org/10.1016/B978-0-08-101975-7.00005-1.

[12] Handbook of Physical Vapor Deposition (PVD) Processing - 2nd Edition, (n.d.). https://www.elsevier.com/books/handbook-of-physical-vapor-deposition-pvd-processing/mattox/978-0-8155-2037-5 (accessed April 5, 2022).

[13] A. Bashir, T.I. Awan, A. Tehseen, M.B. Tahir, M. Ijaz, Chapter 3 - Interfaces and surfaces, in: T.I. Awan, A. Bashir, A. Tehseen (Eds.), Chemistry of Nanomaterials, Elsevier, 2020: pp. 51–87. https://doi.org/10.1016/B978-0-12-818908-5.00003-2.

[14] C. Bundesmann, H. Neumann, Tutorial: The systematics of ion beam sputtering for deposition of thin films with tailored properties, Journal of Applied Physics. 124 (2018) 231102. https://doi.org/10.1063/1.5054046.

[15] C. Patrick, Ion beam sputter deposition allows tailoring of thin film properties, Scilight. 2018 (2018) 510013. https://doi.org/10.1063/1.5086197.

[16] R. Alvarez, J.M. Garcia-Martin, M.C. Lopez-Santos, V. Rico, F.J. Ferrer, J. Cotrino, A.R. Gonzalez-Elipe, A. Palmero, On the Deposition Rates of Magnetron Sputtered Thin Films at Oblique Angles: Deposition Rates at Oblique Angles, Plasma Process. Polym. 11 (2014) 571–576. https://doi.org/10.1002/ppap.201300201.

[17] V. Layes, S. Monje, C. Corbella, J. Trieschmann, T. de los Arcos, A. von Keudell, Species transport on the target during high power impulse magnetron sputtering, Appl. Phys. Lett. 110 (2017) 081603. https://doi.org/10.1063/1.4976999.

[18] M.M. Singh, G. Vijaya, M.S. Krupashankara, B.K. Sridhara, T.N. Shridhara, Studies on Thin Film Multilayer Coatings Deposited using Sputtering Process, Materials Today: Proceedings. 5 (2018) 2994–2999. https://doi.org/10.1016/j.matpr.2018.01.098.

[19] J.W. Cirtain, L. Golub, A.R. Winebarger, B. De Pontieu, K. Kobayashi, R.L. Moore, R.W. Walsh, K.E. Korreck, M. Weber, P. McCauley, A. Title, S. Kuzin, C.E. DeForest, Energy release in the solar corona from spatially resolved magnetic braids, Nature. 493 (2013) 501–503. https://doi.org/10.1038/nature11772.

[20] D. Martínez-Galarce, R. Soufli, D.L. Windt, M. Bruner, E. Gullikson, S. Khatri, E. Spiller, J.C. Robinson, S. Baker, E. Prast, Multisegmented, multilayer-coated mirrors for the Solar Ultraviolet Imager, Opt. Eng. 52 (2013) 095102. https://doi.org/10.1117/1.OE.52.9.095102.

[21] J.L. Culhane, L.K. Harra, A.M. James, K. Al-Janabi, L.J. Bradley, R.A. Chaudry, K. Rees, J.A. Tandy, P. Thomas, M.C.R. Whillock, B. Winter, G.A. Doschek, C.M. Korendyke, C.M. Brown, S. Myers, J. Mariska, J. Seely, J. Lang, B.J. Kent, B.M. Shaughnessy, P.R. Young, G.M. Simnett, C.M. Castelli, S. Mahmoud, H. Mapson-Menard, B.J. Probyn, R.J. Thomas, J. Davila, K. Dere, D. Windt, J. Shea, R. Hagood, R. Moye, H. Hara, T. Watanabe, K. Matsuzaki, T. Kosugi, V. Hansteen, Ø. Wikstol, The EUV Imaging Spectrometer for Hinode, Sol Phys. 243 (2007) 19–61. https://doi.org/10.1007/s01007-007-0293-1.

[22] F. Delmotte, E. Meltchakov, S. de Rossi, F. Bridou, A. Jérome, F. Varnière, R. Mercier, F. Auchère, X. Zhang, B. Borgo, C. Dumesnil, S. François, M. Roulliay, U. Strauch, Development of multilayer coatings for solar orbiter EUV imaging telescopes, in: Solar Physics and Space Weather Instrumentation V, SPIE, 2013: pp. 64–73. https://doi.org/10.1117/12.2036050.

[23] M.-F. Ravet, F. Bridou, X. Zhang-Song, A. Jerome, F. Delmotte, R. Mercier, M. Bougnet, P. Bouyries, J.-P. Delaboudiniere, Ion-beam-deposited Mo/Si multilayers for EUV imaging applications in astrophysics, in: Advances in Optical Thin Films, SPIE, 2004: pp. 99–108. https://doi.org/10.1117/12.514597.

[24] R.A. Stern, B.M. Haisch, E.G. Joki, R.C. Catura, Normal incidence multilayer mirrors for extreme ultraviolet astronomy., 445 (1984) 347–357. https://doi.org/10.1117/12.966166.

[25] C. Montcalm, E.A. Spiller, M. Wedowski, E.M. Gullikson, J.A. Folta, Multilayer coating of 10X projection optics for extreme ultraviolet lithography, in: Emerging Lithographic Technologies III, SPIE, 1999: pp. 710–716. https://doi.org/10.1117/12.351157.

[26] A. Sorrentino, J. Nicolás, R. Valcárcel, F.J. Chichón, M. Rosanes, J. Avila, A. Tkachuk, J. Irwin, S. Ferrer, E. Pereiro, MISTRAL: a transmission soft X-ray microscopy beamline for cryo nano-tomography of biological samples and magnetic domains imaging, J Synchrotron Rad. 22 (2015) 1112–1117. https://doi.org/10.1107/S1600577515008632.

[27] H. Legall, H. Stiel, G. Blobel, C. Seim, J. Baumann, S. Yulin, D. Esser, M. Hoefer, U. Wiesemann, M. Wirtz, G. Schneider, S. Rehbein, H.M. Hertz, A compact Laboratory Transmission X-ray Microscope for the water window, J. Phys.: Conf. Ser. 463 (2013) 012013. https://doi.org/10.1088/1742-6596/463/1/012013.

[28] M. Rose, P. Skopintsev, D. Dzhigaev, O. Gorobtsov, T. Senkbeil, A. von Gundlach, T. Gorniak, A. Shabalin, J. Viefhaus, A. Rosenhahn, I. Vartanyants, Water window ptychographic imaging with characterized coherent X-rays, J Synchrotron Rad. 22 (2015) 819–827. https://doi.org/10.1107/S1600577515005524.

[29] C. Burcklen, S. de Rossi, E. Meltchakov, D. Dennetière, B. Capitanio, F. Polack, F. Delmotte, High-reflectance magnetron-sputtered scandium-based x-ray multilayer mirrors for the water window, Optics Letters. 42 (2017) 1927. https://doi.org/10.1364/OL.42.001927.

[30] K. Le Guen, H. Maury, J.-M. André, P. Jonnard, A. Hardouin, F. Delmotte, M.-F. Ravet-Krill, X-ray spectroscopic application of Cr⁄Sc periodic multilayers, Appl. Phys. Lett. 91 (2007) 234104. https://doi.org/10.1063/1.2821379.

[31] Q. Huang, Q. Yi, Z. Cao, R. Qi, R.A. Loch, P. Jonnard, M. Wu, A. Giglia, W. Li, E. Louis, F. Bijkerk, Z. Zhang, Z. Wang, High Reflectance Nanoscale V/Sc Multilayer for Soft X-ray Water Window Region, Sci Rep. 7 (2017) 12929. https://doi.org/10.1038/s41598-017-13222-5.

[32] V. Polkonikov, N. Chkhalo, R. Pleshkov, A. Giglia, N. Rividi, E. Brackx, K. Le Guen, I. Ismail, P. Jonnard, Periodic Multilayer for X-ray Spectroscopy in the Li K Range, Applied Sciences. 11 (2021) 6385. https://doi.org/10.3390/app11146385.

[33] C. Hombourger, P. Jonnard, J.-M. André, J.-P. Chauvineau, Use of layered synthetic microstructures for the quantitative x-ray analysis of light elements, X-Ray Spectrometry. 28 (1999) 163–167. https://doi.org/10.1002/(SICI)1097-4539(199905/06)28:3<163::AID-XRS331>3.0.CO;2-Z.

[34] J.B. MacNaughton, E.Z. Kurmaev, L.D. Finkelstein, J.S. Lee, S.D. Wettig, A. Moewes, Electronic structure and charge carriers in metallic DNA investigated by soft x-ray spectroscopy, Phys. Rev. B. 73 (2006) 205114. https://doi.org/10.1103/PhysRevB.73.205114.

[35] Structural and Band Gap Investigation of GaN:ZnO Heterojunction Solid Solution Photocatalyst Probed by Soft X-ray Spectroscopy - Google Search, (n.d.). https://www.google.com/search?q=Structural+and+Band+Gap+Investigation+of+GaN%3AZnO+Heterojunction+Solid+Solution+Photocatalyst+Probed+by+Soft+X-ray+Spectroscopy&rlz=1C1CHBF_enFR880FR880&oq=Structural+and+Band+Gap+Investigation+of+GaN%3AZnO+Heterojunction+Solid+Solution+Photocatalyst+Probed+by+Soft+X-ray+Spectroscopy&aqs=chrome..69i57j69i61l3.750j0j7&sourceid=chrome&ie=UTF-8 (accessed July 11, 2022).

[36] V.N. Strocov, P.O. Nilsson, T. Schmitt, R. Claessen, A.Y. Egorov, V.M. Ustinov, Zh.I. Alferov, LOCAL ELECTRONIC STRUCTURE OF N ATOMS IN Ga(In)AsN BY SOFT-X-RAY ABSORPTION AND EMISSION: OPTICAL EFFICIENCY, Int. J. Nanosci. 03 (2004) 95–103. https://doi.org/10.1142/S0219581X04001869.

[37] P. Jonnard, M. Wu, K. Le Guen, A. Giglia, K. Koshmak, Q. Huang, Z. Zhang, Z. Wang, I. Esteve, N. Menguy, B. Doisneau, Characterization of Sc/Mg multilayers with and without Co barriers layers for x-ray spectroscopy in the water window range, J. Appl. Phys. 126 (2019).

[38] Willmott, Philip. An introduction to synchrotron radiation: techniques and applications., John Wiley & Sons, 2019.

[39] M.H. Modi, R.K. Gupta, S.R. Kane, V. Prasad, C.K. Garg, P. Yadav, V.K. Raghuvanshi, A. Singh, M. Sinha, A soft x-ray reflectivity beamline for 100-1500 eV energy range at Indus-2 synchrotron radiation source, AIP Conference Proceedings. 2054 (2019) 060022. https://doi.org/10.1063/1.5084653.

[40] G. Lodha, M. Modi, V.K. Raghuvanshi, K.J.S. Sawhney, V. Nandedkar, Soft x-ray reflectometer on Indus-1, Synchrotron Radiat. News. 17 (2004) 33–35. https://doi.org/10.1080/08940880408603084.

[41] M. Nayak, G.S. Lodha, A.K. Sinha, R.V. Nandedkar, S.A. Shivashankar, Determination of interlayer composition at buried interfaces using soft x-ray resonant reflectivity, Appl. Phys. Lett. 89 (2006) 181920. https://doi.org/10.1063/1.2374865.

[42] P.N. Rao, U.K. Goutam, P. Kumar, M. Gupta, T. Ganguli, S.K. Rai, Depth-resolved compositional analysis of W/B4C multilayers using resonant soft X-ray reflectivity, Journal of Synchrotron Radiation. 26 (2019) 793–800. https://doi.org/10.1107/S1600577519002339.

[43] M. Nayak, G.S. Lodha, Optical Response Near the Soft X-Ray Absorption Edges and Structural Studies of Low Optical Contrast System Using Soft X-Ray Resonant

Reflectivity, Journal of Atomic, Molecular, and Optical Physics. 2011 (2011) e649153. https://doi.org/10.1155/2011/649153.

[44] U. Bergmann, P. Glatzel, X-ray emission spectroscopy, Photosynth Res. 102 (2009) 255. https://doi.org/10.1007/s11120-009-9483-6.

[45] J.-P. Rueff, J.M. Ablett, D. Céolin, D. Prieur, T. Moreno, V. Balédent, B. Lassalle, J.E. Rault, M. Simon, A. Shukla, The Galaxies Beamline at SOLEIL Synchrotron: Inelastic X-ray Scattering and Photoelectron Spectroscopy in the Hard X-ray Range, J Synchrotron Rad. 22 (2015) 175–179. https://doi.org/10.1107/S160057751402102X.

[46] J.M. Ablett, D. Prieur, D. Céolin, B. Lassalle-Kaiser, B. Lebert, M. Sauvage, Th. Moreno, S. Bac, V. Balédent, A. Ovono, M. Morand, F. Gélebart, A. Shukla, J.-P. Rueff, The GALAXIES inelastic hard X-ray scattering end-station at Synchrotron SOLEIL, *J. Synchrotron Radiat.* 26 (2019) 263–271. https://doi.org/10.1107/S160057751801559X.

[47] M. Schmeling, Total reflection X-ray fluorescence, Physical Sciences Reviews. 4 (2019). https://doi.org/10.1515/psr-2017-0161.

[48] D.K.G. de Boer, Glancing-incidence x-ray fluorescence of layered materials, Phys. Rev. B. 44 (1991) 498–511. https://doi.org/10.1103/PhysRevB.44.498.

[49] Y. Ménesguen, B. Boyer, H. Rotella, J. Lubeck, J. Weser, B. Beckhoff, D. Grötzsch, B. Kanngießer, A. Novikova, E. Nolot, M.-C. Lépy, CASTOR, a new instrument for combined XRR-GIXRF analysis at SOLEIL, X-Ray Spectrometry. 46 (2017) 303–308. https://doi.org/10.1002/xrs.2742.

[50] Y. Ménesguen, M.-C. Lépy, Metrology of thin layer deposition with combined XRR-GIXRF analysis at SOLEIL synchotron, in: Metrology, Inspection, and Process Control for Semiconductor Manufacturing XXXV, SPIE, 2021: pp. 54–62. https://doi.org/10.1117/12.2583702.

[51] S. Kodigala, The Role of Characterization Techniques in the Thin Film Analysis, in: 2014: pp. 67–140. https://doi.org/10.1016/B978-0-12-394429-0.00004-4.

[52] Secondary Ion Mass Spectrometry - an overview | ScienceDirect Topics, (n.d.). https://www.sciencedirect.com/topics/physics-and-astronomy/secondary-ion-mass-spectrometry (accessed May 22, 2022).

[53] A. Dębski, R. Dębski, W. Gasior, New features of Entall database: Comparison of experimental and model formation enthalpies, Archives of Metallurgy and Materials. 59 (2015) 1337–1343. https://doi.org/10.2478/amm-2014-0228.

[54] O. Thomas, C.S. Petersson, F.M. d'Heurle, The reaction of scandium thin films with silicon: diffusion, nucleation, resistivities, Applied Surface Science. 53 (1991) 138–146. https://doi.org/10.1016/0169-4332(91)90254-H.

[55] Y.A. Uspenskii, V.E. Levashov, A.V. Vinogradov, A.I. Fedorenko, V.V. Kondratenko, Y.P. Pershin, E.N. Zubarev, V.Y. Fedotov, High-reflectivity multilayer mirrors for a

vacuum-ultraviolet interval of 35–50??nm, Opt. Lett., OL. 23 (1998) 771–773. https://doi.org/10.1364/OL.23.000771.

[56] S.P. Singh, M.H. Modi, P. Srivastava, Growth kinetics and compositional analysis of silicon rich a-SiNx:H film: A soft x-ray reflectivity study, Appl. Phys. Lett. 97 (2010) 151906. https://doi.org/10.1063/1.3497284.

[57] A. Majhi, M. Nayak, P.C. Pradhan, E.O. Filatova, A. Sokolov, F. Schäfers, Soft X-ray Reflection Spectroscopy for Nano-Scaled Layered Structure Materials, Sci Rep. 8 (2018) 15724. https://doi.org/10.1038/s41598-018-34076-5.

[58] M.H. Modi, M. Sinha, A. Bose, A. Singh, P. Jonnard, Depth analysis of Al/ZrC interfaces using SIMS and x-ray reflectivity, Surf Interface Anal. 50 (2018) 1239–1242. https://doi.org/10.1002/sia.6443.

[59] M. Fernández-Perea, J.I. Larruquert, J.A. Aznárez, J.A. Méndez, L. Poletto, A.M. Malvezzi, A. Giglia, S. Nannarone, Determination of optical constants of scandium films in the 20-1000 eV range, J. Opt. Soc. Am. A, JOSAA. 23 (2006) 2880–2887. https://doi.org/10.1364/JOSAA.23.002880.

[60] Y.A. Uspenskii, J.F. Seely, N.L. Popov, A.V. Vinogradov, Y.P. Pershin, V.V. Kondratenko, Efficient method for the determination of extreme-ultraviolet optical constants in reactive materials: application to scandium and titanium, J. Opt. Soc. Am. A, JOSAA. 21 (2004) 298–305. https://doi.org/10.1364/JOSAA.21.000298.

[61] CXRO X-Ray Interactions With Matter, (n.d.). https://henke.lbl.gov/optical_constants/ (accessed April 13, 2022).

[62] E.A. Juarez-Arellano, B. Winkler, S.C. Vogel, A. Senyshyn, D.R. Kammler, M. Avalos-Borja, In situ observation of the reaction of scandium and carbon by neutron diffraction, Journal of Alloys and Compounds. 509 (2011) 1–5. https://doi.org/10.1016/j.jallcom.2010.08.081.

[63] K.A. Gschneidner, F.W. Calderwood, The C−Sc (Carbon-Scandium) system, Bulletin of Alloy Phase Diagrams. 7 (1986) 559–560. https://doi.org/10.1007/BF02869868.

[64] H.-L. Chen, R. Schmid-Fetzer, The Mg–C phase equilibria and their thermodynamic basis, International Journal of Materials Research. 103 (2012) 1294–1301. https://doi.org/10.3139/146.110787.

[65] H. Li, J. Zhu, Z. Wang, Z. Song, H. Chen, Asymmetrical diffusion at interfaces of Mg/SiC multilayers, Optical Materials Express. 3 (2013). https://doi.org/10.1364/OME.3.000546.

[66] Y. Ménesguen, M.-C. Lépy, COLEGRAM, a flexible user-friendly software for processing of ionizing radiation spectra, Nuclear Instruments and Methods in Physics Research Section A: Accelerators, Spectrometers, Detectors and Associated Equipment. 1003 (2021) 165341. https://doi.org/10.1016/j.nima.2021.165341.

[67] M. Gasgnier, L. Névot, Analysis and crystallographic structures of chromium thin films, Physica Status Solidi (a). 66 (1981) 525–540. https://doi.org/10.1002/pssa.2210660215.

[68] R. Matyi, M. Hatzistergos, E. Lifshin, X-ray reflectometry analyses of chromium thin films, Thin Solid Films. 515 (2006) 1286–1293. https://doi.org/10.1016/j.tsf.2006.03.016.

[69] A. Lippitz, Th. Hübert, XPS investigations of chromium nitride thin films, Surface and Coatings Technology. 200 (2005) 250–253. https://doi.org/10.1016/j.surfcoat.2005.02.091.

[70] K. Petkov, V. Krastev, Ts. Marinova, XPS analysis of thin chromium films, Surface and Interface Analysis. 18 (1992) 487–490. https://doi.org/10.1002/sia.740180705.

[71] N. Miyata, S. Ishikawa, M. Yanagihara, M. Watanabe, Buried Interfaces in Mo/Si Multilayers Studied by Soft-X-Ray Emission Spectroscopy, *Jpn. J. Appl. Phys*. 38 (1999) 6476. https://doi.org/10.1143/JJAP.38.6476.

[72] I. Jarrige, P. Jonnard, N. Frantz-Rodriguez, K. Danaie, A. Bosseboeuf, Study of the NiTi/SiO2 interface: analysis of the electronic distributions, *Surf. Interface Anal*. 34 (2002) 694–697. https://doi.org/10.1002/sia.1390.

[73] P. Jonnard, K. Guen, R. Gauvin, J.-F. Berre, Characterization of Al and Mg Alloys from Their X-Ray Emission Bands, *Microscopy & Microanalysis* 15 (2009) 36–45. https://doi.org/10.1017/S1431927609090060.

[74] M. Salou, S. Rioual, J.B. Youssef, D.T. Dekadjevi, S.P. Pogossian, P. Jonnard, K.L. Guen, G. Gamblin, B. Rouvellou, Inter-diffusion effects in as-deposited Al/Ni polycrystalline multi-layers, *Surf. Interface Anal.* 40 (2008) 1318–1321. https://doi.org/10.1002/sia.2896.

[75] T. Nyberg, P. Skytt, B. Gålnander, C. Nender, J. Nordgren, S. Berg, Studies of reactive sputtering of multi-phase chromium nitride, *J. Vac. Sci. Technol.* A. 15 (1997) 248–252. https://doi.org/10.1116/1.580520.

[76] P. Jonnard, H. Maury, J.-M. André, Wavelength despersive spectroscopy analysis at high spectral resolution: application to the study of Mo/Si multilayers, *X-Ray Spectrom.* 36 (2007) 72–75. https://doi.org/10.1002/xrs.940.

[77] T. Lucinski, P. Chomiuk, Magnetic and electric properties of (Fe, Co)/(Si, Ge) multilayers, *Open Phys.* 9 (2011) 276–286. https://doi.org/10.2478/s11534-010-0145-2.

[78] T. Imazono, Y. Hirayama, S. Ichikura, O. Kitakami, M. Yanagihara, M. Watanabe, Interdiffused Layers in Antiferromagnetically Coupled Fe/Si Multilayers Studied by Soft-X-Ray Fluorescence Spectroscopy, *Jpn. J. Appl. Phys.* 43 (2004) 4327. https://doi.org/10.1143/JJAP.43.4327.

[79] null Chaiken, null Michel, null Wall, Structure and magnetism of Fe/Si multilayers grown by ion-beam sputtering, Phys Rev B Condens Matter. 53 (1996) 5518–5529. https://doi.org/10.1103/physrevb.53.5518.

[80] G. Crecelius, Reaction of iron on silicon, *Appl. Surf. Sci.* 65–66 (1993) 683–689. https://doi.org/10.1016/0169-4332(93)90739-X.

[81] M. WATANABE, T. Ejima, N. MIYATA, T. IMAZONO, M. YANAGIHARA, Studies of multilayer structure in depth direction by soft X-ray spectroscopy, Nuclear Science and Techniques. 17 (2006) 257–267. https://doi.org/10.1016/S1001-8042(06)60048-1.

[82] H. Maury, J.-M. André, K. Le Guen, N. Mahne, A. Giglia, S. Nannarone, F. Bridou, F. Delmotte, P. Jonnard, Analysis of periodic Mo/Si multilayers: Influence of the Mo thickness, Surface Science. 603 (2009) 407–411. https://doi.org/10.1016/j.susc.2008.12.002.

[83] L. Badía-Romano, J. Rubín, C. Magén, D.E. Bürgler, J. Bartolomé, Iron silicide formation at different layers of (Fe/Si)3 multilayered structures determined by conversion electron Mössbauer spectroscopy, *J. Appl. Phys.* 116 (2014) 023907. https://doi.org/10.1063/1.4887522.

[84] N.R. Baldwin, D.G. Ivey, Low temperature iron thin film-silicon reactions, JOURNAL OF MATERIALS SCIENCE. 31 (1996) 31–37. https://doi.org/10.1007/BF00355122.

[85] M. Walterfang, W. Keune, K. Trounov, R. Peters, U. Rücker, K. Westerholt, Magnetic and structural properties of epitaxial c-FeSi films grown on MgO(100), *Phys. Rev. B.* 73 (2006) 214423. https://doi.org/10.1103/PhysRevB.73.214423.

[86] J.M. Gallego, J.M. García, J. Alvarez, R. Miranda, Metallization-induced spontaneous silicide formation at room temperature: The Fe/Si case, Phys. Rev. B. 46 (1992) 13339–13344. https://doi.org/10.1103/PhysRevB.46.13339.

[87] K. Radermacher, S. Mantl, Ch. Dieker, H. Lüth, C. Freiburg, Growth kinetics of iron silicides fabricated by solid phase epitaxy or ion beam synthesis, Thin Solid Films. 215 (1992) 76–83. https://doi.org/10.1016/0040-6090(92)90704-F.

[88] S. Luby, G. Leggieri, A. Luches, M. Jergel, G. Majni, E. Majkova, M. Ožvold, Interfacial reactions of thin iron films on silicon under amorphous silicon and SiOx capping, Thin Solid Films. 245 (1994) 55–59. https://doi.org/10.1016/0040-6090(94)90877-X.

[89] I.A. Tarasov, M.A. Visotin, A.S. Aleksandrovsky, N.N. Kosyrev, I.A. Yakovlev, M.S. Molokeev, A.V. Lukyanenko, A.S. Krylov, A.S. Fedorov, S.N. Varnakov, S.G. Ovchinnikov, Si/Fe flux ratio influence on growth and physical properties of polycrystalline β-FeSi2 thin films on Si(100) surface, *J. Magn. Magn. Mater.* 440 (2017) 144–152. https://doi.org/10.1016/j.jmmm.2016.12.084.

[90] P. Zaumseil, High-resolution characterization of the forbidden Si 200 and Si 222 reflections, J Appl Crystallogr. 48 (2015) 528–532. https://doi.org/10.1107/S1600576715004732.

[91] S.R. Naik, S. Rai, M.K. Tiwari, G.S. Lodha, Structural asymmetry of Si/Fe and Fe/Si interface in Fe/Si multilayers, *J. Phys. Appl. Phys.* 41 (2008) 115307. https://doi.org/10.1088/0022-3727/41/11/115307.

[92] A. Gupta, D. Kumar, V. Phatak, Asymmetric diffusion at the interfaces in Fe/Si multilayers, *Phys. Rev. B.* 81 (2010) 155402. https://doi.org/10.1103/PhysRevB.81.155402.